



Max-Planck-Institut für Metallforschung
Stuttgart

**Microstructure and Chemistry of Grain-
Boundary Films and Triple-Junction Phases in
Liquid-Phase Sintered SiC Ceramics**

Haihui Ye

Dissertation
an der
Universität Stuttgart

Bericht Nr. 114
Januar 2002

Microstructure and Chemistry of Grain-Boundary Films and Triple-Junction Phases in Liquid-Phase Sintered SiC Ceramics

Von der Fakultät Chemie der Universität Stuttgart
zur Erlangung der Würde eines Doktors der
Naturwissenschaften (Dr.rer.nat.) genehmigte Abhandlung

Vorgelegt von

Haihui Ye

aus Shanghai, China

Hauptberichter:	Prof. Dr. F. Aldinger
Mitberichter:	Prof. Dr. G. Petzow
Tag der mündlichen Prüfung:	18.01.2002

Institut für Nichtmetallische Anorganische Materialien der Universität Stuttgart
Max-Planck-Institut für Metallforschung, Stuttgart
Pulvermetallurgisches Laboratorium

2002

献给亲爱的父母和妻子

in Liebe für meine Eltern und Yan

Dedicated to my parents and Yan with love

Microstructure and Chemistry of Grain-Boundary Films and Triple-Junction Phases in Liquid-Phase Sintered SiC Ceramics

(Ph.D. Thesis)

by

Haihui Ye

ABSTRACT

Thorough investigation of the microstructure and chemistry of the intergranular phases including grain-boundary films and triple-junction phases is essential in order to understand the sintering behavior of the materials and therefore helpful to improve the mechanical properties. For this object three SiC-based materials are prepared and studied, including two model systems and one technically relevant system. The first model system consist of SiC-SiO₂. Silica was used as the only sintering additive in order to obtain intergranular phases without any extra element and simplify the analyses and model calculations. The second model system is based on coarse SiC powder (32-160 μm) which was liquid-phase sintered using Y₂O₃ and AlN as additives. Large particles were used in order to create large intergranular spaces at triple junctions, enabling there precise compositional analyses by wavelength-dispersive X-ray spectrometry (WDS, with a spatial resolution of 1 μm). For the third material also Y₂O₃ and AlN were used as sintering additives, however, in combination with SiC powder with a ‘normal’ (sub-μm) mean particle size. SEM, TEM, and HRTEM were performed to observe the microstructure of the materials, while XRD, EDS, WDS, and EELS were performed to quantify chemical compositions.

The main emphasis of the experimental studies and discussions on the SiC-SiO₂ model system is on the grain-boundary films. Stable amorphous films with a mean width of 1.5 nm were found at grain boundaries by HRTEM. This result disagrees with the well-known model originally proposed by Clarke [CLA87] which predicts ‘clean’ grain boundaries for SiC-SiO₂ system. EELS spectra show that the grain-boundary films contain not only silica but also C and N. C originates from the SiC grains, and N from the sintering atmosphere. Thermodynamic calculations within the framework of Clarke’s model were conducted by considering the force balance between attractive Van der Waals forces in adjacent grains and the repulsive ‘steric force’ originating from the rearrangement of structural units, for example,

oxygen-coordinated silicon tetrahedra in the films. Calculations show that C and N modify the structural units in the intergranular phases, increase the repulsive ‘steric force’ counterbalancing the attractive Van der Waals force between SiC grains, and stabilize the grain-boundary films. The effects of sintering atmosphere on the triple-junction phases were also studied. Nanometer-sized $\text{Si}_2\text{N}_2\text{O}$ crystals were found to grow in triple junctions because of the incorporation of N from the sintering atmosphere.

In the liquid-phase sintered coarse SiC, a N-rich amorphous phase (about 44 at% N) was identified by WDS to be the main triple-junction phase, while three further secondary intergranular phases were AlN, $\text{Y}_2\text{SiN}_4\text{O}_3$ and an O-rich phase ($\text{Y}_{10}\text{Al}_2\text{Si}_3\text{O}_{18}\text{N}_4$). The overall O content was found to be reduced in comparison to the initial powder composition. The incorporation of N from the sintering atmosphere into the intergranular phase and a subsequent carbothermal reduction are believed to be responsible for the removal of O and the formation of the N-rich amorphous phase. The improved sintering behavior of SiC-AlN- Y_2O_3 in N_2 atmosphere compared with that in argon and a characteristic strengthening effect at high temperature can be explained by taking this newly discovered N-rich amorphous phase into account.

The fine-grained α -SiC was sintered with AlN and Y_2O_3 in Ar or N_2 atmosphere to high density. The existence of stable grain-boundary films is consistent with the observation in the SiC-SiO₂ model system. EELS analyses show that the different sintering atmospheres lead to the different compositions of the triple-junction phases which are $\text{Y}_{10}\text{Al}_2\text{Si}_3\text{O}_{18}\text{N}_4$ in case of Ar atmosphere, $\text{Y}_2\text{SiN}_4\text{O}_3$ and $\text{Y}_{10}\text{Al}_2\text{Si}_3\text{O}_{18}\text{N}_4$ in case of N_2 atmosphere, respectively. The formation and distribution of these crystalline phases at triple junctions can be understood by considering the different viscosity of O-rich liquid and N-rich liquid at elevated temperature. The distributions of N, O, C, Si across the triple junctions were analyzed by performing line-scanning EELS analyses. The microanalysis results reveal the composition of the amorphous interfaces which were observed by HRTEM to be present between triple-junction phases and SiC grains. The amorphous interface is rich of N in case of Ar sintering atmosphere, while it consists of two layers in case of N_2 sintering atmosphere: N-rich layer adjacent to the SiC grain and O-rich layer facing the triple junction.

ACKNOWLEDGEMENTS

This Ph.D. work was done from September 1998 to August 2001 in Max-Planck-Institute for Metal Research, Stuttgart, supported by Max-Planck-Society Scholarship.

I would like to thank my advisor Prof. Dr. F. Aldinger for encouraging me to investigate the topic of this work which I found very interesting. During the three years in MPI I not only learned the methods for scientific research, but also was trained to become an independent scientist, which may be of more value. Without the encouragement and continual support from Prof. Dr. F. Aldinger, my achievement would not be possible.

My special thank is given to Dr. G. Rixecker. He is so nice a group leader that working with him is a happy experience. Most importantly, I learned much from his serious attitude toward scientific work and writing of scientific articles.

I want to thank Prof. Dr. E. J. Mittemeijer who, together with my advisor, gave me an examination at the beginning of my Ph.D. work and kindly encouraged me to do well in the future. I want also to thank Prof. Dr. G. Petzow who friendly helped me and accepted to become the 'Mitberichter' for my final examination.

There were many people in MPI who trained me and helped me. Dr. F. Phillipp, Ms. M. Kelsch, Mr. P. Kopold and Dr. C. Scheu trained me to operate TEM observations and EELS analyses. Mr. M. Schweizer showed me the whole procedure to prepare ceramic samples. Mr. H. Labitzke helped me to do SEM observations. Ms. S. Haug helped to do WDS analyses. Ms. M. Thomas helped to do XRD analyses. The very important computer services are provided by Mr. E. Bruckner. Therefore I would like to take this opportunity to express my sincere thanks to them.

There were many other people who made my working and living easier and full of fun. For example, Ms A. Rohrbach helped me settle down with no problem when I just arrived at Stuttgart; Ms S. Paulsen always helped me with a nice smile; my roommate Dr. R. Hoffmann and K. Biswas are nice people and often discussed with me about my speciality: Chinese words; my colleagues Dr. L. Wang and J. Peng invited me to have dinner with them; ..., and so on. There were many many same kinds of things which I can not list all but in deed make me feel very happy and very lucky to work in such a group. Here I would like to thank all of my colleagues who have ever helped me.

My family is a source of support in many forms. My parents always sent E-mails to me with motherly care. My brother always took his responsibility to repair my parents' computer and E-mail system to enable them work well. My daughter, several months old, slept so quietly at night and caused absolutely no trouble to my working. Without a doubt, the biggest support was from my lovely wife: Yan. I thank you so much.

TABLE OF CONTENTS

ABSTRACT.....	2
ACKNOWLEDGEMENTS.....	4
TABLE OF CONTENTS.....	5
LIST OF SYMBOLS AND ABBREVIATIONS.....	7
1 INTRODUCTION	9
2 REVIEW OF SINTERING AND MICROSTRUCTURES OF SiC-BASED CERAMICS	11
2.1 Structural properties of SiC	11
2.2 Sintering of SiC.....	12
2.2.1 Difficulties in sintering	12
2.2.2 Solid-state sintering	13
2.2.3 Liquid-phase sintering	13
2.3 Microstructure features of liquid-phase sintered SiC	16
2.3.1 Phase transformation.....	16
2.3.2 Coarsening and solution-precipitation process	17
2.3.3 Effect of sintering atmosphere on microstructures	17
2.4 Grain-boundary films and triple-junction phases of SiC ceramics	18
2.4.1 Stability of grain-boundary films in ceramic materials	18
2.4.2 Grain-boundary films in liquid-phase sintered SiC	19
2.4.3 Triple-junction phases and their crystallization	21
3 CHARACTERIZATION METHOD – ELECTRON MICROSCOPY	27
3.1 Interactions between electrons and matter	27
3.2 Scanning electron microscopy and X-ray microanalysis	28
3.3 Transmission electron microscopy	29
3.4 High resolution transmission electron microscopy	30
3.5 Electron energy-loss spectrometry.....	32
3.6 Specimen preparation for TEM	34
4 THE MODEL SYSTEM SiC-SiO ₂	41
4.1 Introduction.....	41
4.2 Experimental procedure	41
4.3 Densification	42
4.3.1 Effect of sintering temperature	42

4.3.2	Effect of the SiO ₂ content	43
4.4	Grain-boundary films.....	44
4.4.1	HRTEM observations and EELS compositional analyses.....	44
4.4.2	Calculations based on Clarke's model.....	44
4.5	Si ₂ N ₂ O crystallization in triple junctions.....	46
4.6	Crack deflection.....	47
5	THE "COARSE SiC" MODEL SYSTEM	62
5.1	Introduction.....	62
5.2	Experimental procedure.....	62
5.3	Overall microstructure and composition.....	63
5.4	Chemical composition of intergranular phases.....	65
5.5	Crystalline intergranular phases.....	66
5.6	Effect of nitrogen incorporation.....	67
6	LPS-SiC WITH Y ₂ O ₃ -AlN ADDITIVES	77
6.1	Introduction.....	77
6.2	Experimental procedure.....	77
6.3	Densification.....	78
6.4	Effect of sintering atmosphere on grain growth and densification.....	79
6.5	SiC grain morphology and phase transformation.....	80
6.6	Grain-boundary films.....	81
6.6.1	HRTEM observation.....	81
6.6.2	EELS analyses and element excess.....	82
6.6.3	ELNES analyses and bonding information.....	83
6.7	Triple-junction phases.....	83
6.7.1	Triple junctions and large pockets.....	83
6.7.2	Crystallization of phases at triple junctions and large pockets.....	84
6.7.3	Identification of the secondary crystalline phases.....	84
6.7.4	EELS analyses and confirmation of N-rich triple-junction phases.....	85
6.7.5	Distribution of elements across triple-junction phases.....	86
7	SUMMARY AND CONCLUSIONS	109
	ZUSAMMENFASSUNG.....	111
	REFERENCES	121
	CURRICULUM VITAE (LEBENS LAUF).....	128

LIST OF SYMBOLS AND ABBREVIATIONS

ϕ	dihedral angle
σ	scattering cross section
σ_i	scattering cross section of a segregated element
σ_r	scattering cross section of reference element
$\sigma(\beta\Delta)$	partial ionization cross section
$\alpha\eta_o^2$	'ordering force' constant in Eq. 4.2
β	collection semiangle
Δ	energy window
ΔG	free-energy change
ξ	structural correlation length
γ_{gb}	grain boundary energy
γ_{sv}	solid/vapor surface energy
Γ_i	excess of a segregated element at a grain boundary
A	fitting parameter in Eq. 3.1
d	particle size distribution
E	energy loss
H	Hamaker constant
h	film thickness
I	intensity in the channel of energy loss E
I	EELS edge intensity
I_k	K shell intensity
I_l	intensity of the zero-loss and low-loss electrons
N_k	number density of atoms belonging to a K shell edge
N_r	site density of the reference element in bulk grains
P	pressure
r	fitting parameter in Eq. 3.1
T	temperature
T_m	melting temperature
w	width of the analysis region across the grain boundary
Z	atomic number

AEM	analytical electron microscope
BF	bright-field TEM image
BSE	backscattered electron microscopy
CBED	convergent-beam electron diffraction
DF	dark-field TEM image
DSTEM	dedicated scanning transmission electron microscope
EDS	energy-dispersive X-ray spectrometry
EELS	electron energy-loss spectrometry
ELNES	energy-loss near-edge structure
FEG	field-emission gun
GB	grain boundary
GPS	gas-pressure sintering
HIP	hot-isostatic pressing
HRTEM	high resolution transmission electron microscopy / microscope
HVEM	high-voltage electron microscope
IVEM	intermediate voltage electron microscope
LPS	liquid-phase sintering
PEELS	parallel-acquisition electron energy-loss spectrometry
SAD	selected-area diffraction
SEELS	serial-acquisition electron energy-loss spectrometry
SEM	scanning electron microscopy / microscope
STEM	scanning transmission electron microscopy / microscope
TEM	transmission electron microscopy / microscope
WDS	wavelength-dispersive X-ray spectrometry
XRD	X-ray diffraction

1 INTRODUCTION

Silicon carbide (SiC) possesses a combination of advanced properties, such as strength retention to high temperatures, high chemical stability, high wear resistance, high thermal conductivity, good thermal-shock resistance, and excellent oxidation resistance, which make it a superb material for high-temperature application. However, it is difficult to obtain dense sintered compacts due to the highly covalent bonding character of SiC. Although development of the Acheson process in 1892 [ACH92] brought SiC production to a commercial scale, the widespread application of SiC as a structural material became possible only after Prochazka [PRO75] developed a technique in 1975 using additives for pressureless solid state sintering.

Liquid-phase sintering of SiC-based ceramics has received great attention since the 1980s [OMO82] because sintering temperatures for full densification can be reduced dramatically. A variety of additive systems including oxides, nitrides, carbides, and metals has been adopted. All of them introduce during sintering intergranular phases at grain boundaries and triple junctions which have a pronounced influence upon the final properties. For example, strong intergranular bonding is required for creep resistance and high strength at elevated temperatures, while activation of toughening mechanisms such as crack deflection, crack bridging and micro-cracking relies on 'sufficiently weak' interfaces. Control of the microstructure and chemistry of intergranular phases is therefore particularly important.

Since the presence of thin amorphous films along grain boundaries was first observed in Si₃N₄ densified with a MgO additive by high resolution transmission electron microscopy in 1977 [CLA77], numerous investigations including microscopic observation, compositional identification and model calculations by using TEM and related microanalysis have been conducted on the intergranular phases of ceramic materials. However, compared with Si₃N₄-based material which is also fabricated by liquid-phase sintering, much less research on the grain-boundary films and triple-junction phases has been performed for SiC-based materials. For example, it is already a well-established concept that amorphous grain-boundary films with about 1 nm thickness are always present in liquid-phase sintered Si₃N₄-based material. The amorphous grain-boundary films have been confirmed by many HRTEM observations [KLE97, CAN97] and are in agreement with an important model calculation conducted by Clarke [CLA87] who investigated the force balance at grain boundaries and predicted the amorphous films with an equilibrium thickness in Si₃N₄-based material. Ambiguity arises

when SiC-based materials are taken into consideration. Clarke's model predicts that no amorphous film will be stable at grain boundaries of SiC-based materials. The prediction has been approved by some TEM observations [CAR91], but is contrary to others [FAL97, TUR96] where the stable amorphous grain-boundary films have been clearly found. The ambiguity or the contradiction raised in case of SiC-based materials is likely to be due to the fact that interfacial reactions and crystallization behavior are rendered rather complicated by the presence of C. Therefore, in-depth investigation of the microstructure and chemistry of the intergranular phases in SiC-based ceramics with a lateral resolution on the order of nanometers is worthwhile and forms the main topic of this thesis.

The thesis is organized as follows: a review of previous work on structural properties of SiC crystals, sintering of SiC-based ceramics with the emphasis on liquid-phase sintering, the overall microstructure of sintered SiC and, more specifically, the grain-boundary films and triple-junction phases of liquid-phase sintered SiC will be given in Chapter 2. The electron microscopic methods as most important part of the experimental procedures are introduced in Chapter 3. Sintering procedures and other experimental methods are different for the different systems investigated and therefore are described separately in the corresponding chapters. The model system SiC-SiO₂ is discussed in Chapter 4 with the main objective to understand the behavior of grain-boundary films within the framework of the Clarke's model [CLA87]. To identify the composition of triple-junction phases of SiC-based ceramics, the model system using coarse SiC powder as starting material for sintering was investigated and is discussed in Chapter 5. Detailed investigations on the intergranular phases of the technologically relevant system SiC-Y₂O₃-AlN by using TEM, HRTEM and EELS methods are described in Chapter 6. The densification, phase transformation, effect of sintering atmospheres, segregation at grain-boundary films and elemental distribution across triple-junction phases are discussed. Finally, in Chapter 7, conclusions from the investigations of Chapter 4, 5 and 6 are drawn.

2 REVIEW OF SINTERING AND MICROSTRUCTURES OF SiC-BASED CERAMICS

2.1 Structural properties of SiC

The basic structural unit of SiC polytypes consists of a primarily covalently bonded (88% covalent and 12% ionic) tetrahedron of four C atoms with a silicon atom at the center or vice versa (Figure 2.1). The bond length of Si-C is approximately 1.89 Å. The SiC crystals are constructed with these tetrahedra joined to each other at the corners.

The structure of SiC crystals can be simulated by stacking sheets containing close-packed spheres. Each sheet represents a bilayer composed of one layer of Si atoms and one layer of C atoms. The differences among the polytypes arise only from the type of stacking of these sheets in the direction of the c-axis. Using the notation for hexagonal crystal symmetry, the first sheet can be defined as the basal plane with Miller-indexed directions according to Figure 2.2. The most stable way to stack an identical second sheet of close-packed spheres is to place the spheres atop the ‘valleys’ of the first sheet. The second sheet may be displaced along $[\bar{1}100]$ until the spheres lie in the valleys denoted ‘B’ in Figure 2.2, or the sheet may be displaced along $[1\bar{1}00]$ until the spheres lie in the valleys denoted ‘C’ in Figure 2.2. Thus, a sheet can be denoted A, B, or C, depending on the positions of its spheres. All polytypes can be described as different stackings of A, B, and C sheets, with the restriction that sheets with the same notation cannot be stacked upon each other.

A large number of hexagonal, rhombohedral and cubic SiC polytypes exist, with some having stacking sequences of several hundreds of Si-C bilayers [FIS90]. The two most simple stacking sequences are ...ABAB... and ...ABCABC..., which produce the hexagonal wurtzite structure (with the stacking along the [0001] direction) (see Fig. 2.3) and the cubic zinc-blende structure (with the stacking along the [111] direction), respectively. The zinc-blende structure is the only cubic polytype, referred to as β -SiC, whereas the hexagonal and rhombohedral polytypes are collectively referred to as α -SiC.

In the Ramsdell notation [RAM47], a number indicating the periodicity in the stacking direction (i.e., the number of sheets A, B, and C needed to define the unit cell) is followed by a letter indicating the crystal symmetry, C for cubic, H for hexagonal, or R for rhombohedral. According to this notation, β -SiC is represented by 3C, while wurtzite is 2H. Table 2.1 shows several basic SiC polytypes as described by the notation systems introduced above.

2.2 Sintering of SiC

2.2.1 Difficulties in sintering

Sintering is the most common process for the production of SiC, but due to the highly covalent bonding character of SiC (see Section 2.1), this is also very difficult without the aid of sintering additives.

A necessary condition for sintering to occur is that the grain boundary energy γ_{gb} be less than twice the solid/vapor surface energy γ_{sv} [GRE76]. In case of three grains surrounding a pore, γ_{gb}/γ_{sv} should be smaller than $\sqrt{3}$. Only when this condition is satisfied, mass transport can lead to a reduction of excess energy by the formation of grain boundaries from surfaces, followed by grain boundary migration and pore shrinkage. In covalent materials including SiC, as pointed out by Prochazka [PRO87], the grain boundary energy γ_{gb} is so high that pore shrinkage and densification are practically inhibited.

Another thermodynamic sintering theory was proposed by Inomata [INO82] by considering the free energy of the sintering powder. According to the theory, sintering is the process in which surfaces are transformed into interfaces; it is the excess free energy of the powder surfaces and interfaces that drives the densification-related mass transport. Since the relaxation of surface energy by the formation of SiC crystal interfaces is extremely small, Tanaka [TAN91] concluded that SiC is fundamentally a non-sinterable material and sintering additives to alter the free energy are required for its densification.

Extremely low self-diffusion coefficients ($\sim 10^{-11}$ cm²/s for C and $\sim 10^{-13}$ cm²/s for Si) arising from the high degree of covalency of SiC [HON79] is the kinetic reason for the limited mass transport. Diffusion-controlled solid-state densification is therefore actually infeasible for pure SiC.

Coarsening, rather than densification, is preferred during the sintering of SiC, which also constitutes a kinetic difficulty for complete densification. This is because SiC has a relatively high vapor pressure [PRO58]. Smaller grains, with their small radii of curvature, tend to ‘evaporate’ and ‘condense’ on the larger particles, resulting in coarsening of the microstructure without the elimination of pores.

Therefore, sintering techniques making use of additives have to be adopted. With different additives, sintering can occur in the absence or presence of a liquid phase, which is referred to as solid-state sintering or liquid-phase sintering, respectively.

2.2.2 Solid-state sintering

The first to describe the sintering of SiC powders were Alliegro et al. [ALL56]. They used hot-pressing and showed that additives are required for sintering. Prochazka [PRO75] first developed pressureless solid-state sintering of SiC by using a small amount of B and C additives. Later on, full density was also achieved through substituting part of the boron by aluminum [SCH80] and beryllium [SMO79]. Today, pressureless sintering with B-C additives has become a key technology for the manufacturing of SiC ceramics for application as wear resistant components.

The effect of B and C during the sintering process was explained by Prochazka [PRO75] based on a thermodynamic model. C was thought to remove SiO₂ from the SiC powder surface by carbothermal reduction, thereby increasing the solid/vapor interface energy γ_{sv} , while B was assumed to accumulate at grain boundaries to decrease the grain boundary energy γ_{gb} . Considering a typical situation where a pore is surrounded by three grains (see Fig. 2.4), increase of γ_{sv} and decrease of γ_{gb} would favour the pore shrinkage. Therefore, the combined effect of B and C on the interfacial energies largely accelerates the pore shrinkage and improves the densification.

Uncertainties and arguments, however, have always existed with regard to this explanation. Tanaka [TAN84] argued that C also acts to reduce the grain boundary energy, since a certain amount of C is always required independent of the initial oxygen content of the powder. Lange [LAN76] discussed the effect of B and C as liquid-phase sintering process. In SiC containing Al, B and C as additives, sintering has been recognized also as liquid-phase sintering [CAO96, SHI85]. The positive effect of B and C on the self-diffusion in SiC can also be the reason for the improved densification [BIR86].

Low fracture toughness (2-3 MPa \sqrt{m}) of the resulting materials and high processing temperatures (>2100°C) that easily result in exaggerated grain growth are the main disadvantages which restrict the application of the solid-state sintering process. Both α -SiC and β -SiC can be solid-state sintered to full density by adding B and C. However, no significant effect on the mechanical properties is caused by the difference in polytype structures [SUZ86].

2.2.3 Liquid-phase sintering

If the eutectic temperature of the sintering additives is lower than the sintering temperature, a liquid phase will form and spread among the SiC grains upon melting, leading to liquid-phase

sintering. Liquid-phase sintering offers two significant advantages over solid-state sintering: first, it requires lower process temperatures; second, it results in more uniform densification and fine-grained microstructures can be achieved more easily. Liquid-phase sintering of SiC is normally performed at temperatures around 1850-2000°C. Techniques related to liquid-phase sintering include pressureless sintering, gas-pressure sintering (GPS), hot-pressing, and hot-isostatic pressing (HIP).

2.2.3.1 *Liquid-Phase Sintering Mechanisms*

The mechanisms of liquid-phase sintering processes have been described in detail by Kingery [KIN59-1, KIN59-2], Petzow [PET76] and German [GER85]. The sintering process can be treated as a sequence of three stages:

(1) Particle rearrangement

Significant densification results from particle rearrangement in an early stage as soon as the liquid is formed and wetting occurs. The rearrangement of the particles is driven by capillary forces. Parameters like the quantity of liquid, green density, sintering temperature, wetting, etc. strongly effect this stage, which proceeds rather rapidly. If enough liquid phase is formed and wetting is sufficient, full densification can be achieved almost instantaneously.

(2) Solution-precipitation

Dissolution and reprecipitation of the solid phase dominate the microstructural development including densification, shape accommodation and grain growth. It is the chemical potential gradient that induces the dissolution of grains with a small surface radius and their reprecipitation on such with larger ones during microstructure development. Because the diffusivities in a liquid are orders of magnitude higher than those in a solid, the kinetics of densification are much faster than in the case of solid-state sintering. It is worth noting that in addition to densification, coarsening due to Ostwald ripening will occur simultaneously during the solution-precipitation process.

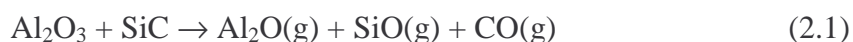
(3) Skeleton sintering

Once a rigid skeleton of contacting particles is formed, solid-state sintering rate-controlled by grain boundary diffusion starts. The overall shrinkage or densification rates are significantly reduced, and the microstructure approaches stable.

These three stages are overlapping as shown schematically in Figure 2.4. Particle rearrangement is always the fastest compared to the other two stages.

2.2.3.2 Sintering Additives

As early as 1975, SiC was hot-pressed to 99% relative density by using Al₂O₃ as sintering additive [LAN75]. During sintering Al₂O₃ was thought to form an oxide melt with the silica that is always present on the surface of SiC powder because of oxidation. Suzuki [SUZ91] optimized this process by using pressureless sintering. The reason for using Al₂O₃ as a sintering additive was that it has a reasonably high melting temperature and superior mechanical properties compared to other oxides. However, as mentioned by Mulla [MUL94], the reaction between SiC and Al₂O₃ according to



is a major problem associated with sintering in this system since the formation of volatile components and retarding densification. An innovative approach to the pressureless liquid-phase sintering of SiC was initiated by Omori and Takei in 1982 [OMO82, OMO85, OMO86], who showed that a wide variety of rare-earth oxides, in combination with Al₂O₃ and/or boron compounds, could be used as sintering additives to promote the densification of SiC. The most frequently used additive system is Al₂O₃-Y₂O₃, not only because of the low eutectic temperature which exists at an Y₂O₃ content of 20 mol% (T_m = 1816°C, or even lower when considering the presence of silica) [GRO94], but also because an optimized microstructure consisting of elongated α-SiC grains and YAG (Y₃Al₅O₁₂) as an intergranular phase can be obtained, resulting in improved mechanical properties such as fracture toughness [KIM97, PAD94-1, KRS95, LEE94]. Other Al₂O₃-containing additive systems are Al₂O₃-Y₂O₃-CaO [MIT96], Al₂O₃-Al₄C₃ [CAR91, HUA86, JAC88, JOU91], and Al₂O₃-C [SAK88]. Recently increasing attention has been paid to the incorporation of N into the intergranular phase of liquid-phase sintered SiC. AlN, as a source of N, was used as sintering additive together with Al₂O₃ and Y₂O₃ [NAG00] or simply with Y₂O₃ [RIX00, KEP98]. During liquid-phase sintering, AlN forms low-melting eutectic composition with Y₂O₃ [JEU93] and/or Al₂O₃. When N₂ is used as sintering atmosphere, compared with pure oxide additives which may lead to strong decomposition reaction (e.g. Equation 2.1), oxide/nitride additives are more stable because the decomposition reaction



can be suppressed effectively by N₂ overpressure. Moreover, incorporation of N into the intergranular phase is reported to retard the β-to-α SiC phase transformation and suppress grain growth [JUN97, KIM99-2]. Si₃N₄ [TUR96] and prereacted oxynitride glass [KIM99-2] also were added for sintering SiC. The former requires the HIP process for densification whereas the latter allows densification at as low as 1800°C.

The non-oxide system Al-B-C also provides sintering additives for the liquid-phase sintering of SiC. Methods of addition include direct mixing of aluminum, boron, and carbon with SiC powders [DUV93, MOB96, CAO96], formation of an Al solid solution in the SiC powder [TAN85], and using the AlB₂ [COP78] or Al₄C₃ and B₄C compounds [ZHO99]. The addition of aluminum not only initiates densification at substantially lower temperatures than boron and carbon alone but also enhances the β -to- α phase transformation [SHI85, WIL85] and the transformation of 6H-SiC to 4H-SiC [TAN00].

2.3 Microstructure features of liquid-phase sintered SiC

Although the observed as-sintered microstructures strongly depend on the preparation route and processing parameters utilized, there are a number of microstructural features which are characteristic for liquid-phase sintered SiC-based materials. Typically, the microstructure is composed of SiC grains, amorphous grain-boundary films between adjacent SiC grains, and phases at triple junctions of SiC grains. The latter two types of phases are also in general referred to as intergranular phases. It is worth to note that in some reports grain boundaries with direct crystal/crystal contacts and (at least locally) no grain-boundary films were shown [CAR91]. Figure 2.5 depicts a schematic microstructure of a liquid-phase sintered SiC ceramic, giving an impression of the above mentioned phases. Microstructural features related to SiC phase transformation, grain coarsening, and the effect of sintering atmosphere will be reviewed in this chapter, while grain-boundary films and triple-junction phases will be covered in the next chapter .

2.3.1 Phase transformation

For the liquid-phase sintering of SiC ceramics, α -SiC has been widely used as starting powder [OMO82, CUT89, COR90, CHI91, SIG93] because α -SiC usually results in fine, equiaxed microstructures. When the fracture toughness of the sintered body is concerned, however, the use of β -SiC is preferred as the starting powder because the β -to- α phase transformation at high temperatures results in a microstructure with interlocking plate-like grains [PAD94-1, LEN97]. Platelet-like shaped grains have been shown to increase the fracture toughness of SiC by crack bridging [PAD94-2, KIM95] or crack deflection [MUL94]. The transformation can be accelerated by adding some α -SiC as transformation seeds in the starting powders [LEE94, KIM98], while in contrast, it can be retarded by incorporating N into the intergranular glass phases [JUN97, KIM99-1]. When sintering additives from the Al-B-C

system are used, Al firstly enhances the β -to- α phase transformation, and secondly dissolve into the SiC crystal, cause the transformation of 6H-SiC to 4H-SiC, and accelerate anisotropic grain growth [TAN00, ZHO99]. A reverse α -to- β phase transformation in SiC was also found when 10 wt% of Si₃N₄ were added and the material was hot isostatically pressed at 2100°C [TUR96]. The N-containing liquid phase arising from melting of surface SiO₂ and dissolution of Si₃N₄ during sintering was supposed to cause the transformation.

2.3.2 Coarsening and solution-reprecipitation process

Sigl and Kleebe [SIG93] were the first to report about details of the “core/rim” structure of SiC grains which experimentally verified the sintering mechanism in liquid-phase sintered SiC to be solution-reprecipitation. They showed that the dissolved SiC would re-precipitate onto the undissolved ‘core’ SiC grains during sintering, forming a ‘rim’ region; the difference between core and rim is clearly visible in polished and plasma-etched sample cross sections, because the rims are no longer pure SiC but contain small amounts of Y, Al and O incorporated from the liquid phase. The same characteristic structures were also observed by Ye et al. [YE99] and Biswas et al. [BIS01]. They both referred to the explanation from Sigl and Kleebe [SIG93] and concluded moreover that the solution-reprecipitation process was controlled by interfacial reactions, rather than by atomic transport through the melt. This conclusion was drawn on the basis of different experimental methods. However, in the former work [YE99], it was found that grain growth of SiC was independent of the quantity of the liquid intergranular phase, while in the latter paper [BIS01], it was proved that along with the increasing viscosity of the oxynitride intergranular liquid, the rate of grain growth increased, while it would have decreased if atomic transport through the viscous liquid had dominated the kinetics of the solution-reprecipitation process. A different opinion, however, was proposed by Falk [FAL97] who did not find any detectable incorporation of Y, Al or O into the SiC grains, although she also found indications for the occurrence of solution-reprecipitation processes by analyzing the shape of SiC grains.

2.3.3 Effect of sintering atmosphere on microstructures

The sintering atmosphere is a significant processing factor for liquid-phase sintering. Vacuum is theoretically preferred for liquid-phase sintering, since gas bubbles might be enabled to leave the liquid phase, which otherwise would inhibit full densification [GER85]. A gas atmosphere, however, is generally utilized for the suppression of decomposition reactions,

reduction of weight loss, microstructure design and some technical reasons, for example, protection of heating elements. Ar and N₂ are the most frequently used atmospheres for the sintering of SiC-based materials. Previously, sintering in N₂ was found more difficult than in Ar because dissolution of N₂ into the liquid intergranular phase would increase its viscosity and hinder grain rearrangement and atomic transport; higher temperature is therefore needed for full densification [PRO79, JAC88]. However, when N-containing additives such as AlN were adopted for sintering, a N₂ atmosphere was not only able to improve the densification by suppressing the decomposition reaction of AlN [CHI94, NAD95, BIS00], but also beneficial for producing fine-grained SiC with high strength since the high viscosity of N-containing melts retard the β -to- α phase transformation and inhibit grain growth [JUN97, KIM99-2, NAG00]. To suppress the gas-forming reaction between SiC and oxide additives, CO was sometimes used as (or part of the) sintering atmosphere. A small partial pressure of CO gas can largely reduce the weight loss and increase the density of the sintered products [MUL94].

2.4 Grain-boundary films and triple-junction phases of SiC ceramics

2.4.1 Stability of grain-boundary films in ceramic materials

Since amorphous grain-boundary films were first observed in MgO-fluxed Si₃N₄ by Clarke and Thomas [CLA77] using high-resolution transmission electron microscopy, similar observations have also been reported for Al₂O₃ [HAN83], ZnO₂ [RÜL84] and many other ceramics. Along with the improvement of TEM-related techniques, extensive studies on the grain-boundary films have been performed during the last ten years. At first sight, the presence of glassy films between two grains in liquid-phase sintered ceramics appears to be a kinetic, non-equilibrium phenomenon, comparable to large glass pockets between several grains. But the invariable existence of these films under various experimental conditions indicate that they might be in a state of thermodynamic equilibrium. A model devised by Clarke [CLA87, CLA93] to explain this phenomenon suggests that such amorphous films have an equilibrium thickness as a result of an intricate force balance between attractive Van der Waals forces across the grain boundary and repulsive steric, capillary, and electric double-layer forces within the film. The calculated film thicknesses based on Clarke's model are generally on the order of 1-2 nm, which is in agreement with most of the previous experimental observations. Numerous studies followed the publication of the Clarke model. Kleebe et al. [KLE92, KLE93] and Tanaka et al. [TAN94] demonstrated that the equilibrium thickness of such films in Si₃N₄ ceramics depends sensitively on film composition (e.g. on

doping with Ca^{2+}); however, for a given composition, the film thickness was constant and independent of grain misorientation. Vetrano et al. [VET93] observed Si_3N_4 materials in which the triple-junction phases had been devitrified by annealing, while the grain-boundary films still remained amorphous and kept their equilibrium thickness. Wang and Chiang [WAN98] produced a film-free $\text{ZnO-Bi}_2\text{O}_3$ composite by hot-pressing under 1 GPa pressure, then annealed it and found that the amorphous films re-appeared at the grain boundaries, which indicates that the grain-boundary film has a lower free energy than crystal-crystal grain boundaries and is therefore thermodynamically stable. Theoretical work using molecular-dynamics simulations has been conducted by Koblinski, et al. [KEB97] to understand the thermodynamic stability of the amorphous grain-boundary films in covalent ceramics. They suggested that grain-boundary films do not require impurities for their stabilization and that their existence in high-energy boundaries can be attributed to thermodynamics alone. Several other theoretical works from different angles of view, dealing with the thermodynamic equilibrium of grain-boundary films [BOB99, BRAD97, CAN97, GOL02], were also carried out and indicate the strong recent attention focused on this phenomenon. The significance of the presence and stability of grain-boundary films in materials is tremendous. While the melted state of the grain-boundary films at elevated temperatures significantly improves the densification behaviour because of liquid-phase sintering mechanisms, its solidified state present in the sintered materials strongly affects the mechanical and physical properties, e.g., creep resistance and fracture toughness of structural ceramics [RAJ93, WIE99, BEC98, SUN98, CAO96], or electrical properties of thick-film resistors [CHIA94], varistors [GREU95] and high- T_c superconductors [RAM90]. Thus, in-depth understanding and tailoring of the behavior of grain-boundary films would be extremely valuable for materials development.

2.4.2 Grain-boundary films in liquid-phase sintered SiC

Grain-boundary films in SiC ceramics are much less understood than those in Si_3N_4 . Clarke particularly discussed the behavior of liquid silica films between SiC grains when proposing his force-balance model [CLA87]. He found that SiC is the only material where the attractive Van der Waals force is larger at all distances than the repulsive steric force, as it is indicated by the high refractive index of SiC. Therefore, it was concluded that the liquid silica film would not be stable between SiC grains. Accordingly, the theoretical result, that siliceous films in SiC ceramics have a zero equilibrium thickness, is in agreement with the experimental results in so far that up to date no SiC ceramic has been observed by TEM to contain a glassy grain-boundary phase.

Clarke's model calculations were experimentally tested by Carpenter and Braue [CAR91] who indicated that in liquid-phase sintered SiC using Al₂O₃ and A₄C₃ as sintering additives, grain boundaries are found to be free of glassy phases by high resolution TEM. Sigl and Kleebe [SIG93], who found that the equilibrium film thickness can be affected by the variation of the chemical compositions of adjacent grains, also concluded that their observation was consistent with Clarke's model. However, they didn't comment on the fact that they also found amorphous films with a thickness of 1 nm at 6H-SiC/6H-SiC grain boundaries. It was Turan and Knowles [TUR95, TUR96] who pointed out that there is a contradiction between Sigl and Kleebe's observation and Clarke's model. They produced a SiC/Si₃N₄ composite and revealed that grain-boundary films always existed in the composites made from as-received powders, while film-free boundaries were present in those made from deoxidized powders. The silica layer on the surface of SiC powders was apparently significant for the formation of grain-boundary films. Considering the apparent contradiction to Clarke's model, they supposed that small amounts of dissolved SiC and nitrogen might be the reason for the stabilization of the grain-boundary films.

Several reports [PEZ98, KLE92, DUV93] show that both grain-boundary films and film-free boundaries can be observed in SiC-based ceramics. Different factors seem to decide about the presence or absence of the grain-boundary films. For example, Kleebe [KLE92] indicates that using Al₂O₃ instead of AlN as sintering additive can cause the occurrence of amorphous grain-boundary films, while Pezzotti et al. [PEZ98] show that doping with B and C is beneficial for a depletion of grain-boundary films. More literature sources, however, report that grain-boundary films with a thickness around 1 nm are always present in liquid-phase sintered SiC-based ceramics [FAL97, FAL98, WAN97, KAN99, MOB96, NAG00, MOB98, CAO96]. The difference in sintering additives or sintering processes might affect the equilibrium thickness of the films within a small range, but is not likely to completely remove the grain-boundary films.

The composition of grain-boundary films is complicated and difficult to be identified because of their atomic scale dimensions. A common idea is that a surplus of O and cations originating from the metal oxide/nitride additives can be present in the grain-boundary films through segregation [FAL98, PEZ00]. On the other hand, the effects of C and/or N in grain-boundary films remain unclear. Some reports showed the grain boundaries did not contain C and N because C disappeared by reaction with the SiO₂ glass present on the grain surfaces [BRAU94], and N-containing liquid phases did not completely wet the grain boundaries.

Others, however, argue that C and/or N could indeed stably exist in grain-boundary films by forming oxycarbide [KAN99] and/or oxynitride glasses [NAG00].

Like for other ceramics, tailoring the structural width and chemistry of grain-boundary films could fundamentally vary the physical properties of the SiC-based materials and is therefore a very significant task.

2.4.3 Triple-junction phases and their crystallization

It is well established that the presence of amorphous intergranular phases due to liquid-phase sintering limits the high-temperature properties of non-oxide ceramic materials [CLA82, PIE86], which is closely related to the properties of the intergranular phases such as thermal stability, softening at high temperatures and oxidation resistance. One possibility to reduce the amount of amorphous phases is to crystallize them, especially in the region of triple junctions, through a post-sintering heat treatment or a controlled sintering cycle. However, only partial crystallization can be achieved due to several reasons: (1) the composition of the intergranular phases may shift during processing into regions of the phase diagram at which the crystallization capability is low [BON87]; (2) contrary to crystallization of bulk glasses the volume change of intergranular phases during crystallization is constrained by surrounding grains, as a result of which the internal stress can build up a thermodynamic barrier for complete crystallization [RAJ81]; (3) even if the volume mismatch stresses can be relaxed through mass transport between grain-boundary films and triple-junction phases, kinetic hindrance of crystallization has to be taken into account [KES92]. With regard to SiC-based ceramics, it is therefore not surprising that even after the crystallization of triple-junction phases, amorphous phases can always be found between the secondary crystalline phases and surrounding SiC grains [WAN97, FAL97]. The distribution of the chemical elements in the triple junctions is strongly affected by the crystallization of the triple-junction phases. When Al_2O_3 and Y_2O_3 are used as sintering additives, crystallization of Y-Al-garnet (YAG) can cause a depletion in Y of the residual glass at triple junctions and grain boundaries [FAL97]. Graphite was frequently detected in the residual glass as a consequence of the decomposition of SiC [FAL97] and/or excess free carbon in the starting powders [PEZ98]. Incorporation of N into the triple junctions leads to the formation of an oxynitride glass phase, which, when crystallized, forms N-containing solid solutions, as for example $\text{Y}_{10}\text{Al}_2\text{Si}_3\text{O}_{18}\text{N}_4$ [KEP98]. In spite of these results more detailed investigations are required on the N-containing triple junctions in SiC ceramics.

Table 2.1 Different notations for the SiC polytypes [JÄR98]

Ramsdell notation	3C	2H	4H	6H	15R
Structure	Zinc-blende	Wurtzite			
Type	β	α	α	α	α
Stacking sequence (ABC notation)	ABC...	AB...	ABCB...	ABCACB...	ABCBACABA CBCACB...

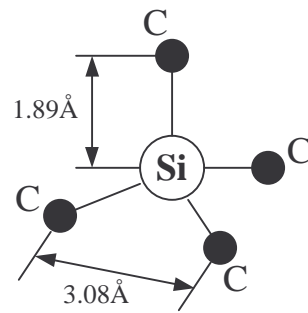


Fig. 2.1 Basic structural unit of SiC, consisting of a tetrahedron of four carbon atoms with a silicon atom in the center.

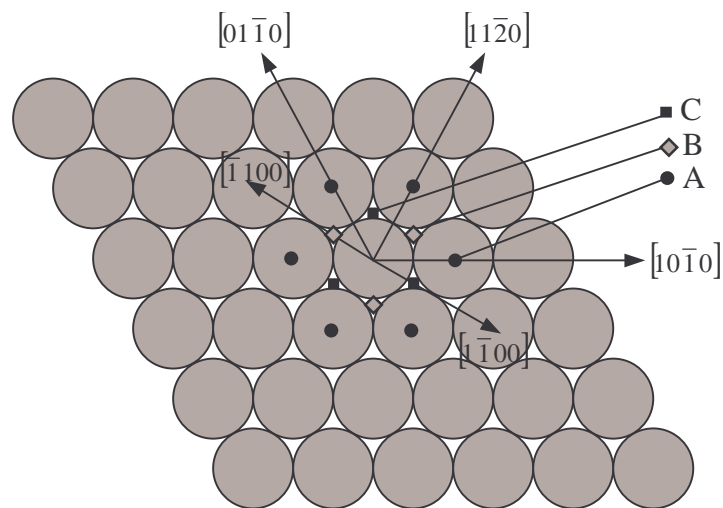


Fig. 2.2 A close-packed hexagonal plane of spheres, with the sphere centers marked by A. A second and identical plane can be placed atop the first plane, with either the sphere centers marked by B or those marked by C. More planes can be stacked by obeying the same rules to form the final structure. Miller indexes are used to indicate the direction of displacement.

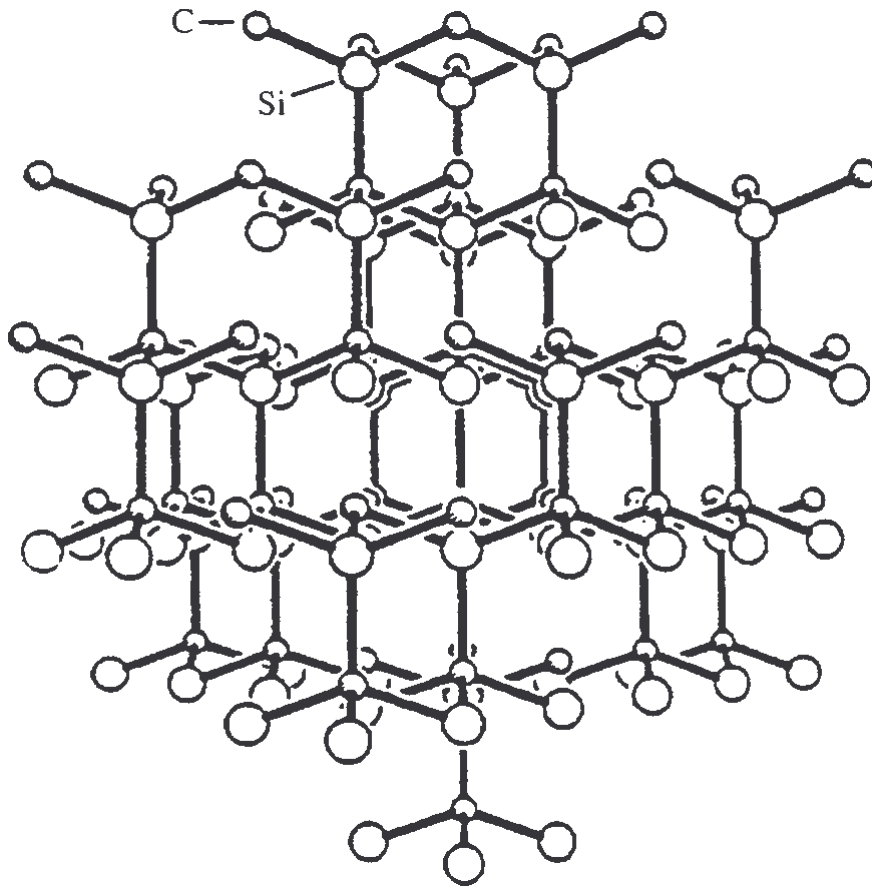


Fig. 2.3 Structure of hexagonal SiC which crystallizes in the wurtzite structure (from BAR97).

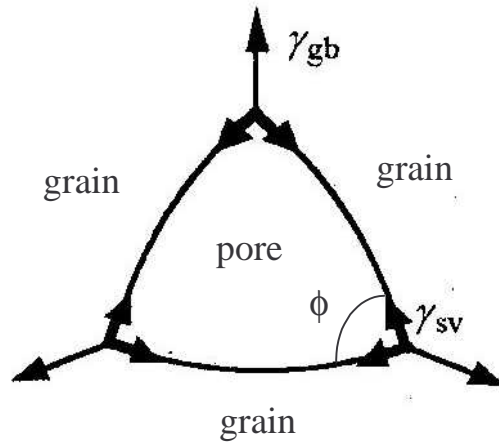


Fig. 2.4 Illustration of a pore surrounded by three grains during the liquid phase sintering process. γ_{sv} is solid/vapor surface energy, γ_{gb} is grain boundary energy, and ϕ is dihedral angle. Increase of γ_{sv} and decrease of γ_{gb} are beneficial to the pore shrinkage. It is worth noting that the figure is a 2-dimensional section through the microstructure; a real pore will be surrounded by more grains.

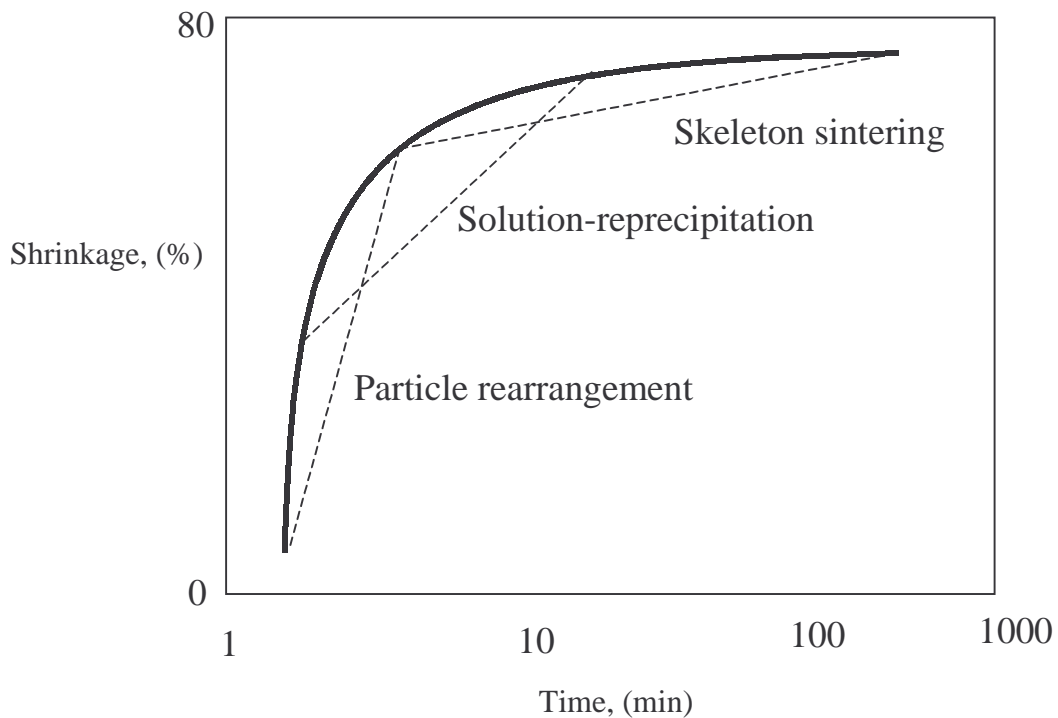


Fig. 2.5 Time dependence of shrinkage as a result of the liquid-phase sintering mechanisms.

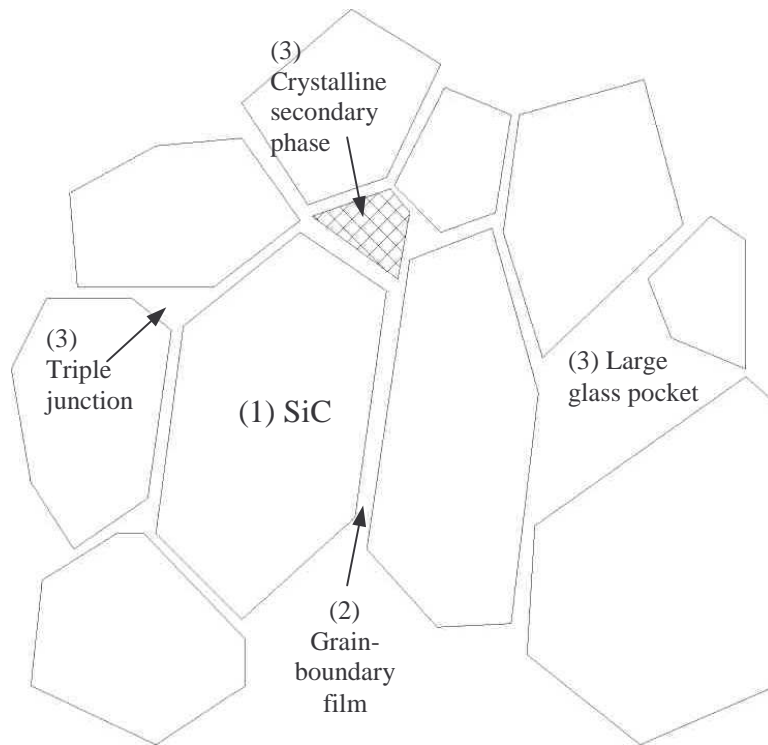


Fig. 2.6 Schematic microstructure of a liquid-phase sintered SiC ceramic, consisting of (1) SiC grains, (2) amorphous grain-boundary film between two SiC grains and (3) different phases at triple junctions and pockets between several adjacent SiC grains.

3 CHARACTERIZATION METHOD – ELECTRON MICROSCOPY

Electron microscopy methods with sub-micrometer or nanometer resolution, as an important part of the experimental procedures to investigate the microstructure and chemistry of the SiC-based materials, are introduced in the present chapter.

3.1 Interactions between electrons and matter

When a specimen is hit by a finely focused electron beam, there will be a rich variety of interactions between electrons and matter in the specimen, which constitutes the basis for electron microscopy. A wide range of signals are emitted during the interactions, and some of these are summarized in Fig. 3.1. These signals can be collected by specific detectors and used to derive a wealth of important information about the specimen.

The electron-matter interactions can be divided into two classes:

1. Elastic scattering events affect the trajectories of the beam electrons inside a specimen without altering the kinetic energy of the electrons. In scanning electron microscopy (SEM), elastic scattering is responsible for the phenomenon of electron backscattering that forms an important imaging signal. In transmission electron microscopy (TEM), elastically scattered electrons are the major source of contrast in images and also create the intensity distributions in diffraction patterns.
2. Inelastic scattering events result in a transfer of energy from the beam electrons to the atoms of the specimen, leading to the generation of secondary electrons for SEM, Auger electrons for surface microanalysis, inelastically scattered electrons for electron energy-loss spectrometry (EELS), characteristic X-rays for microanalysis (EDS and WDS), bremsstrahlung X-rays, electron-hole pairs, plasmons, phonons, and so on.

In above descriptions of electron scattering, the electron beam is treated as a succession of particles, but when considering electron diffraction, it must be treated by wave theory. Electron diffraction, based on the wave aspect of electrons, has become an indispensable part of TEM and is an extremely useful tool for studying the crystallography of minute-sized crystals.

The region of the specimen in which the incident electrons interact with the matter, depositing energy and producing the signals for measurement is known as the interaction volume. The interaction volume is influenced by the electron beam energy, the atomic numbers of the involved atoms, and specimen tilt. The concept of interaction volume is important to the

microanalysis combined with SEM or TEM because it determines the spatial resolution of the analysis.

3.2 Scanning electron microscopy and X-ray microanalysis

The scanning electron microscope and electron microprobe are powerful instruments which permit the observation and characterization of specimens in many regards: composition, surface topography, crystallography, etc. In the SEM, the signals of greatest interest are the backscattered electrons and the secondary electrons. The backscattered electrons provide the atomic number contrast (also called Z contrast) for the SEM image and respond to the local composition of the specimen. The secondary-electron emission is confined to a volume close to the beam's impact area, permitting images to be obtained at relatively high resolution. In the electron microprobe, the primary signal of interest is the characteristic X-rays emitted as a result of the electron bombardment. The analysis of the characteristic X-rays can yield both qualitative identification and quantitative compositional information from regions of a specimen as small as one micrometer in diameter. Two kinds of spectrometers are used to analyze the characteristic X-rays: the wavelength-dispersive spectrometer (WDS) and the energy-dispersive spectrometer (EDS). Neither WDS nor EDS is the ideal spectrometer in all situations. For example, for WDS, the X-ray collection efficiency is low and the time required for analysis is long; for EDS, the energy resolution is worse than that of WDS and it is more difficult to detect light elements ($Z < 10$). So the choice of the spectrometer according to the particular situation is important. Sometimes the combined usage of WDS and EDS is necessary to achieve maximum capabilities for analysis.

The scanning electron microscope most frequently used in this thesis is the Zeiss DSM982 Gemini, equipped with a thermal Schottky field emission cathode. EDS is interfaced with the SEM. For measuring the composition of the intergranular phase in the model system 'coarse SiC with Y_2O_3 -AlN additives', a SEM combined with WDS (SX100, Cameca) was used. The spatial resolution of WDS is about 1 μm . The specimens for SEM observation and EDS and WDS analyses were ground and polished to a 1 μm surface finish. While plasma etching and carbon coating were performed to obtain better contrast and avoid charging effects in the SEM images, no etching or coating was conducted before WDS analysis in order not to affect the precise measurement of the composition.

3.3 Transmission electron microscopy

It was Knoll and Ruska who built the first electron microscope of the world in Berlin in the early 1930s. In their paper [KNO32] the term ‘electron microscope’ was first used, and the idea of electron lenses and electron images was first developed into the practical reality. Several years later commercial transmission electron microscopes were built in the UK, 1936, and in Germany, 1939. Now a days transmission electron microscopes became widely available from several sources (Hitachi, JEOL, FEI, and RCA, etc.). A theoretical textbook often referred to as the ‘bible’ of TEM was written by Hirsch et al in 1977 [HIR77]. The practical applications of TEM in materials science were pioneered in the United States by Thomas [THO62], later by Edington [EDI76] and by Thomas and Goringe [THO79]. In 1996 Williams and Carter published the latest fundamental textbook of TEM for material science [WIL96].

A transmission electron microscope can appear in several different forms, including conventional transmission electron microscope (CTEM), high resolution transmission electron microscope (HRTEM), scanning transmission electron microscope (STEM), and analytical electron microscope (AEM). It is usual to divide the TEM into three components: the illumination system, the objective lens/stage, and the imaging system.

The illumination system comprises the gun and the condenser lenses and its role is to extract the electrons from the source and transfer them to the specimen. There are two kinds of electron guns available: thermionic gun (using tungsten or LaB₆ filaments) and field-emission gun (FEG). The electrons emitted from the electron gun are condensed by magnetic lenses to form the electron beam. Two principal modes of the electron beam can be obtained by adjusting the condenser lenses: parallel beam and convergent beam. The first mode is used for conventional TEM imaging, diffraction and HRTEM imaging, while the second is used for STEM imaging, microanalysis and convergent-beam electron diffraction (CBED). Some instruments are only capable of operating in convergent beam mode and are referred to as ‘dedicated STEM’.

The objective lens/stage system is the heart of the TEM. Here is where all the beam-specimen interactions take place (cf. section 3.2) and bright-field (BF) and dark-field (DF) images as well as selected-area diffraction patterns (SAD) are created. Fig. 3.2 shows the two basic modes of operation of the TEM: imaging and SAD. It is also here that the convergent beam is scanned over the specimen to form STEM images and diffraction patterns. The quality of the image formed by the objective lens controls the resolution of the final image.

The imaging system uses several lenses to magnify the image or the diffraction pattern produced by the objective lens and to focus these on the viewing screen. To date, TEM images and diffraction patterns are still mainly viewed at fluorescent screen or TV/CRTs and recorded on photographic film as analog images. It can be speculated that most analog detection, recording, and storage of TEM results will eventually be replaced by digital methods.

Combination of electron diffraction and imaging is one of the greatest advantages of TEM, enabling TEM to determine crystallographic orientations locally (at the nanometer level). Another advantage is the high resolution of the TEM image. The resolution of a TEM is the smallest distance between two points that the TEM can resolve, depending on the wavelength of the electrons. Since the wavelength of electrons is related to their energy, the high accelerating voltage of TEM may get an electron beam with small wavelength, leading to a very high resolution in TEM image (normally 0.2 – 0.3 nm). For HVEMs which use an extremely high accelerating voltage (between 1MV and 3MV), the resolution can be 0.1 nm or better, achieving so-called atomic resolution. The large depth of field is also an important property for TEM, which means in the TEM the whole thickness of the specimen is usually in focus at the same time. There are many other reasons why the TEM becomes the most powerful tool for material research, at the same time it is important to note that there are many limitations. First, a high resolution automatically means that only a small part of the specimen can be observed at any one time. The higher the resolution, the worse the sampling abilities of the instrument. Thus before performing TEM to get detailed but very local information, it is beneficial to use visible-light microscopy or SEM to obtain a concept about the materials on the whole. Second, interpreting TEM images is difficult and easily misleading. One important reason is that the TEM views specimens in transmission and has no surface-sensitivity and depth-sensitivity. Third, the electron beam with its high voltage can modify or even damage the specimen. Fourth, the TEM requires thin specimens, and thinner is better. But as a general rule the thinning processes do affect the specimen, changing both its structure and its chemistry. This contradiction in the specimen preparation is the major limitation of the TEM. Therefore, only when the limitations of the TEM as listed above are seriously noticed and carefully solved, the advantages of the TEM can be thoroughly exploited in material research.

3.4 High resolution transmission electron microscopy

The HRTEM provides the possibility to observe a specimen on a scale close to the atomic level. Understanding of the relationship between the atomic structure of materials and their

chemical and physical properties can be greatly improved by performing HRTEM. The instruments required for HRTEM include the high voltage electron microscopes (HVEMs) and the intermediate voltage electron microscopes (IVEMs) which operate at 200 to 400 kV, but still offer very high resolution. One example of IVEMs is the JEM 4000EX (JEOL) which has an accelerating voltage of 400 kV and a point resolution of 0.17 nm and is used as the main instrument in this thesis for HRTEM imaging.

The steps necessary to obtain a HRTEM image contain: aligning the instrument well; performing current and voltage centering of the objective lens routinely and frequently at high magnification (e.g. 200,000); finding a thin and clean region of the specimen (the thickness of the region for HRTEM must be smaller than 50 nm, and thinner is better); orienting the specimen so that the beam is aligned along a zone axis; adjusting the focus to minimum contrast; correcting the astigmatism; recording the HRTEM image at high magnification (e.g. 500,000).

A HRTEM image is a kind of phase-contrast image where the contrast arises due to the differences in the phase of the electron waves scattered in a thin specimen. Both HRTEM imaging and BF/DF imaging use the diffracted electron beam to form images. The difference is that: a BF/DF image is formed when one single beam is selected for imaging by using the lens aperture, while a HRTEM image requires the selection of more than one beam. As a result, the contributions of two or more diffracted electron beams cause the appearance of the lattice fringes in the HRTEM image of a crystalline phase. Study of these fringes can provide a large amount of information about the crystal structure and orientation.

The first step of the HRTEM image processing is to improve the appearance of an image with the aid of computers, make it look sharper and show higher contrast, etc. Then the information contained in the image is quantified. Third, the image is simulated by using methods like the fast Fourier transform (FFT) approach. Finally, the quantified experimental image is compared with the computer-simulated image. It is often necessary to repeat the process for several times to establish the final relation between the HRTEM image and the atomic structure of the specimen. The use of computers and appropriate software packages is crucial for successfully conducting the process.

The applications of HRTEM are wide-ranging, for example, in studying structures, nonstoichiometry, interfaces, precipitates, defects, and so on. The HRTEM is especially useful in the present experiments for studying grain-boundary films. Kleebe [KLE97] summarized the three imaging techniques used for measuring grain-boundary films: 1, dark-field imaging, 2, Fresnel fringe imaging, and 3, HRTEM imaging, and concluded that the

HRTEM method shows the highest accuracy and can be used to reproducibly measure the film thickness within ± 0.1 nm. The fundamental requirement for accurate measurement is that the grain boundary plane must be parallel to the electron beam. At the same time the zone axis of the two grains should be parallel to the interface too, in order to produce lattice fringes in both grains. This situation can be achieved by carefully tilting the specimen. The quality of the imaging is strongly affected by the specimen preparation, because the grain-boundary film and grains can be thinned at different rate due to different bonding and density.

3.5 Electron energy-loss spectrometry

EELS is the analysis of the energy distribution of electrons that have interacted inelastically with the specimen. These inelastic collisions yield a large amount of information about the electronic structure of the atoms of the specimen, which in turn reveals details of the bonding of these atoms and their nearest-neighbor configurations. The spectrum of electron energies is examined by using a magnetic prism spectrometer which can be interfaced to either a TEM or a STEM. The magnetic prism is a highly sensitive device with a resolving power of approximately 1 eV even when the energy of the incident electron beam is up to 400 keV. There are two ways to acquire a spectrum. One is to build up the spectrum one channel at a time, which is known as serial-acquisition EELS, or SEELS, the other is to acquire all the channels simultaneously, which is parallel-acquisition EELS, or PEELS. PEELS is much more efficient than SEELS. In the present experiments, a dedicated scanning transmission electron microscope (Model HB501, Vacuum Generators, U.K.) equipped with a Gatan 666 PEELS spectrometer was used to perform EELS analysis. With a cold field-emission electron gun (FEG), the DSTEM has an electron probe size around 0.5 nm and an energy resolution better than 0.7 eV.

The energy-loss spectrum comprises three principal regions:

1. The zero-loss peak, which consists primarily of elastic forward-scattered electrons, but also contains electrons that have suffered minor (unresolvable) energy losses.
2. The low-loss region up to an energy loss of about 50 eV. It contains electrons which have interacted with the weakly bound outer-shell electrons of the atoms in the specimen, e.g. electrons exciting plasmon oscillations.
3. The high-loss region above 50 eV, where electrons have interacted with the more tightly bound inner-shell or 'core' electrons.

The high-loss region contains information about the inner electron shells and characteristics of the atoms in the specimen and therefore is most useful. For the light elements, the edges of energy-loss electrons that have interacted with K shell electrons (K edges) are usually adopted for measurement (in EELS, ‘edge’ is often used in stead of ‘peak’). As Z increases, K shell electrons require more energy for their ejection because they are more strongly bound to the nucleus. So other lower-energy ionizations, such as the L and M edges arising from L and M shell electrons, respectively, can be used. Normally, the L edges are used when the K-shell energy exceeds ~1 keV (Na), and the M edges are used when the L shell exceeds ~1 keV (Zn). Regarding nomenclature, the L_1 edge corresponds to the 2s electrons in the L shell, the $L_{2,3}$ edge to the 2p electrons in the L shell, $M_{4,5}$ edge to the 3d electrons in the M shell, etc. Table 3.1 lists the principal elements measured in this thesis and their characteristic ionization energies.

Qualitative EELS microanalysis is very straightforward. There are few artifacts that can be mistaken for an edge. As long as the spectrum is calibrated, the edge corresponding to a certain element can be unambiguously identified.

For quantitative microanalysis, the background intensity arising from multiple-scattering events must be removed and the partial ionization cross section, σ , should be determined. Curve fitting is one of the common methods to remove the background. The process is shown schematically in Fig. 3.3. It is assumed that the energy dependence of the background has the form:

$$I = A \cdot E^{-r} \quad (3.1)$$

where I is the intensity in the channel of energy loss E, and A and r are fitting parameters. The cross section σ is a measure of the probability of a specific scattering event occurring, which is the sensitivity factor relating intensity of edges (I) to the number of atoms. It is the variation of the cross section with the energy loss E which causes elements with same number of atoms to show totally different edge intensities in the spectrum. Because the cross section is influenced by the choice of collection semiangle β of the spectrometer and by the selection of the energy window Δ (cf. Fig. 3.3), the partial ionization cross section $\sigma(\beta\Delta)$ is actually determined for microanalysis. Either theoretical or experimental approaches can be used for its determination. The detailed processes are given in Egerton’s book [EGE86] and can be performed by using Gatan’s EL/P software.

Then, number density N_k of atoms belonging to a K shell edge can be calculated by

$$N_k = \frac{I_k(\beta\Delta)}{I_l(\beta\Delta)\sigma_k(\beta\Delta)} \quad (3.2)$$

Here, I_K is the K shell intensity after removing the background, I_l is the intensity of the zero-loss and low-loss electrons, both of which are limited by β and Δ .

For a ratio of two elements A and B, the determination of I_l is unnecessary:

$$\frac{N_A}{N_B} = \frac{I_K^A(\beta\Delta)\sigma_K^B(\beta\Delta)}{I_K^B(\beta\Delta)\sigma_K^A(\beta\Delta)} \quad (3.3)$$

The major assumption in the whole approach is that the electrons undergo a single scattering event. In practice, it is difficult to avoid multiple scattering even in very thin specimens. Therefore, the relative error of the quantitative microanalysis can be ± 10 -20%.

3.6 Specimen preparation for TEM

In the present work, all the TEM specimens are prepared starting from bulk materials. A standard procedure for preparation of bulk specimens is followed, which includes cutting, grinding, dimpling, and ion-beam milling. The whole procedure is shown schematically in Fig. 3.4.

(1) Cutting

The bulk SiC-based ceramic is cut by a diamond cutting wheel to get a thin slice with thickness < 1 mm. Then an ultrasonic drill (Gatan Model 601) is used. The cutting tool of the ultrasonic drill is a hollow tube with an inner diameter of 3 mm. As a result, a $\varnothing 3 \times 1$ mm disk is cut out of the slice.

(2) Grinding

The ceramic disk is glued to the center core of a Gatan disk grinder for mechanical thinning. One side of the disk is ground and polished to a smoothness of $\frac{1}{4}$ μm . Then the glue is dissolved, the disk is turned upside down and again glued to the polishing mount to grind the other side. The grinding is continued until 100 μm thickness is reached.

(3) Dimpling

With the thin disk the center core is taken out of the Gatan disk grinder and put in a dimpling apparatus (Gatan Model 656). The aim of this process is to thin the center of the disk while minimizing damage to the surface of the sample. The last step of the dimpling is also to get a smoothness of $\frac{1}{4}$ μm on the surface. Finally the thickness of the center of the disk is about 20 to 30 μm . The disk is then carefully dismantled by dissolving the glue. A copper ring with 3 mm diameter is glued to the disk to support it. Now it is ready for ion-beam milling.

(4) Ion-beam milling

Ion-beam milling involves bombarding the specimen with energetic ions and sputtering material from the specimen until it is thin enough to be studied in the TEM. The equipment used in the present work is called PIPS (precision ion polishing system, Gatan Model 691). The accelerating voltage is 4 to 6 keV, and the Ar ion beam is aligned at an angle of 7 to 10° to the surface of the specimen. Since SiC-based ceramics are hard, several hours of continuous bombarding are normally required. When a hole in the center of the disk is visible by the optical microscopy, the accelerating voltage is reduced to 2 keV and kept there for 20 minutes to remove the amorphous layer on the surface caused by the previous bombarding. Finally the edge of the hole can be electron-transparent, with a thickness of 10 to 100 nm, thin enough for TEM investigation.

Table 3.1 The ionization energy of the elements measured in this work

Element with their EELS edge	Ionization energy, eV
Si L _{2,3}	99
C K	284
B K	401
O K	532

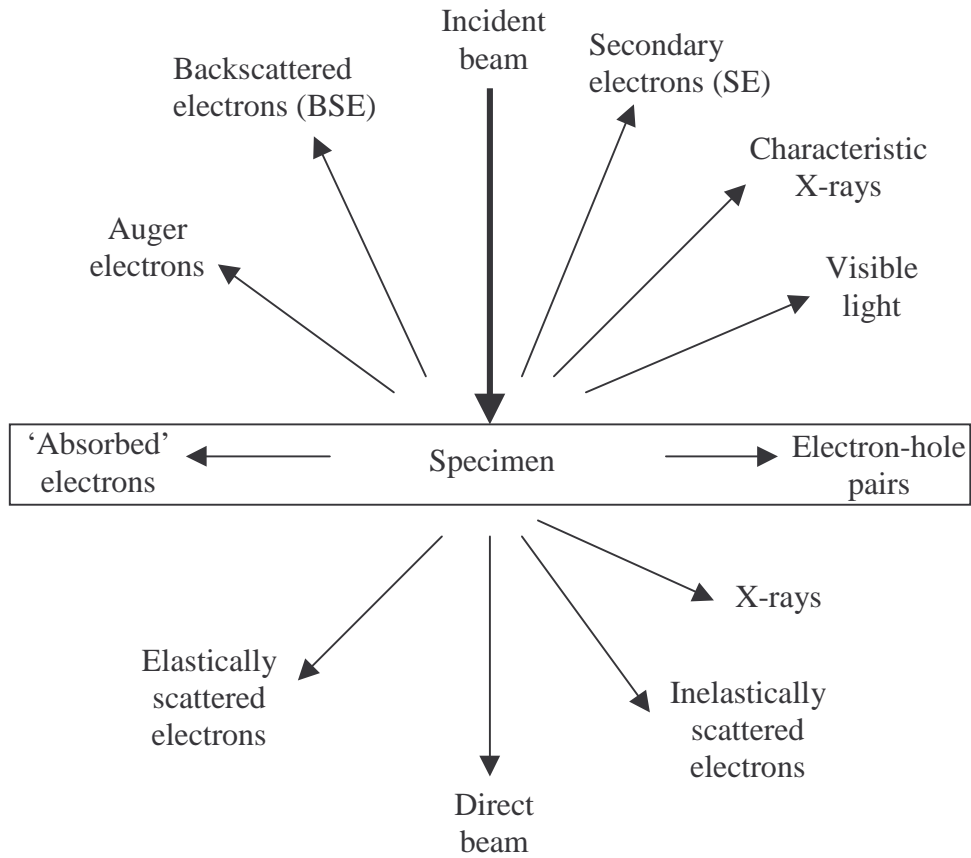


Fig. 3.1 Signals generated when a high-energy beam of electrons interacts with a specimen. Most of these signals can be detected in different types of electron microscopes. The directions shown for each signal do not always represent the physical direction of the signal but indicate, in a relative manner, where the signal is strongest or where it is detected.

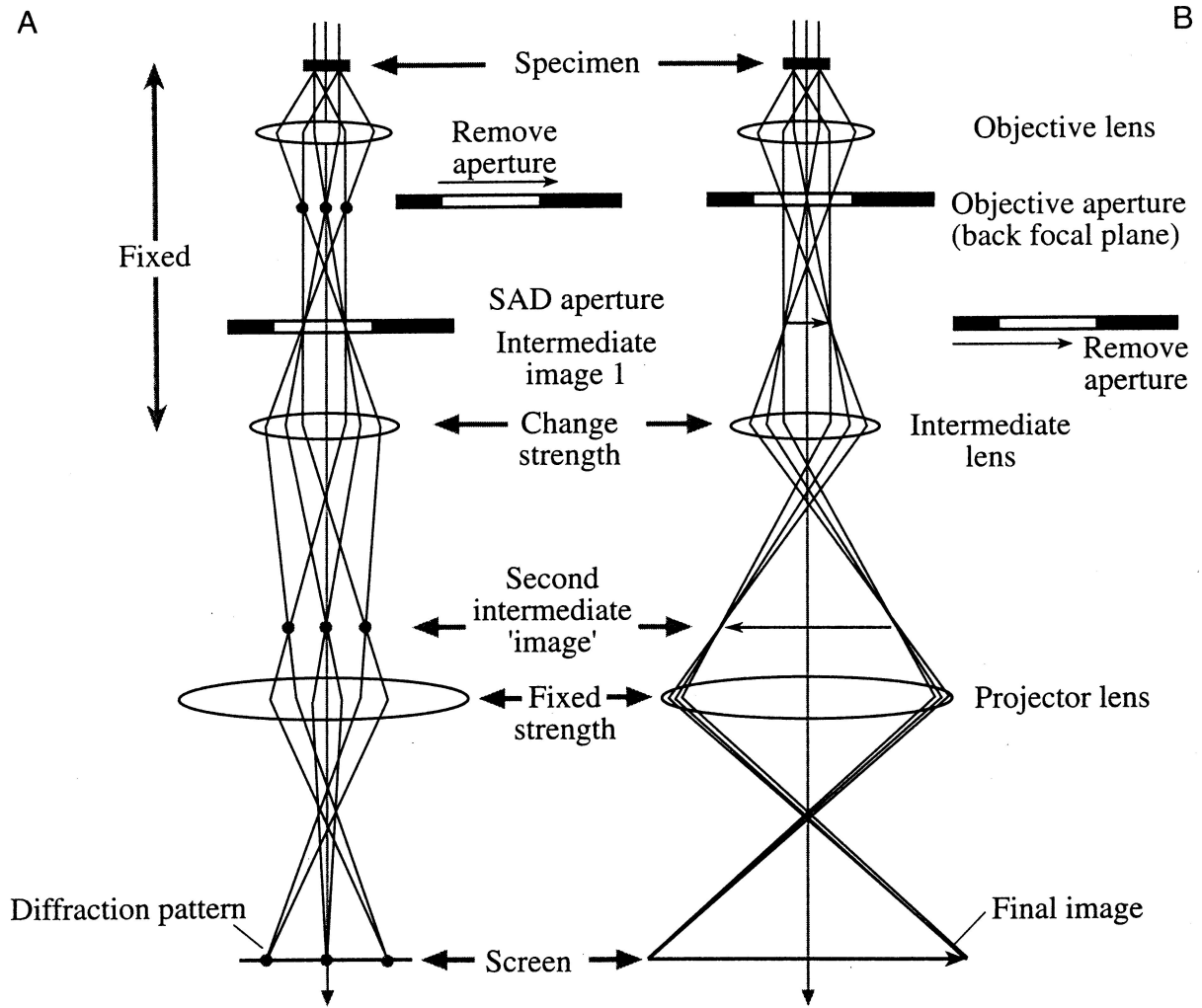


Fig. 3.2 The two basic modes of operation of the TEM system involve (A) projecting the diffraction pattern on the viewing screen and (B) projecting the image onto the screen.

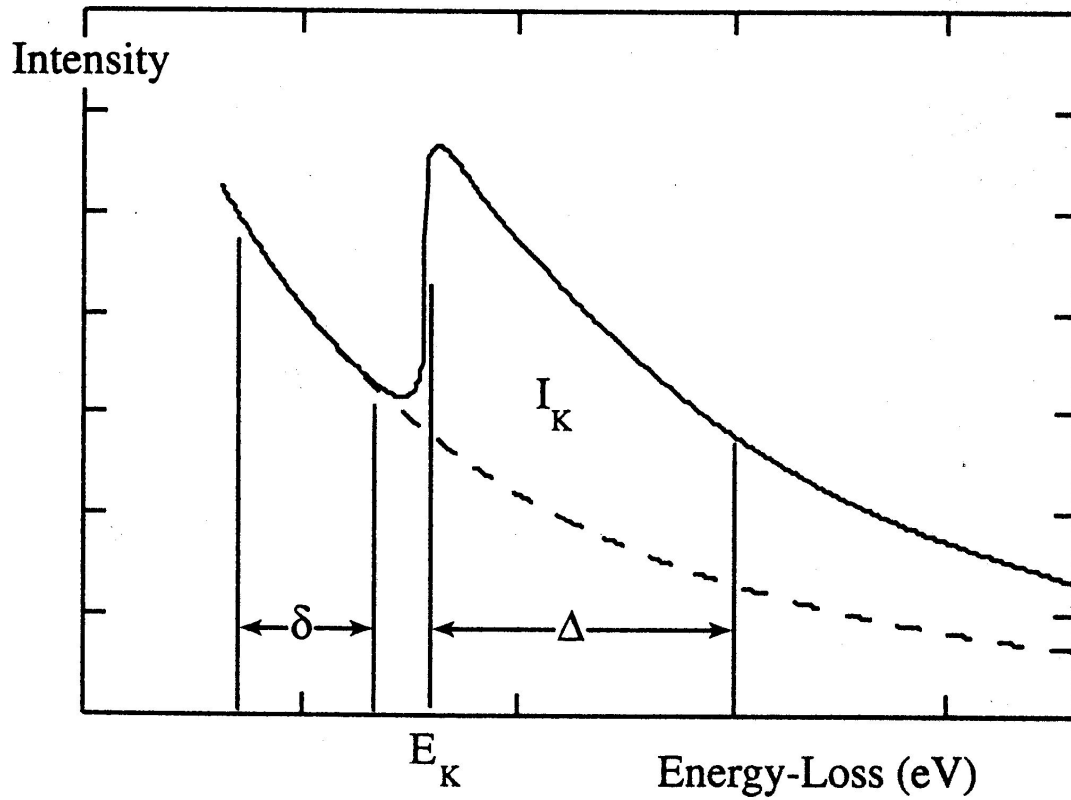


Fig. 3.3 Curve fitting method used to remove the background in EELS. A window δ in the background before the edge onset is selected to draw a fitting curve. The curve is extrapolated under the EELS edge. The edge intensity I_K over a post-edge window Δ is obtained by subtracting the extrapolated background.

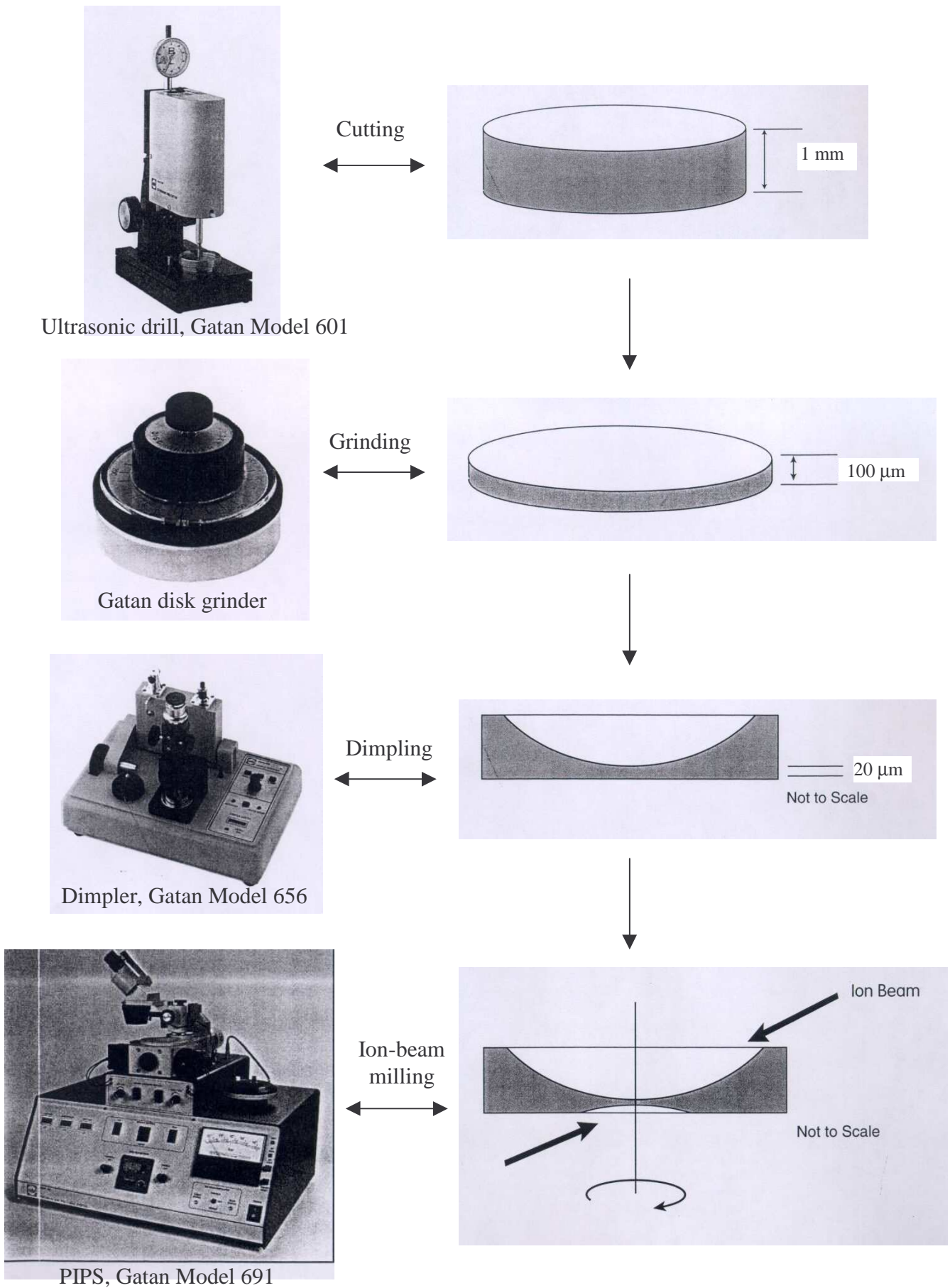
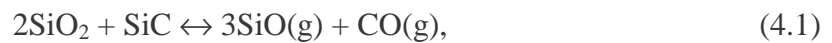


Fig. 3.4 The preparation procedure of bulk specimen for TEM.

4 THE MODEL SYSTEM SiC-SiO₂

4.1 Introduction

In this chapter, the model system consisting of liquid-phase sintered SiC with SiO₂ as the only sintering additive is discussed. The motivation for studying this model system comes from the theoretical work by Clarke [CLA87] who argued that SiO₂ films are not stable at SiC-SiC grain boundaries. According to his model the equilibrium film thickness calculated on the basis of local force balance is zero. The apparent contradiction between this theoretical calculation and many experimental observations has been reviewed in Section 2.4.2. It is therefore interesting to investigate the validity of Clarke's model with respect to the SiC-based materials. Since the behavior of the grain-boundary films is strongly affected by their composition, using solely SiO₂ as sintering additive is supposed to simplify the interpretation of the experimental observations and related model calculations. A major experimental difficulty for investigation comes from the fact that the system SiC-SiO₂ is thermodynamically unstable under standard sintering conditions. According to the reaction



it has to be stabilized by controlling the CO partial pressure in the sintering atmosphere.

4.2 Experimental procedure

α -SiC (UF15, H.C. Starck) was used as raw material. The amount of silica added as a sintering additive was 0 wt %, 5 wt %, 10 wt %, or 20 wt %. The powder mixtures were prepared by attrition milling in isopropanol with Si₃N₄ milling media for 4h, using a polyethylene container and stirrer. The slurry was separated from the milling media via a sieve chain and subsequently dried in a vacuum evaporator. Completely dried mixtures were obtained after 48 h at 65 °C in a drying chamber. Finally the processed powder was sieved to obtain granules with a maximum diameter of 160 μm , and cold isostatically pressed at a pressure of 600 MPa into cylinders of 15 mm \varnothing \times 12 mm height. Sintering was performed in a gas-pressure furnace (KCE GmbH, Rödental) with a graphite heating element. The main sintering conditions are shown in Table 4.1. To restrict the reaction between SiC and SiO₂, sintering atmospheres containing CO were used. CO gas was transferred into the furnace when the temperature had reached 800°C. The CO pressure was released after the end of the

isothermal holding period (0.5 h). The densities of the sintered samples were measured by the Archimedes principle in distilled water at room temperature. The theoretical densities of the samples were calculated using the rule of mixtures, taking the densities of SiC as 3.22 g/cm^3 and SiO₂ as 2.20 g/cm^3 . X-ray diffraction patterns (Siemens D5000, Cu K_α radiation) were used to identify the crystalline phases. After sintering, the hexagonal crystal structure of α-SiC was retained, and no crystalline SiO₂ could be detected by XRD. Specimens for scanning electron microscopy (Zeiss DSM982 Gemini, equipped with a thermal Schottky field emission cathode) were polished to 1 μm using routine ceramographic techniques. The microstructure of the sintered samples was observed using SEM at magnifications ranging from 1000× to 50000×.

Samples sintered to the highest possible density were selected for TEM study. Thin foils for TEM were prepared by the standard procedures of grinding, dimpling, and argon ion-beam thinning. TEM and HREM observations were performed with an electron microscope (Model JEM-4000EX, JEOL, Japan) which was operated at 400 kV and has a point resolution of 0.17 nm.

Spatially-resolved EELS analysis was performed with a dedicated scanning transmission electron microscope (STEM, model HB501, Vacuum Generators, U.K.) with a Gatan 666 Parallel EELS spectrometer. The STEM is equipped with a cold field emission electron gun and has an electron probe size smaller than 1 nm and an energy resolution better than 0.7 eV. Quantitative analysis was performed on background-subtracted EELS data by using a special software (EL/P, Gatan Inc.) and with an uncertainty of about 10 %.

4.3 Densification

4.3.1 Effect of sintering temperature

Fig. 4.1 shows the evolution of the density of SiC-20 wt % SiO₂ specimens with increasing sintering temperatures. A density as high as 94.2% of the theoretical value was achieved at 1860°C, while both higher and lower temperatures caused a sharp decrease of the density. Below 1860°C poor densification is considered to be the consequence of an insufficient amount of liquid phase. Although liquid-phase sintering may not be the only mass-transfer process, the dominant mechanism which determines the final density must clearly involve the liquid phase [GER85]. The lowest melting temperature in the SiC-SiO₂ system is 1723°C, which explains why the amount of liquid phase is not sufficient when sintering below this temperature. Shortly above this temperature (1790°C), the sintering time of 30 minutes may

be not long enough to produce sufficient amount of liquid phase and a low enough viscosity to complete rearrangement of SiC particles. This consideration is supported by the shrinkage-temperature curve (Fig. 4.2) which shows that shrinkage increases sharply above 1790°C, indicating that sufficient amounts of liquid phase forms only above this temperature. Through SEM images (Fig. 4.3) the change of microstructure caused by the presence of the liquid phase is monitored. The microstructure of the sample sintered at 1790°C (Fig. 4.3b) does not show much difference to that of the sample sintered at 1720°C (Fig. 4.3a); it merely seems to contain some more clusters of SiC grains. In contrast, the microstructure of the sample sintered at 1860°C (Fig.4.3c) looks strikingly different: the sample is much more dense, the grain size is much larger and the liquid phase can be easily identified between the SiC particles.

The decrease of density above 1860°C is associated with an increasing weight loss (Fig. 4.2), which is due to reactions between SiC and SiO₂. The most favoured reaction is [NAD95] equation 4.1. At low temperatures (1400 K - 1600 K) [JAC92], this reaction was found to be very sluggish in reaching the steady state, but at elevated temperatures, it became violent and the volatilization of SiO and CO caused large weight losses and low densities. The point where the reaction rate accelerates can be obtained by thermodynamical calculation. Fig. 4.4 shows the free-energy change of reaction (4.1) at different total pressures as a function of temperature. In the temperature range of 1900°C to 1970°C, ΔG changes from positive to negative for pressures between 0.1 and 0.2 MPa, i.e. reacting into SiO and CO becomes thermodynamically favored. This range of temperatures corresponds to the sharp increase of weight loss near 1950°C in Fig. 3.2.

The scanning electron micrograph of SiC with 20 % SiO₂ sintered at 1950°C is shown in Fig. 4.5. Some remnants of solidified liquid phase can be found between the SiC particles (see arrow). More careful observations show that there are many open gas bubbles on the surface of these solidified liquid phase patches. These gases are believed to be produced from the reaction of SiC and SiO₂ according to the above thermochemical analysis.

Although it is reasonable to assume that at a temperature of 1860°C, the reaction of SiC and SiO₂ also occurs to a certain extent, the rate of shrinkage at this temperature obviously exceeds the rate of the gas evolution due to reaction (4.1), and densification prevails.

4.3.2 Effect of the SiO₂ content

The effect of the content of SiO₂ additive on the final density is shown in Fig. 4.6. At the sintering temperature of 1960°C, the reaction of SiC and SiO₂ is the main process. Accordingly an increasing SiO₂ content promotes the reaction, and therefore decreases the

density of the products. At the reduced temperature of 1860°C, shrinkage caused by the presence of the liquid becomes dominant, and an increase of the SiO₂ content is beneficial to sintering.

4.4 Grain-boundary films

4.4.1 HRTEM observations and EELS compositional analyses

The SiC with 20 wt% SiO₂ sintered at 1860°C showing the highest density (94.2% of the theoretical density) was selected for electron microscopic studies. A large number of grain boundaries were observed by HRTEM, with the result that thin amorphous films can always be found at grain boundaries. The thickness of the films ranges from 0.7 nm to 6 nm, with a mean value of 1.5 nm. The HRTEM image of a typical grain-boundary film of 1.5 nm thickness is shown in Fig. 4.7. These observations are apparently different from forecasting based on Clarke's model. Detailed EELS compositional analysis was therefore necessary to be performed on grain-boundary films to understand the deviation.

An EELS spectrum from an amorphous grain-boundary film is shown in Fig. 4.8. Not only Si and O from the silica additive, but also C and a small amount of N were identified in the EELS spectrum. It is difficult to distinguish between the carbon content of the grain-boundary film and carbon contamination from the residual atmosphere inside the microscope. But when an ELNES (electron energy-loss near-edge structure) analysis equivalent to that described in Section 6.6.3 was performed, the carbon content of the grain-boundary films could be clearly attributed to the dissolution of SiC in liquid SiO₂. Since no nitride additives were used, the segregated N apparently comes from the sintering atmosphere. Upon dissolution in SiO₂ glass, C and N may substitute for O in the network of SiO₄-tetrahedra and form glassy oxycarbide [ZHA90] and oxynitride [GU96, PEZ97] respectively, both of which exhibit an increased viscosity. The significance of the formation of an oxycarbide or oxynitride melt with respect to the stability of grain-boundary films will be discussed in next section based on the model calculations.

4.4.2 Calculations based on Clarke's model

According to Clarke's model [CLA87], the total interaction energy across a liquid intergranular film due to both van der Waals attraction and steric repulsion is given by

$$E(h) = \frac{-H_{\alpha\beta\alpha}}{12\pi h^2} + \frac{2\alpha\eta_0^2\xi}{\tanh\left[\frac{h}{2\xi}\right]} \quad (4.2)$$

where $H_{\alpha\beta\alpha}$ is the Hamaker constant for grains of a material ‘ α ’ separated by a film of material ‘ β ’, h is the film thickness, $\alpha\eta_0^2$ is a constant called ‘ordering force’ which determines the strength of the repulsion, and ξ is the structural correlation length which is assumed to be of molecular dimensions. For the Si_3N_4 - SiO_2 system, where the Hamaker constant is 76×10^{-21} J [CLA87], $\alpha\eta_0^2 = 100$ MPa, and $\xi = 2.5$ Å (approximately the size of a SiO_4 tetrahedron), the interaction energy $E(h)$ can be plotted as a function of the film thickness h (cf. Fig. 4.9a for the system Si_3N_4 - SiO_2). It is evident that for decreasing film thickness there may be two local energy minima, namely the ‘secondary minimum’ at the so-called ‘equilibrium film thickness’ (for Si_3N_4 - SiO_2 , 1.8 nm), and the ‘primary minimum’ at vanishing film thickness (i.e. the “clean” crystal-crystal grain boundary). In sintering experiments, the intergranular film thickness decreases under the influence of the attractive Van der Waals force, starting from a large initial separation of the grains. Unless the Van der Waals interaction is very large, the thinning of the intergranular film will stop as force equilibrium with the steric repulsive force is reached, thus establishing an equilibrium film thickness. Since the energy barrier between the primary and secondary minimum is high, the resulting intergranular amorphous films are thermodynamically meta-stable. The same situation exists in Si_3N_4 and most other liquid-phase sintered ceramics, their Hamaker constant being comparable or smaller than in the case of Si_3N_4 . The only exception to this rule is the SiC - SiO_2 system, where the Hamaker constant is exceptionally large, reaching 233×10^{-21} J [CLA87]. The energy-thickness diagram of this system is plotted in Fig. 4.9b ($\alpha\eta_0^2 = 100$ MPa and $\xi = 2.5$ Å). Here, no energy barrier exists and the equilibrium thickness of the amorphous film is zero.

However, in the actual sintered SiC - SiO_2 ceramic, the intergranular phase is not pure silica, but silicon oxycarbide and/or oxynitride, as indicated by the above EELS/ELNES analyses. The effect of C and/or N is not only to increase the size of the Si based tetrahedra (to approximately 3.1 Å for SiC_4 and 2.8 Å for SiN_4) but also to bridge more tetrahedra (4 in the case of C and 3 in the case of N), instead of only two tetrahedra bridged by O, as shown in the schematic illustration (Fig. 4.10), and thus to increase the size of the structural correlation length ξ . The intergranular film thickness has been demonstrated to be relatively insensitive to the magnitude of the ordering force $\alpha\eta_0^2$, but very sensitive to the correlation length [ACK97]. A small increase of the correlation length will greatly enhance steric repulsion and

can thus cause a dramatic change in the energy-thickness diagram. Fig. 4.11a and Fig. 4.11b show the calculated results for the SiC-SiO₂ system with $\xi = 3.0 \text{ \AA}$ and $\xi = 4.0 \text{ \AA}$, respectively. With increasing correlation length, a secondary energy minimum appears, and the equilibrium thickness increases from 1.3 nm for $\xi = 3.0 \text{ \AA}$ to 2.4 nm for 4.0 \AA . These revised calculations based on Clarke's model are then consistent with the experimental observation, indicating that due to the inevitable presence of carbon in the liquid phase, the grain-boundary films are a characteristic feature of all liquid-phase sintered materials based on SiC, even in the special case of the pure SiC-SiO₂ system. The same is true if N is introduced into the liquid phase.

4.5 Si₂N₂O crystallization in triple junctions

Elongated, well-faceted, nanometer-sized crystals were frequently found in the triple junctions of SiC-SiO₂ samples sintered in atmospheres containing N₂. Fig. 4.12 is a low magnification TEM image where the heterogeneous distribution of these nanometer-sized crystals (about 30 to 50 nm in length) in the triple junctions is visible. Fig. 4.13 shows a TEM image of a relatively large crystal which has an elongated and well-faceted shape. The HRTEM image (Fig. 4.14) illustrates that although all of these secondary crystals are actually located close to SiC grains, there is always an amorphous film between the secondary crystals and the SiC grains, suggesting that the force balance according to Clarke's model also exists in such heterogeneous grain boundaries, inhibiting direct contacts. The volume fraction of the secondary crystals in the material is less than 1%, preventing their identification by XRD. EELS was thus performed utilizing STEM and the results are shown in Fig. 4.15. Energy loss peaks of Si, N, and O clearly appear, while no C is detectable in the EELS spectrum of the elongated crystal (Fig. 4.15b) which was identified by quantitative analysis to be Si₂N₂O. Since in the same material, however, sintered in Ar atmosphere, there is no indication for this phase [PEZ98], the significant effect of the N containing sintering atmosphere on the intergranular phase is again emphasized.

A detailed study on the grain morphology of the Si₂N₂O crystals shows that grain growth always starts in the close vicinity of the surface of SiC particles (cf. Fig. 4.12 and Fig. 4.14). This is understandable when the distribution of N in the triple junctions is considered, as it is revealed by EELS analyses: the inside of large glass pockets contains little or no N (Fig. 4.15d), while N is enriched near the surface of the SiC grains (Fig. 4.15c), indicating that incorporated N tends to preferentially segregate at the surface of SiC grains. During cooling, the N-rich surface of SiC particles becomes a suitable site for the heterogeneous nucleation of

crystals of $\text{Si}_2\text{N}_2\text{O}$ being the only stable ternary crystalline phase in the Si-N-O system [MCH94]. Similar phenomena were also found in the calcium-doped $\text{Si}_3\text{N}_4\text{-SiO}_2$ system [MAY98] and in the barium-doped SiC-SiO₂ system [PEZ00] where the dopant elements, Ca or Ba, prefer to segregate at the surface of matrix grains and at the grain boundaries, rather than being distributed in large SiO₂ glass pockets. By segregation of the impurity elements to SiC surfaces, the high interfacial energy (“bad” wetting behaviour of SiO₂ towards SiC) can be lowered significantly.

Careful design of additive composition and sintering process may allow to adjust the N segregation in order to increase the content of the elongated $\text{Si}_2\text{N}_2\text{O}$ crystals and improve their homogeneous distribution in the intergranular phase, which could be beneficial for improving the mechanical properties of SiC materials.

4.6 Crack deflection

Liquid-phase sintered microstructures can provide several toughening mechanisms, one of them being crack deflection [FAB83]. This can either mean that the cracks follow the intergranular phase and are guided around the grains (intergranular fracture mode). Or, at higher intergranular phase content, it can mean that the cracks are deflected when they pass from one phase to another phase (obstructed transgranular fracture mode). This deflection effect can be seen in the TEM image of an as-sintered SiC-SiO₂ sample (Fig. 4.16), where a crack starting from the edge of the thinned section of the TEM specimen is arrested in a large glass pocket. Due to the difference in the elastic modulus between SiC and SiO₂, the crack is deflected under a characteristic angle every time it passes a crystalline-amorphous phase boundary, which lengthens the crack path, dissipating more energy and hindering further crack extension.

Table 4.1 Sintering conditions for the SiC-SiO₂ system

Additions of SiO ₂ (wt%)	Sintering Temperature (°C)	Sintering Atmosphere and Pressure (MPa)
20	1720	1.5 MPa CO
20	1790	1.5 MPa CO
0, 5, 10, 20	1860	0.1 MPa CO & 0.4 MPa N ₂
0, 5, 10, 20	1950	0.1 MPa CO & 0.4 MPa N ₂

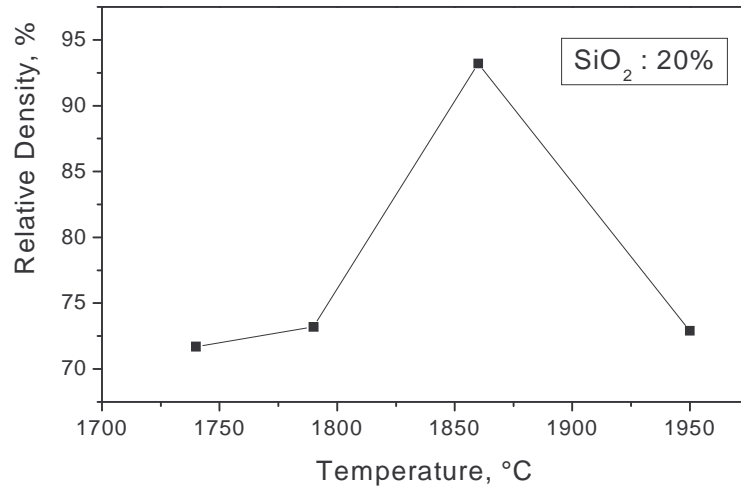


Fig. 4.1 Change of density of SiC - 20 wt% SiO₂ with the sintering temperature.

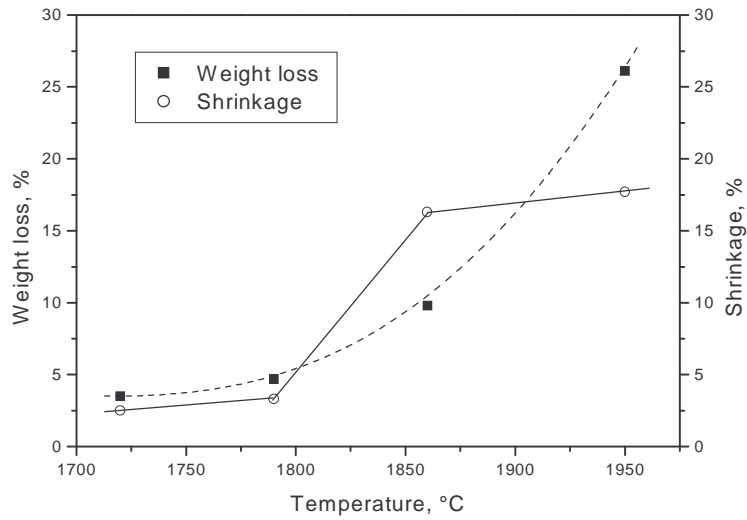
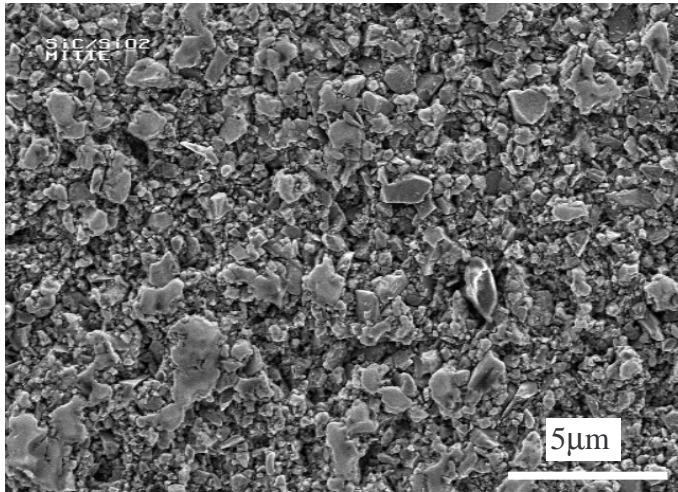
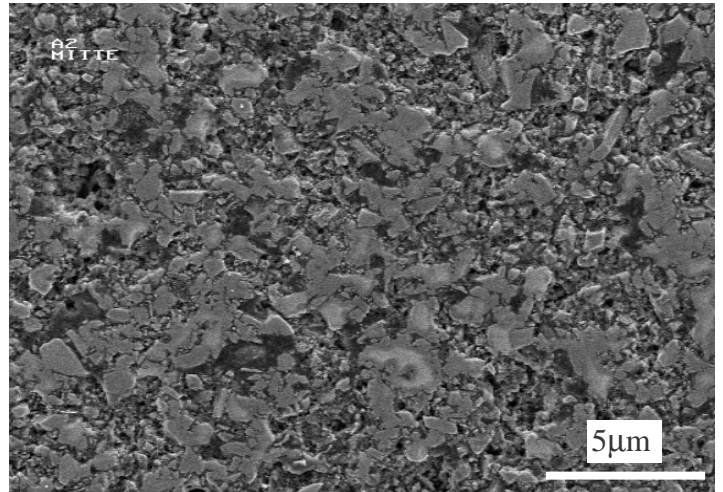


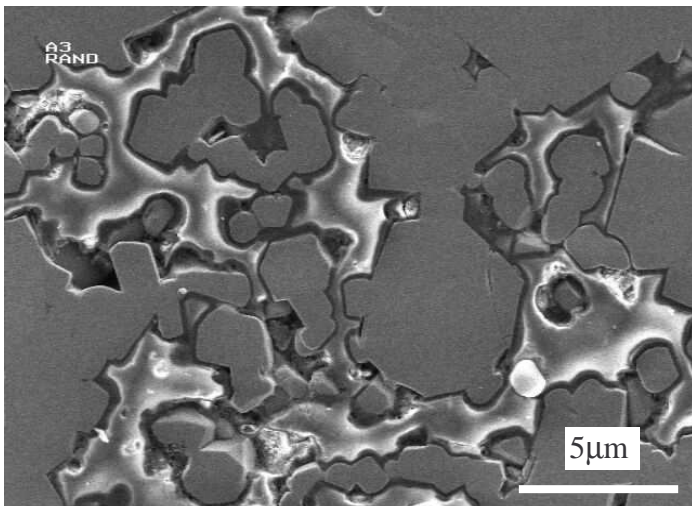
Fig. 4.2 Variation of weight loss and shrinkage of SiC - 20 wt% SiO₂ with the sintering temperature.



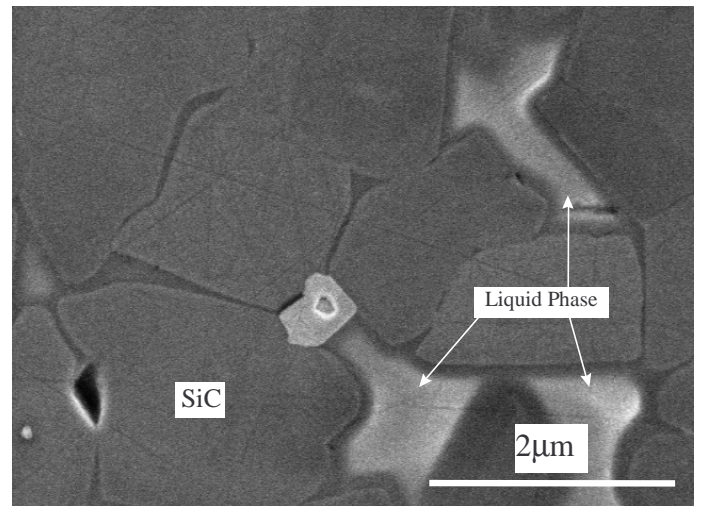
a



b



c



d

Fig. 4.3 SEM photograph of SiC - 20wt% SiO₂ sintered at 1720°C (a), 1790°C (b), and 1860°C (c and d with different magnifications), respectively.

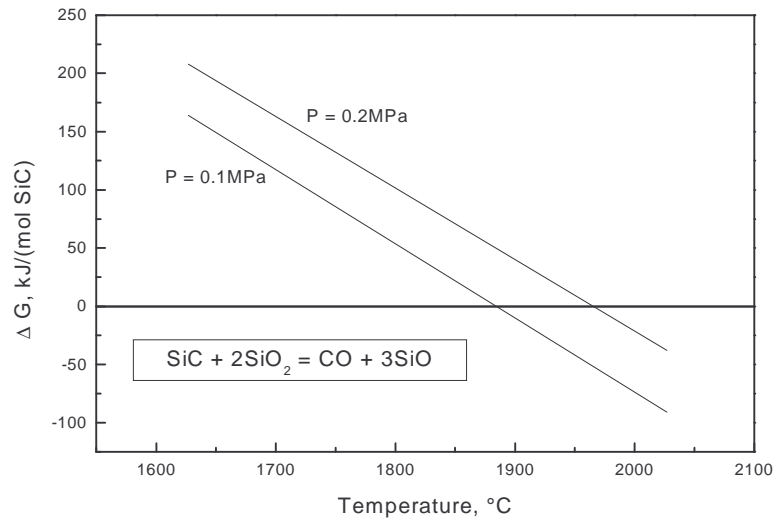


Fig. 4.4 Free-energy change of reaction ($\text{SiC} + 2\text{SiO}_2 = \text{CO} + 3\text{SiO}$) with different total sintering pressure as a function of temperature.

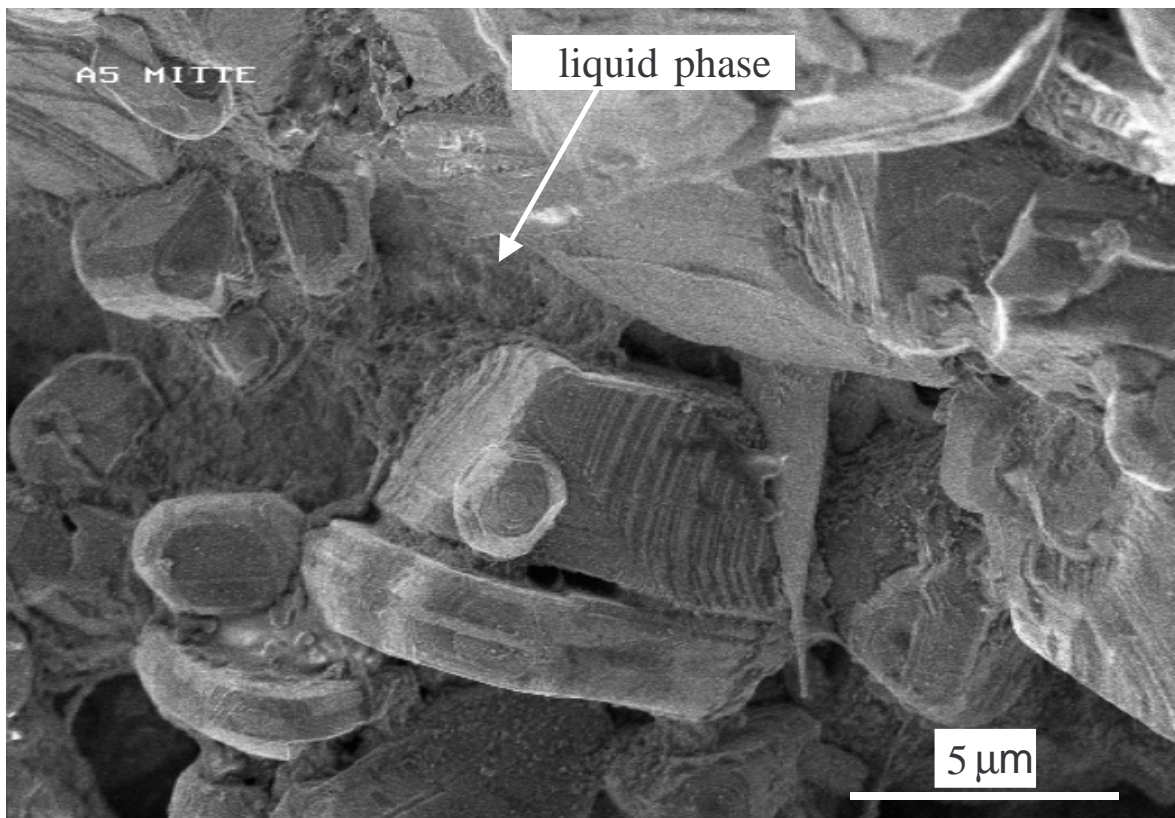


Fig. 4.5 SEM photograph of fracture surface of $\text{SiC} - 20\text{wt}\% \text{SiO}_2$ sample sintered at 1950°C . Remnants of solidified liquid phase among SiC grains are visible. Note the bubbly appearance of the liquid phase.

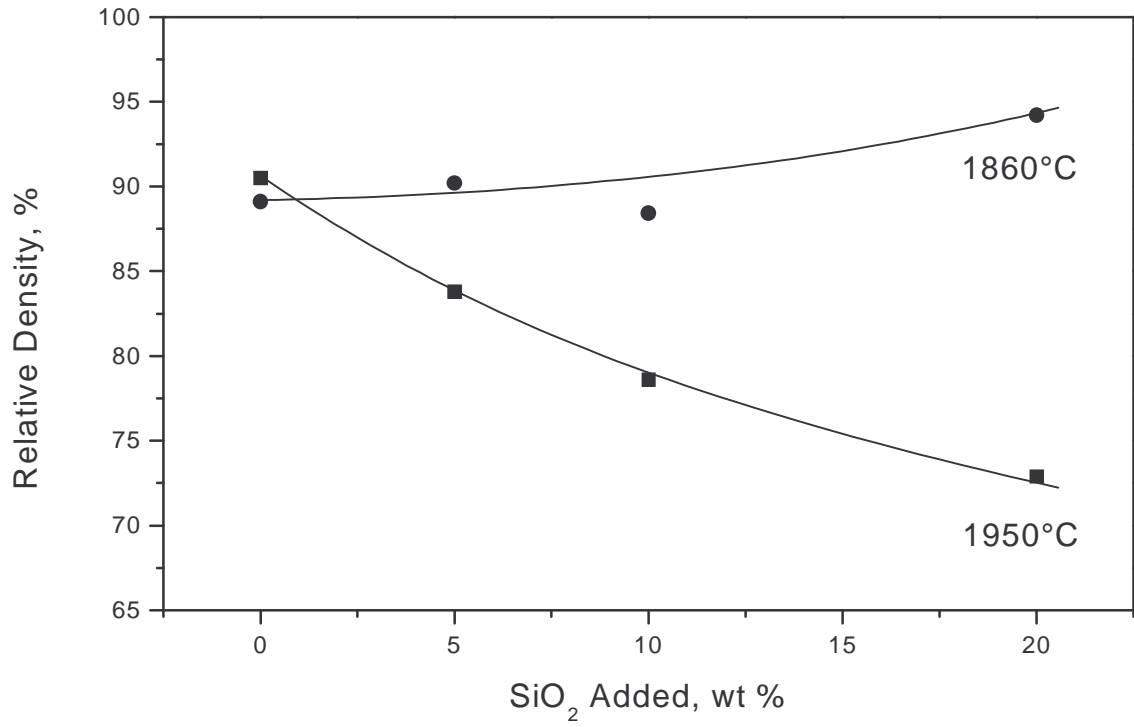


Fig. 4.6 Variation of density with the amount of initially added SiO₂ in SiC samples sintered at 1860°C and 1950°C respectively.

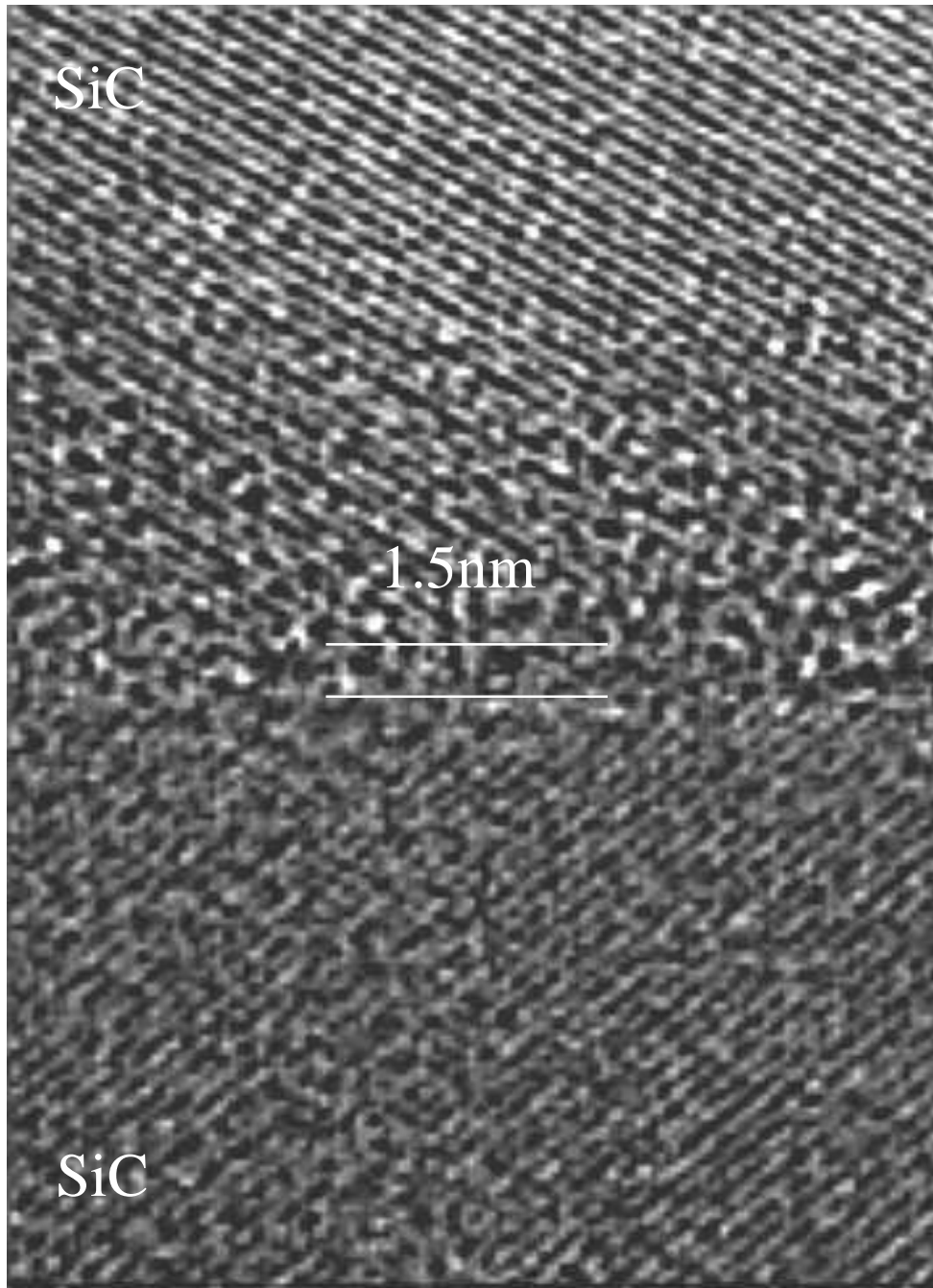


Fig. 4.7 HRTEM image of an amorphous grain-boundary film in a SiC-SiO₂ sample with a thickness of 1.5 nm.

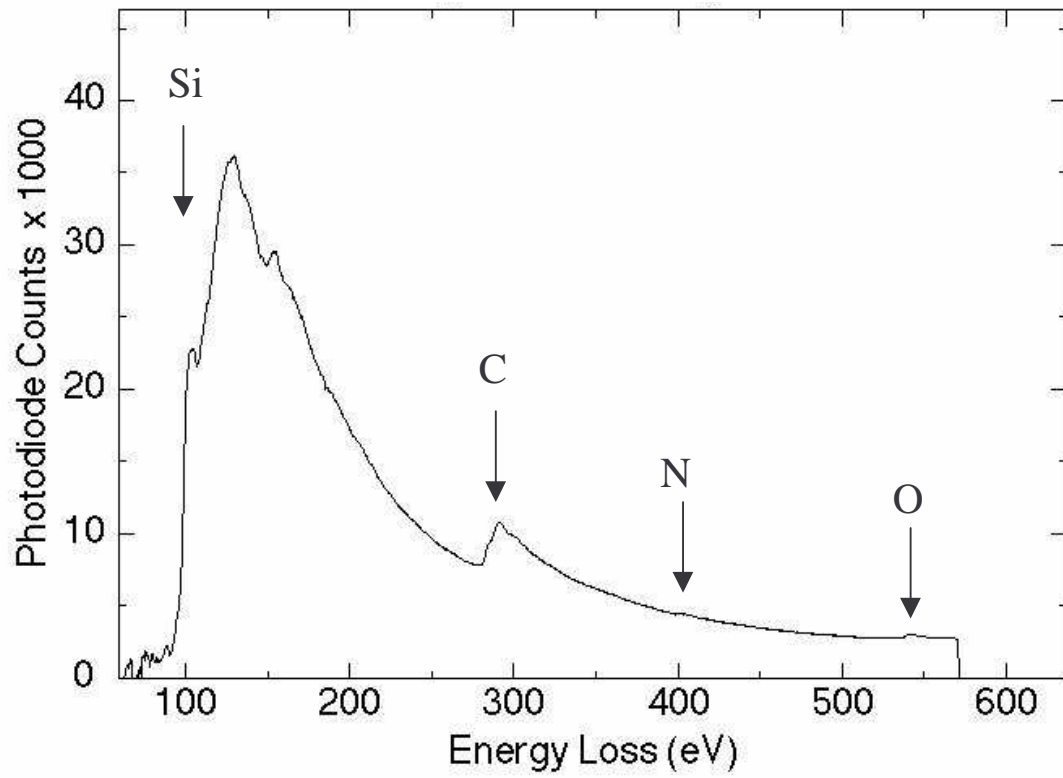


Fig. 4.8 EELS spectrum of a GB film showing the presence of the elements Si, C, N and O in the film (background subtracted).

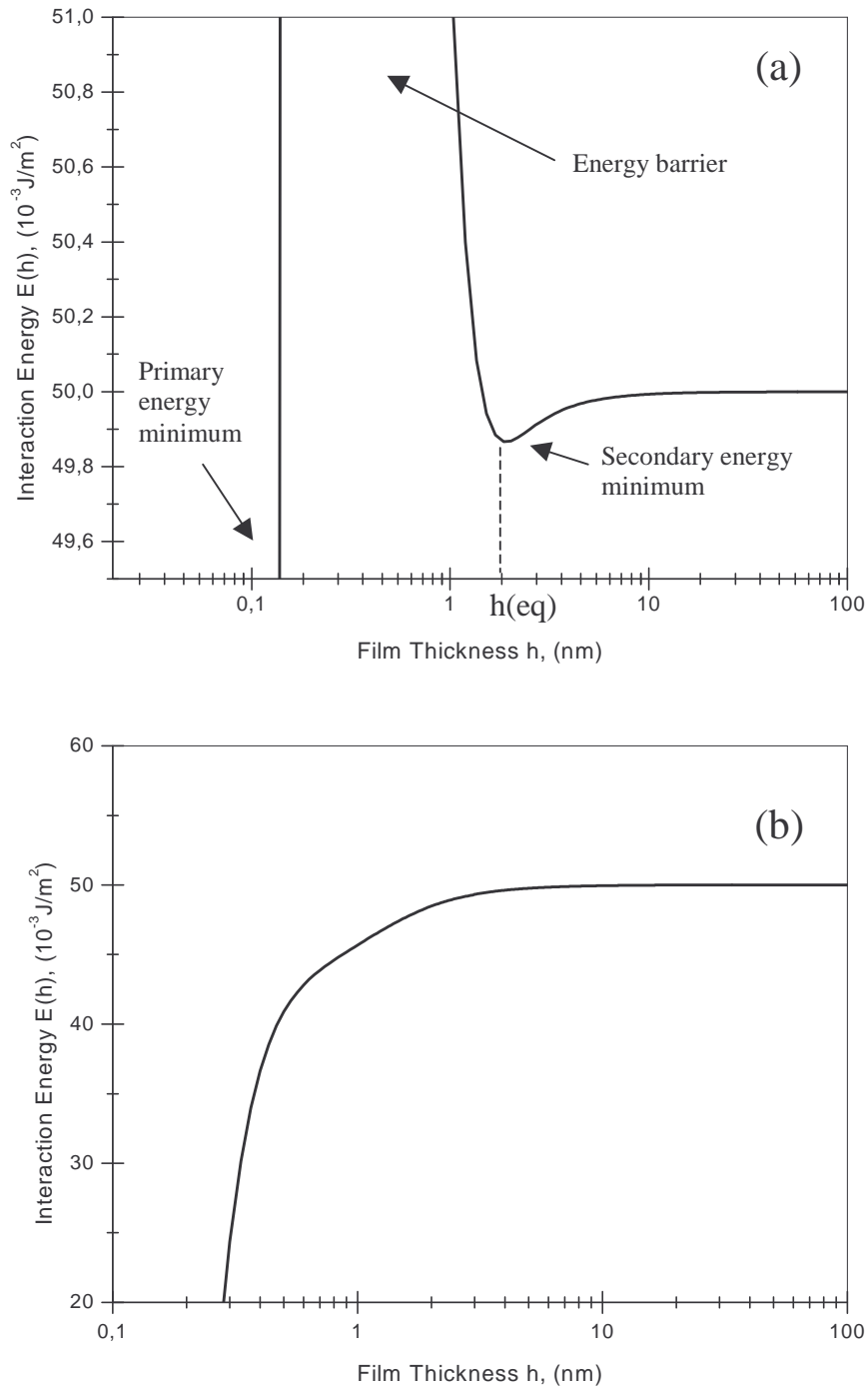


Fig. 4.9 Calculated interaction energy E as a function of the film thickness h for the configurations (a) $\text{Si}_3\text{N}_4\text{-SiO}_2\text{-Si}_3\text{N}_4$ and (b) $\text{SiC-SiO}_2\text{-SiC}$, assuming that $\alpha\eta_o^2 = 100$ MPa, $\xi = 2.5$ Å, (a) $H_{\alpha\beta\alpha} = 76 \times 10^{-21}$ J, and (b) $H_{\alpha\beta\alpha} = 233 \times 10^{-21}$ J. The resulting equilibrium thicknesses, $h(\text{eq})$, are (a) 1.8 nm and (b) 0 nm, respectively.

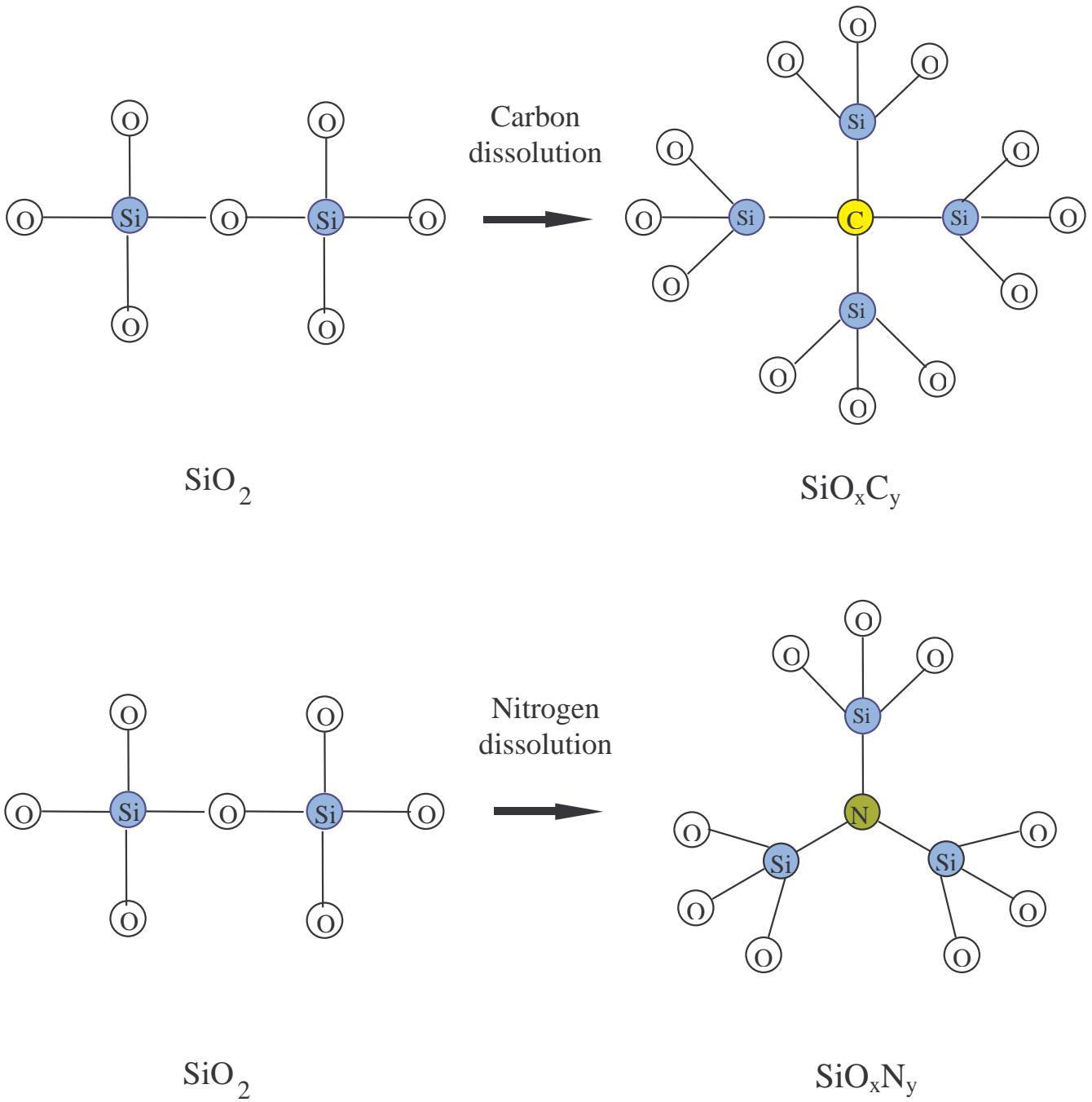


Fig. 4.10 Schematic illustration of the increasing of the correlation length by formation of silicon oxycarbide or silicon oxynitride instead of silica.

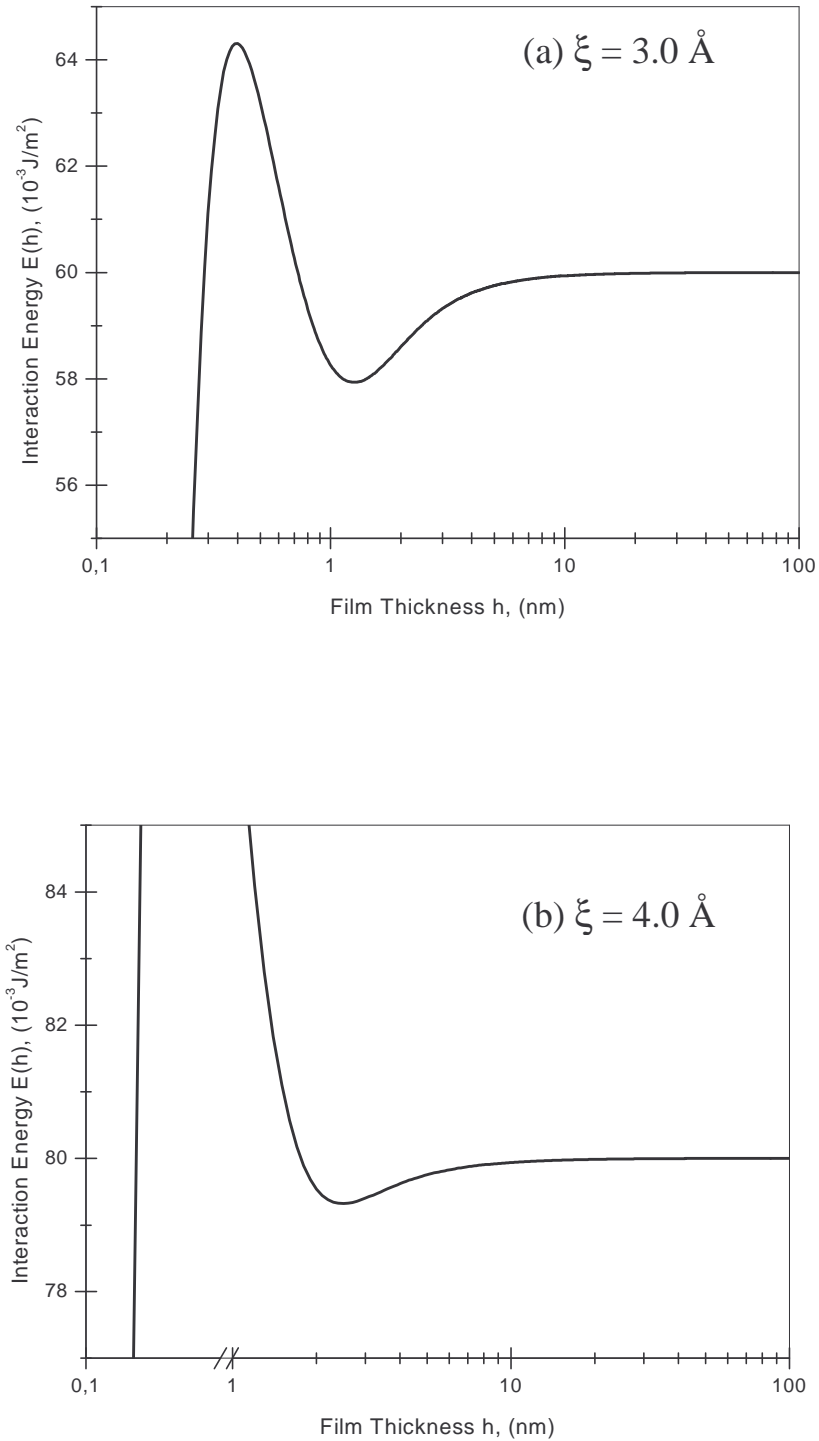


Fig. 4.11 Calculated Interaction Energy E as function of film thickness h for the SiC-SiO₂-SiC system, assuming that $H_{\alpha\beta\alpha} = 233 \times 10^{-21} \text{ J}$, $\alpha\eta_o^2 = 100 \text{ MPa}$, (a) $\xi = 3.0 \text{ \AA}$, and (b) $\xi = 4.0 \text{ \AA}$. The equilibrium thicknesses are (a) 1.3 nm and (b) 2.4 nm, respectively.

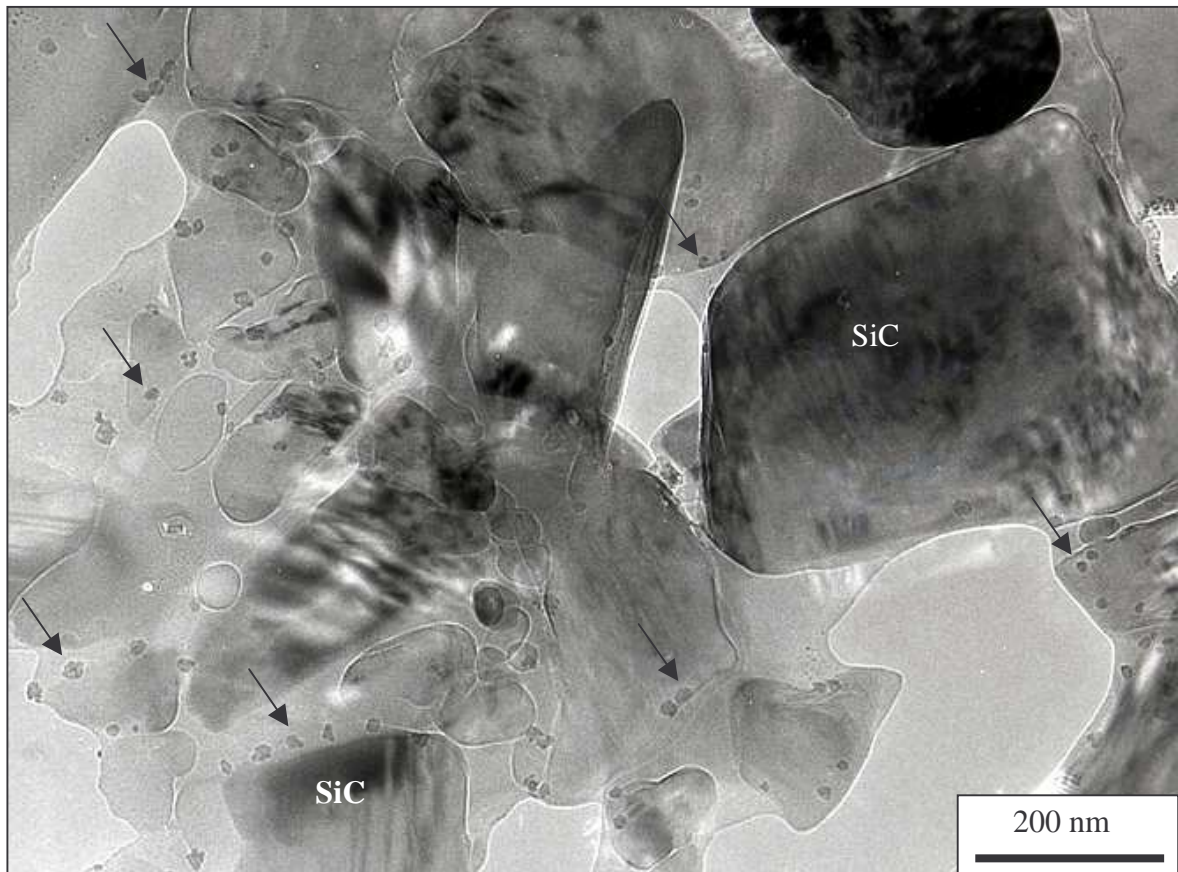


Fig. 4.12 TEM image of SiC-SiO₂ sample. Nanometer-sized secondary crystals are heterogeneously distributed in the intergranular phase, as indicated by arrows.

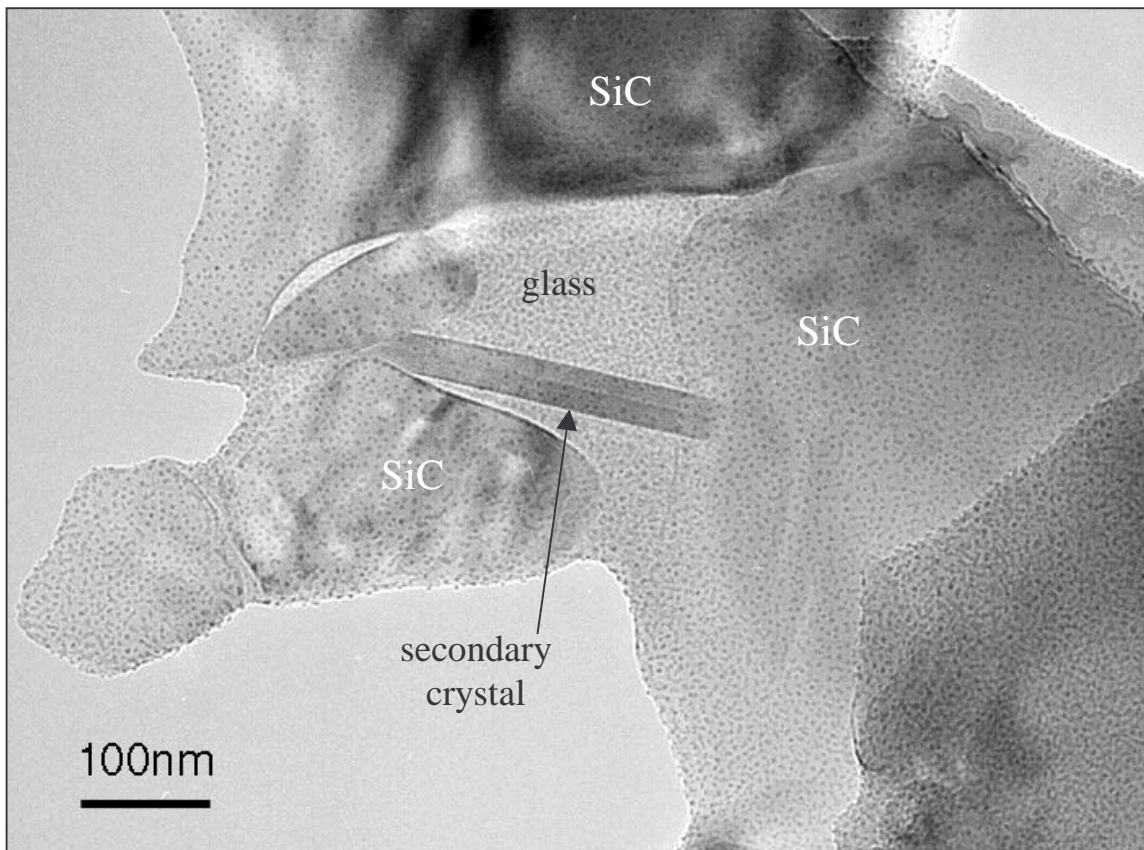


Fig. 4.13 TEM image showing one of the secondary crystals, which has a relatively large size: 260 nm in length and 30 nm in width.

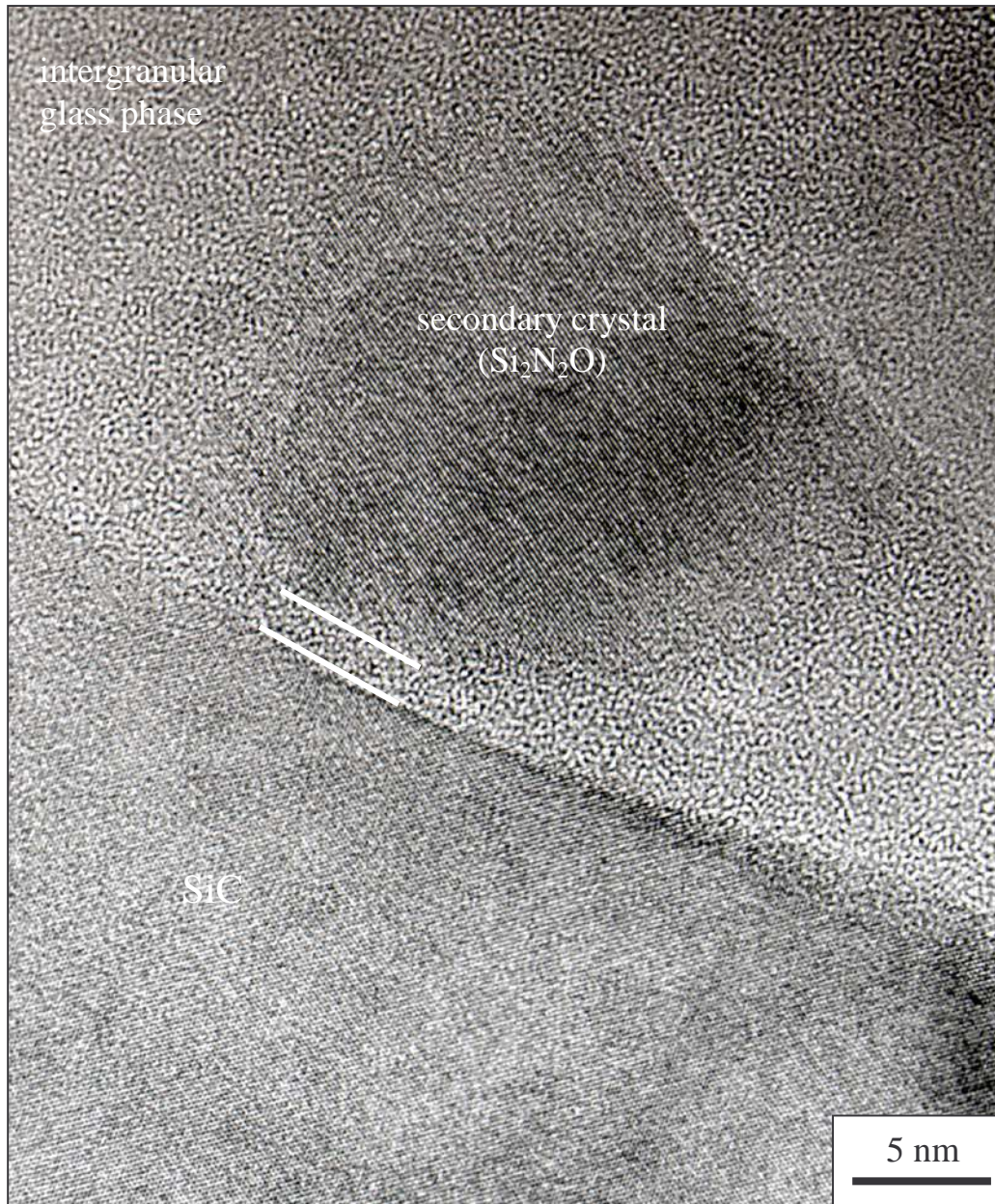


Fig. 4.14 HRTEM image showing an amorphous film between a secondary crystal ($\text{Si}_2\text{N}_2\text{O}$) and a SiC grain, as indicated by two lines.

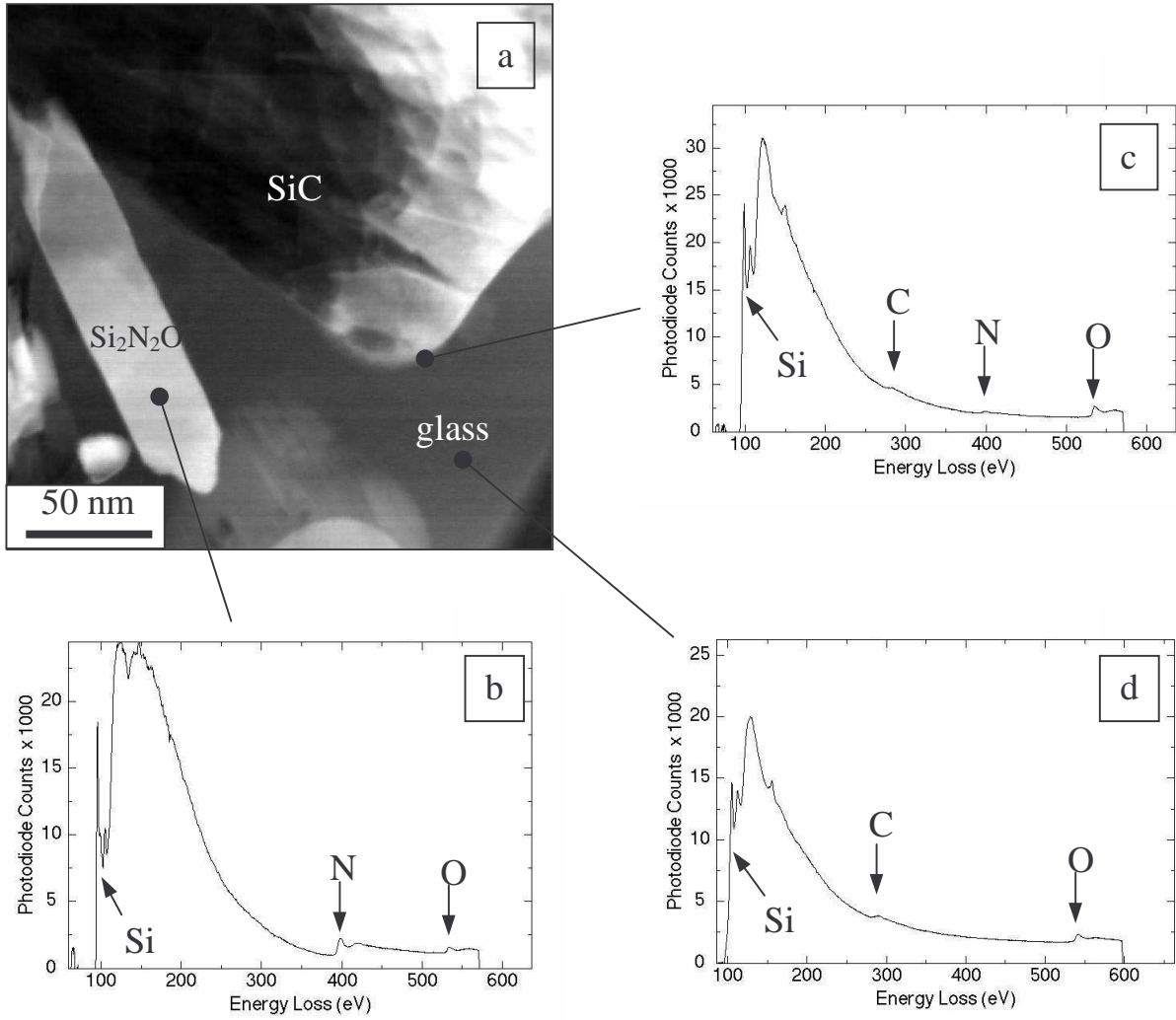


Fig. 4.15 EELS analyses of intergranular phases in SiC ceramics: STEM image (a) and EELS spectra of elongated crystal (b), surface of SiC particle (c), and glass phase (d). The spectra were processed by background subtraction.

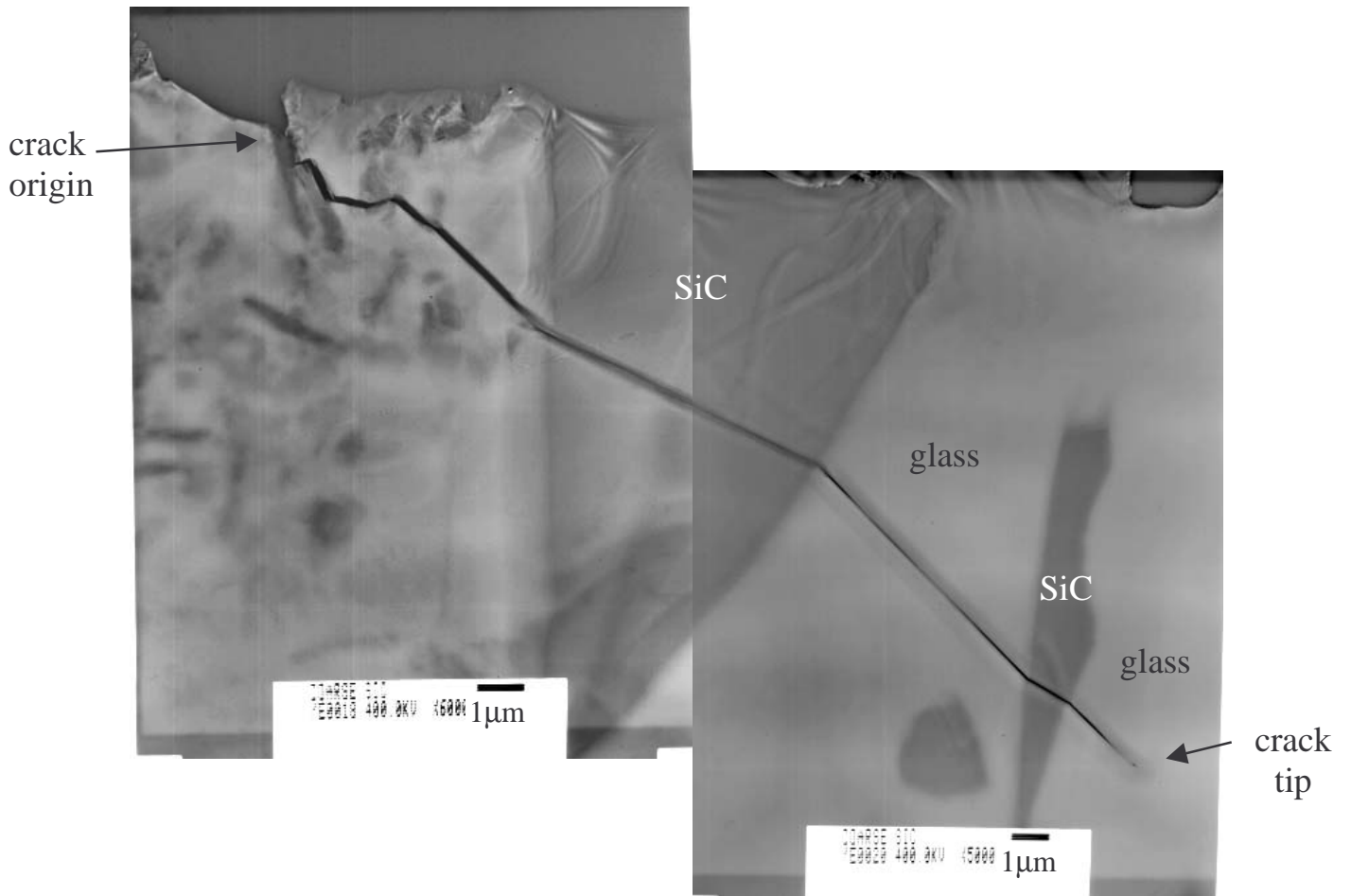


Fig. 4.16 TEM image showing crack deflection at the phase boundaries.

5 THE “COARSE SiC” MODEL SYSTEM

5.1 Introduction

Because of the very significant influence of the intergranular phases on sintering behavior and mechanical properties, quantitative identification of their chemical compositions is of great value for the design of high-performance SiC ceramics. A beneficial additive system has been proven to be Y_2O_3 -AlN [KEP98, NAD95]. However, because of the very fine microstructural features of SiC ceramics densified with the additives from this system, which are in the sub- μm range, precise compositional identification of the intergranular phases has not been achieved yet. For this chapter, a model system was studied using coarse SiC powders (32-160 μm) for liquid-phase sintering, resulting in microstructural features coarse enough for the spatial resolution offered by wavelength-dispersive X-ray spectrometry (WDS). WDS using the scanning electron microscope is an excellent method for the quantitative analysis of chemical compositions because of its high accuracy and ability to quantify light elements (including C, N and O). The intergranular regions are shown to contain large amounts of a N-rich amorphous phase which had not been described up to now.

5.2 Experimental procedure

The starting materials were a raw Acheson SiC powder (ESK Delfzijl) and fine AlN (Grade C, H. C. Starck) and Y_2O_3 (Grade C, H. C. Starck) powders. The SiC powder had an α : β ratio of 3:2 and a SiO_2 content of 2 wt%. Two sieves (32 μm and 160 μm) were used to separate the SiC powder into three fractions with particle sizes of < 32 μm , 32 μm -160 μm , and > 160 μm . The intermediate fraction, with a volume weighted mean particle size of 64 μm , as measured by laser granulometry (Alcatel, France), was selected for sintering. The particle size distribution of the selected SiC starting powder is shown in Fig. 5.1. The compositions of various powder mixtures prepared and the nomenclature used to describe the samples are specified in Table 5.1. The mixtures were prepared in a Turbula mixer for 72 hours using 5 wt% PVB (polyvinyl butyral) as a binder. The powder mixtures were cold isostatically pressed at 600 MPa into green bodies having a cylindrical shape. The green bodies were then slowly heated, at a rate of 0.16 K/min, to 500°C in air in order to burn out the binder. Finally, sintering was performed in a gas-pressure furnace (FCT, Germany) with a graphite heating element in an argon or N_2 atmosphere. The sintering conditions of various samples are summarized in Table 5.1. After sintering the samples were cooled at a rate of 20 K/min to 1500°C and then at a rate of ~50 K/min to room temperature.

The densities of sintered samples were measured using Archimedes' method. The theoretical densities of the different compositions were calculated based on the rule of mixtures, by taking the density of SiC (containing 2 wt % SiO₂) as 3.18 g/cm³, Y₂O₃ as 5.02 g/cm³ and AlN as 3.26 g/cm³. The relative densities were thus available by comparing the measured densities and the theoretical densities. The weight loss during sintering was calculated by weighing the green and sintered bodies. X-ray powder diffractometry (Siemens D5000, Cu K_α radiation) was performed to identify the crystalline phases. Microstructures were observed by using scanning electron microscopy (DSM982, Zeiss) and transmission electron microscopy (JEM 4000EX, JEOL). The content of the intergranular phase was evaluated by analyzing the SEM images using ImageC point-analysis software (Imtronic GmbH). X-ray wavelength-dispersive spectrometry (SX100, Cameca) was used to perform both quantitative electron probe microanalysis with a spatial resolution of 1 μm and elemental mapping with an image size of 576×399 pixels and total scanning time of 20 hours. At least 10 points were measured for every phase to obtain statistically meaningful results.

5.3 Overall microstructure and composition

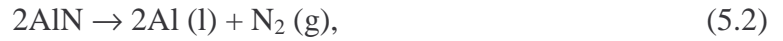
Table 5.2 gives an overview of the relative density and weight loss after liquid-phase sintering of the materials investigated. The sintering conditions, chosen to allow fine-grained SiC to be sintered to full density [KEP98, NAD95, RIX00], lead to a relative density around 67 %. Fig. 5.2 shows the SEM micrographs of the sintered coarse SiC samples. Obviously, the intergranular spaces among the coarse SiC grains were too large to be completely filled by the liquid phase that forms during sintering, thus preventing complete rearrangement of the SiC grains and leaving large pores behind. These large pores are visible in all the samples sintered in Ar and N₂, which explains the low value of the measured relative densities. Although increasing the quantity of additives or extending the sintering time should allow to increase the final density, these methods are not adopted in the present model experiment because of two reasons. First, similar sintering conditions should be chosen in order to simulate the technologically relevant systems which were proven to possess tailored properties [KEP98, NAD95, RIX00]. Second, local densification already exists at many locations in the samples as can be seen in Fig. 5.2. In regions where the liquid phase has completely filled the intergranular spaces, compositional analysis by WDS is feasible. Attempts to increase the amount of the intergranular phase are therefore unnecessary.

The relative content of the intergranular phase is found by evaluating Fig. 5.2 with a special software (ImageC point-analysis). The bright phase in Fig. 5.2 is considered as the

intergranular phase, the gray phase as SiC grains and the dark phase as holes. The content of the intergranular phase C is calculated by

$$C = \frac{\text{Number of points over bright phase}}{\text{Number of points over bright and gray phases}} \quad (5.1)$$

The result is shown in Table 5.3. It is obvious that the SiC sample sintered in Ar (C-60AlN-Ar) contains a smaller amount of intergranular phases (5.6 %) than those sintered in N₂ atmosphere (from 15.1 % to 17.6 %), despite the fact that they contain the same volume of additives in the green bodies. This is because the decomposition reaction of the additive AlN at the sintering temperature,



can be efficiently suppressed by a N₂ atmosphere [NAD95, JUN97], but not in the case of an Ar sintering atmosphere. The decomposition of AlN can even be accelerated in the present model experiment because porous microstructures supply fast channels for releasing N₂ gas and thus encourage the reaction to proceed to the right side. This reason can also serve to explain the lower relative density and higher weight loss of the sample sintered in Ar, as shown in Table 5.2. Comparing the SEM micrographs of samples sintered in N₂ (Fig. 5.2b - 5.2e), no obvious structural difference can be found. The change of the ratio of Y₂O₃ to AlN seemingly did not affect the total quantity and distribution of liquid phases in the intergranular spaces.

The XRD pattern of the sample sintered in Ar (C-60AlN-Ar) is shown in Fig. 5.3a. α -SiC and β -SiC are the major crystalline phases. The minor crystalline phases are identified as Y₂O₃ (JCPDS Nr. 43-0661 [JCP95]) and Y₁₀Al₂Si₃O₁₈N₄ (JCPDS Nr. 32-1426) which has frequently been detected when using Y₂O₃-AlN as sintering additives [NAD95, KEP98]. The XRD patterns of samples sintered in N₂ (Fig. 5.3b) indicate that they also contain α -SiC and β -SiC as major phases and Y₁₀Al₂Si₃O₁₈N₄ as minor phase; the difference is that a more N-rich phase, Y₂SiN₄O₃ (JCPDS Nr. 30-1460), and AlN (JCPDS Nr. 80-0010) are also identified as minor phases. With the increase of the Y₂O₃ to AlN ratio in the additives, the amount of Y₁₀Al₂Si₃O₁₈N₄ increases and that of Y₂SiN₄O₃ and AlN decreases (cf. Fig. 5.3b), but as shown in the SEM images, the total amount of intergranular phases stays constant (cf. Fig. 5.2 and Table 5.3)

Transmission electron microscopy was performed as shown in Fig. 5.4. Selected-area electron diffraction (SAD) was utilized to prove that the main part of the intergranular material was

amorphous. In other words, the minor crystalline phases detected by XRD represent only a small portion of the intergranular phase, highlighting the significance of microanalytical methods for identifying the composition of inter-crystalline phases.

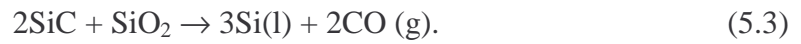
5.4 Chemical composition of intergranular phases

In backscattered-electron SEM images (e.g. Fig. 5.2d), there is a dark gray phase with faceted shapes, which is recognised as SiC, a light gray phase and spots of a bright white phase. Pores appear black. The light gray phase is distributed all over the intergranular regions and constitutes the main part of the intergranular phases. The WDS analysis results on the light gray intergranular phase of the samples sintered in Ar and N₂ are summarized in Fig. 5.5. An O-rich oxynitride phase, which is commonly observed as the main intergranular phase of liquid-phase sintered Si₃N₄ ceramics [LOE94], was also identified to account for the main part of the intergranular material in the SiC sample sintered in Ar (see Fig. 5.5a). In sharp contrast, a new amorphous phase which is rich in N, but depleted of O, was found to occupy much of the intergranular space in the SiC model systems sintered in N₂ (see Fig. 5.5b). The composition of this new phase remains stable as the ratio of Y₂O₃ to AlN in the additive is changed. Neither the O-rich phase in Fig. 5.5a nor the N-rich phases in Fig. 5.5b is corresponding to any crystalline phases identified by XRD analyses (Fig. 5.3), indicating that this main part of the intergranular phase with a light gray color in SEM images is amorphous, in agreement with the SAD observation (Fig. 5.4).

It is reasonable to consider that the O-rich phase in Fig. 5.5a originates from melting of the sintering additives Y₂O₃ and AlN, together with the SiO₂ introduced by surface oxidation of the SiC powder, at the lowest eutectic temperature of 1300-1350°C which is available in the Y-Si-Al-O-N system [LEW94]. According to the solution-precipitation sintering mechanism [GER85], small SiC grains may dissolve into the liquid intergranular phase and reprecipitate on larger SiC grains when saturation of the melt is reached. The overall composition of the melt remains within the glass-forming range of the Y-Si-Al-O-N system [LEW94], although carbon is known to facilitate the crystallization of silicate glasses at high temperatures [PAN98]. Hence, upon cooling, O, Y, N, Al, and dissolved Si and C form the amorphous oxynitride phase with the composition shown in Fig. 5.5a.

To understand the origin of the N-rich phase in SiC samples sintered in N₂ and its distribution over the intergranular space, WDS maps are helpful. Fig. 5.6 shows a BSE image and some maps of the element distribution in sample C-60AlN-N₂. Corresponding to the light gray intergranular phase which is visible in Fig. 5.6a, the Y, N and Si maps (Fig. 5.6b to 5.6d)

show a homogenous distribution of these elements over the intergranular regions, while O is nearly absent (see Fig. 5.6f, the regions with bright color marked by circles are due to pores with oxidized surfaces, corresponding to the black regions in the BSE image, Fig. 5.6a). The absence of O in the intergranular phase proves the important effect of N₂ as sintering atmosphere on the interfacial chemistry. During the heating period, the sintering behavior should be similar to that in Ar atmosphere, with an O-rich liquid phase forming between the SiC grains. At elevated temperatures, dissolution of N₂ into the liquid intergranular phase causes a sharp increase of its N content, while the decomposition reaction between SiC and oxides, such as SiO₂, which is always present on the surface of SiC powder, causes a decrease in O content, according to equation (4.1) and



The liquid Si may form bonds to dissolved N to form intergranular phases, which in turn encourages both the decomposition reaction and the dissolution of N. Finally, after a long enough sintering time, the N-rich amorphous phase would occupy the whole intergranular space. Although the low O content places its composition outside the glass-forming range of the Y-Si-Al-O-N system [LEW94], the amorphous state of the intergranular phase is retained under the present cooling conditions, because the high N content leads to a very high viscosity of silicate glass melts [KAP95]. Thus, crystallization is kinetically inhibited.

5.5 Crystalline intergranular phases

Although the main part of the intergranular phases remains amorphous during cooling, local crystallization is always present. Three crystalline intergranular phases, corresponding to the XRD results (Fig. 5.3b), have been found in the samples sintered in N₂. One of them is AlN, the element distribution of which can be clearly seen in Fig. 5.6f (Al map) and Fig. 5.6d (N map). Obviously, the solubility of AlN in the N-rich liquid phase is not high under the present sintering conditions. The Al content in the main intergranular phase always stays at a level of 2-3 at% (see Fig. 5.5b). The rest remains as excess crystalline AlN. A second crystalline phase appears as small spots in the N map (Fig. 5.6d, marked by arrows) but is absent in the Al map (Fig. 5.6f), indicating that it is a N-rich phase, corresponding to Y₂SiN₄O₃ which was identified by XRD. Both these crystalline phases show dark gray color in BSE images (Fig. 5.6a), similar to SiC grains. In contrast, the third intergranular crystalline phase appears as small bright white spots in BSE images (cf. Fig. 5.7). The WDS measurement indicates that it is a more O-rich phase. The composition of this phase corresponds to the Y₁₀Al₂Si₃O₁₈N₄ phase identified by XRD (Table 5.2). This O-rich crystalline phase (Y₁₀Al₂Si₃O₁₈N₄) is

always situated inside larger pockets of intergranular material where it is less exposed to the N_2 atmosphere during sintering (cf. Fig. 5.7).

The identification of the N-rich amorphous phase in the last section and of the N-rich crystalline phase $Y_2SiN_4O_3$ in the present section reveals the strong effect of the incorporation of N on the composition of the intergranular phases. Although using coarse SiC as starting powder causes the model system to stay far away from equilibrium during sintering, it is reasonable to consider that under the same sintering conditions, similar incorporation of N and similar interfacial reactions should happen when fine SiC powders are used for sintering. Therefore, the measured compositions of the intergranular phases in this model experiment could have value as a reference for understanding the intergranular phases in technologically relevant systems sintered from fine powders.

5.6 Effect of nitrogen incorporation

The model described above can serve to explain two practical phenomena. One is the observation [RIX00], that a N_2 overpressure is preferable to an Ar atmosphere for densification and microstructural control in the system SiC- Y_2O_3 -AlN. The observation that N_2 overpressure helps to suppress the decomposition of AlN at high temperature can now be complemented by considering the effect of the reaction between N_2 and SiC at high temperature. This reaction can accelerate the consumption of small SiC grains and increase the content of Si and C in the liquid intergranular phase (compare Fig. 5.5b to Fig. 5.5a), both mechanisms aiding solution-precipitation processes and therefore improving the sintering behavior. The other phenomenon which is characteristic of the additive system AlN- Y_2O_3 [KEP98], is that α -SiC sintered in N_2 atmosphere reveals increased bending strength upon annealing in air in a temperature range between 1000 and 1200°C. The reason was thought to be twofold: first, the healing of surface flaws and cracks by a glassy phase formed by oxidation; second, the oxidation of the intergranular oxynitride phases at elevated temperature leads to the formation of oxide phases, which is connected with a volume increase because the oxide phases can be assumed to have a lower density (or, in other words, to occupy a larger space) [RIX01]. With the insight gained from the present WDS measurements, this proposed mechanism can be confirmed and formulated more precisely: by conversion of the N-rich glass to an oxidic glass phase, large compressive stresses are expected to be built up, which leads to the observed surface strengthening effect. Since this mechanism is not available with

purely oxidic grain-boundary phases, the strengthening effect at high temperatures becomes a characteristic property of the additive system AlN-Y₂O₃.

Generally, the N-rich glass has a higher glass transition temperature than silicate glass and therefore, softening of the material is shifted to higher temperatures [LOE94]. The design of the additive composition and sintering process to remove all secondary phases in favour of the formation of the N-rich glass can improve the high-temperature strength retention and possibly also the creep resistance significantly.

Table 5.1 Compositions and sintering conditions of SiC samples

Sample	SiC : Additive	Y ₂ O ₃ : AlN	Sintering condition
	[vol%]	[mol%]	
C-60AlN-Ar	90:10	40:60	1950°C, 60min, 1MPa Ar
C-80AlN-N ₂	90:10	20:80	1950°C, 60min, 1MPa N ₂
C-60AlN-N ₂	90:10	40:60	1950°C, 60min, 1MPa N ₂
C-40AlN-N ₂	90:10	60:40	1950°C, 60min, 1MPa N ₂
C-25AlN-N ₂	90:10	75:25	1950°C, 60min, 1MPa N ₂

Table 5.2 Characteristics of liquid-phase sintered SiC samples

Sample	Weight loss [%]	Relative Density [%]	Crystalline Phase	
			Major	Minor
C-60AlN-Ar	2.8	66.8	α -SiC	Y ₁₀ Al ₂ Si ₃ O ₁₈ N ₄
			β -SiC	Y ₂ O ₃
C-80AlN-N ₂	2.2	68.8	α -SiC	Y ₁₀ Al ₂ Si ₃ O ₁₈ N ₄
C-60AlN-N ₂	1.8	67.9	β -SiC	AlN
C-40AlN-N ₂	1.8	67.4		Y ₂ Si ₃ O ₃ N ₄
C-25AlN-N ₂	1.6	67		

Table 5.3 The result of ImageC point-analysis measurement

	Content of intergranular phase, %
C-60AlN-Ar	5.6
C-80AlN-N ₂	16.5
C-60AlN-N ₂	16.0
C-40AlN-N ₂	15.1
C-25AlN-N ₂	17.6

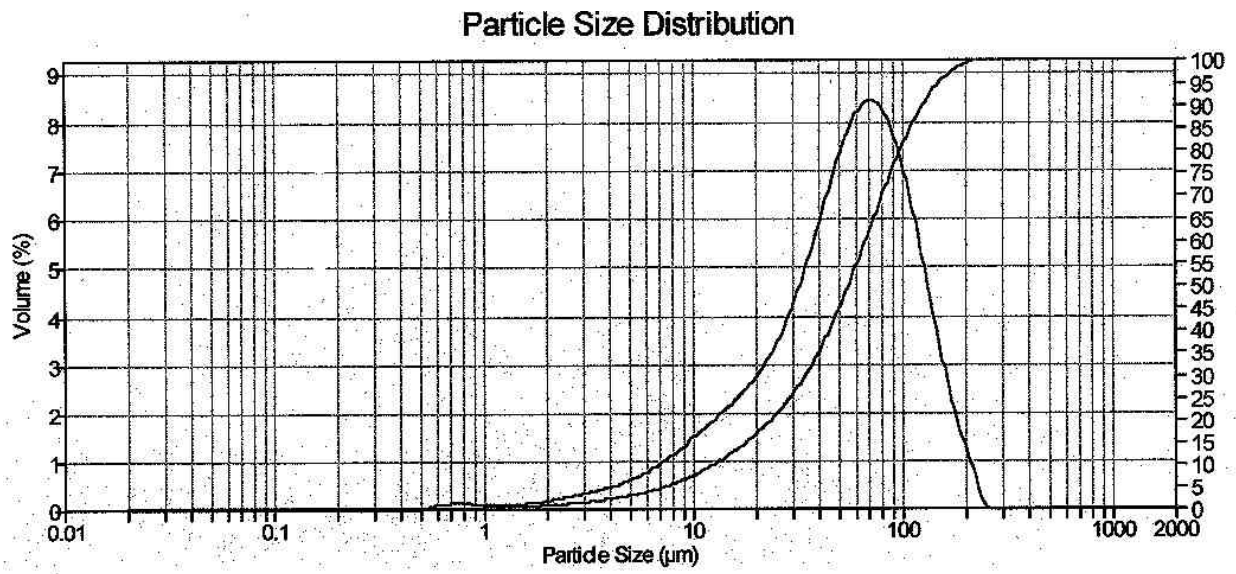


Fig. 5.1 Particle size distribution of the SiC powder selected for sintering. The volume weighted mean particle size is 64 µm.

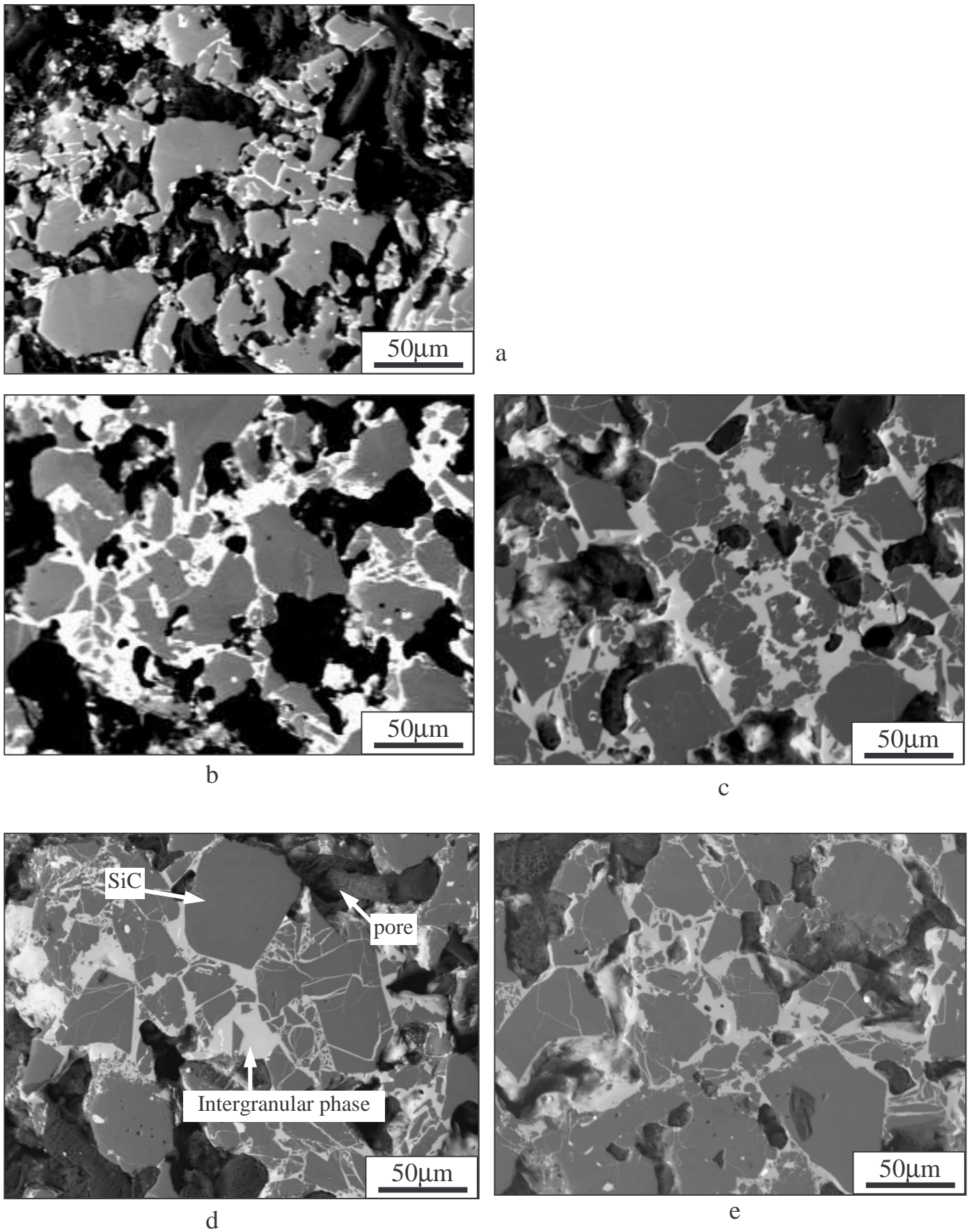


Fig. 5.2 Backscattered-electron SEM images of liquid-phase sintered coarse SiC: (a) Sample C-60AlN-Ar, (b) Sample C-25AlN-N₂, (c) Sample C-40AlN-N₂, (d) Sample C-60AlN-N₂, (e) Sample C-80AlN-N₂.

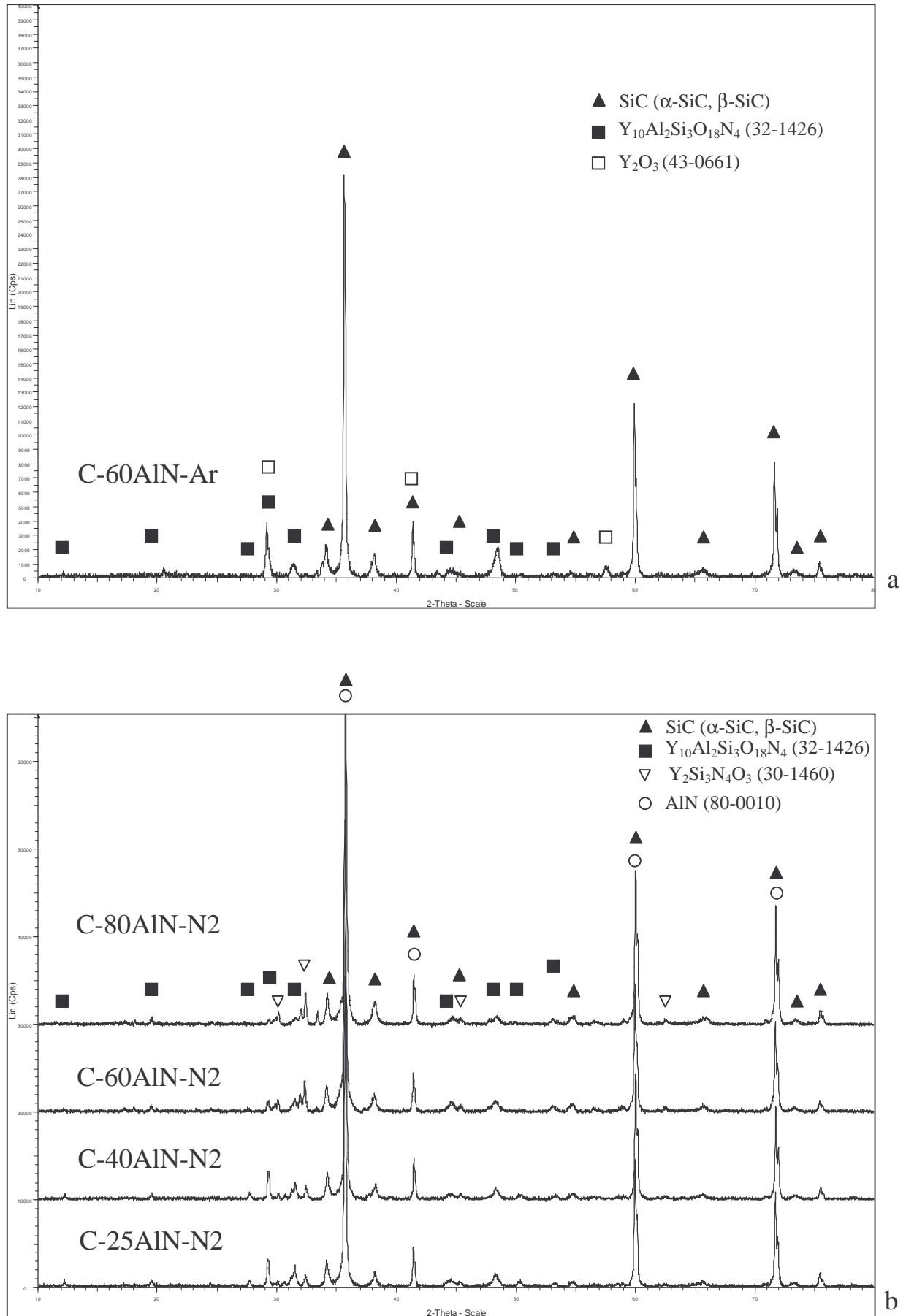


Fig. 5.3 XRD analyses of liquid-phase sintered coarse SiC: (a) sample sintered in Ar atmosphere, (b) samples sintered in N₂ atmosphere.

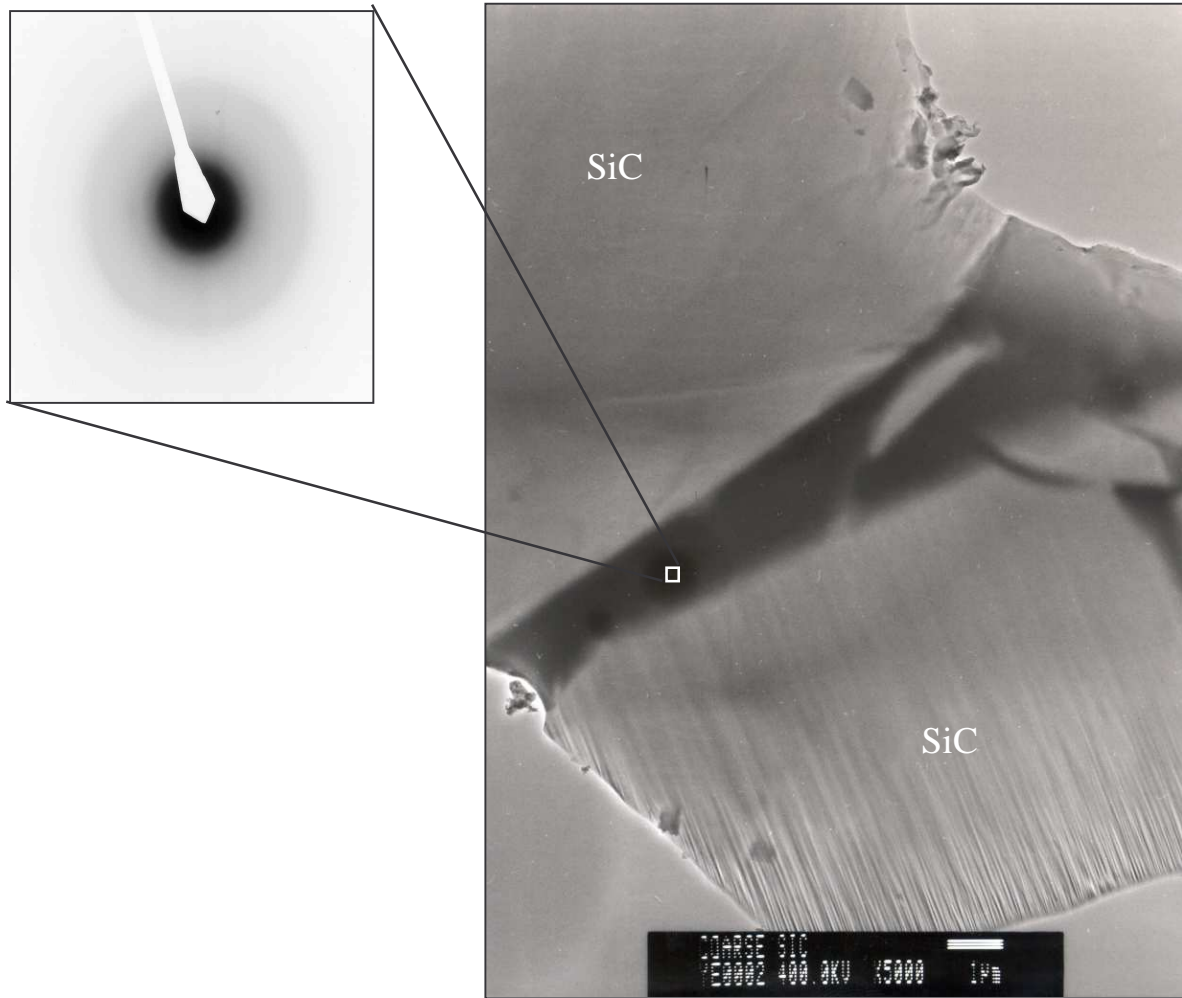
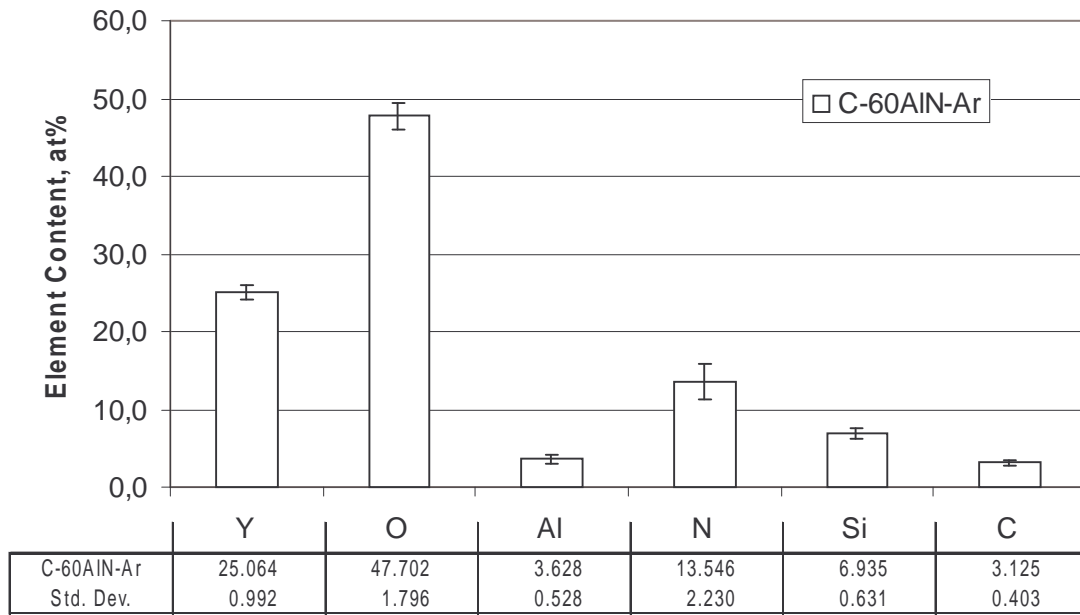
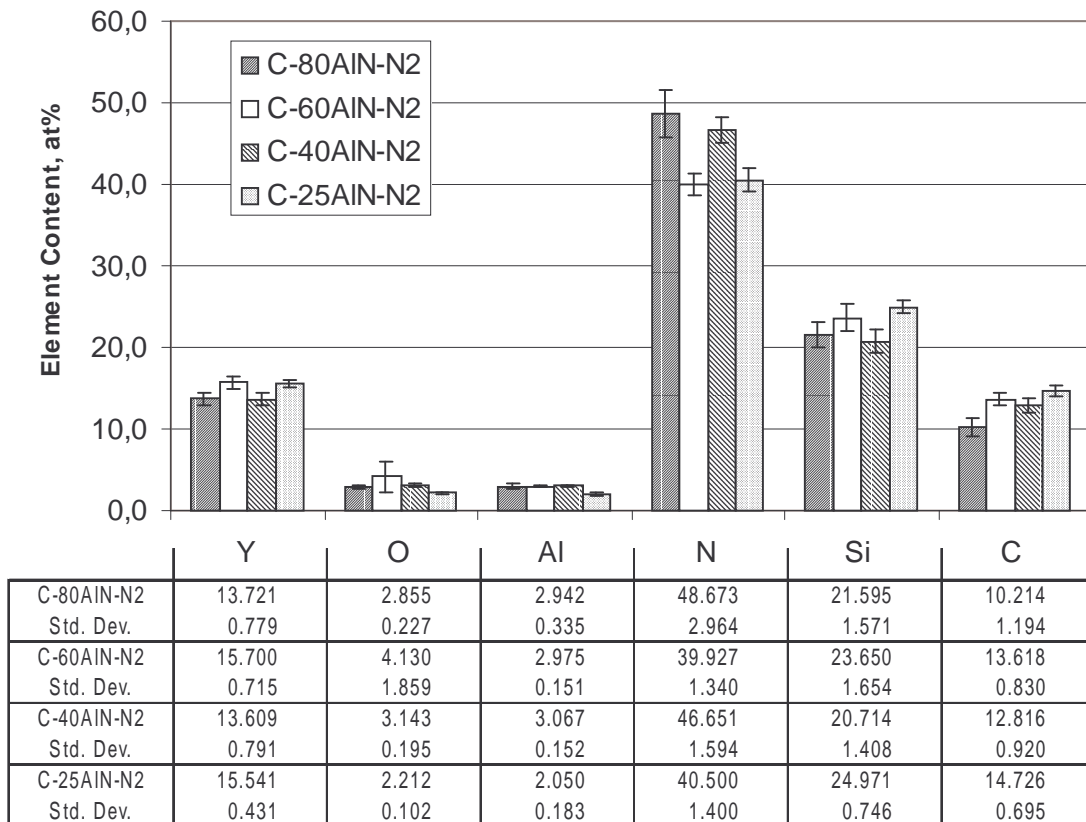


Fig. 5.4 TEM image and selected-area electron diffraction pattern of the intergranular phase in C-60AlN-N₂, showing that the intergranular phase is amorphous.



a



b

Fig. 5.5 WDS results on the amorphous intergranular phase of liquid phase sintered SiC, (a) sintered in Ar, (b) sintered in N₂. (Std. Dev. = standard deviation)

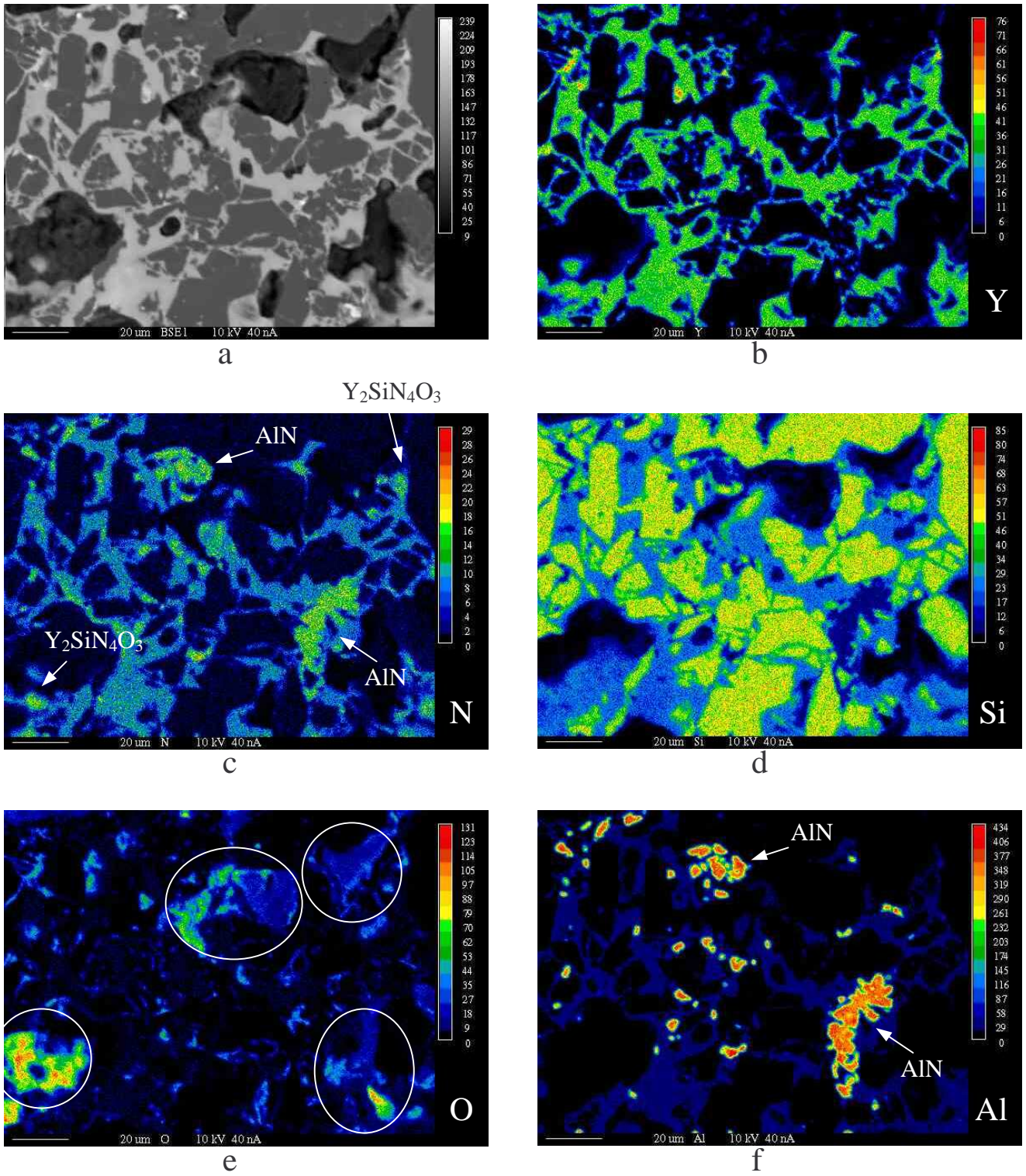
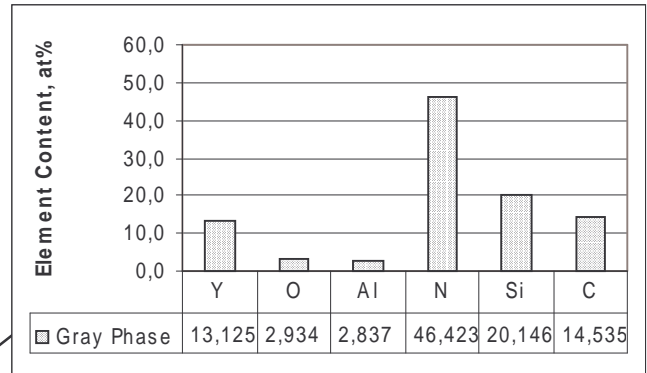
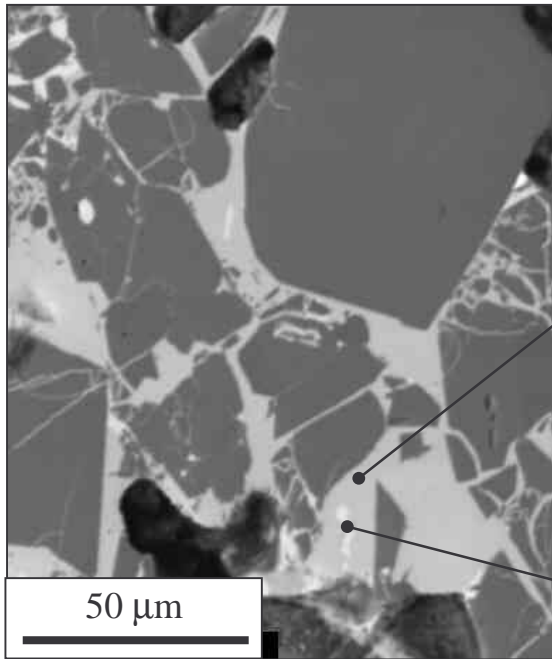
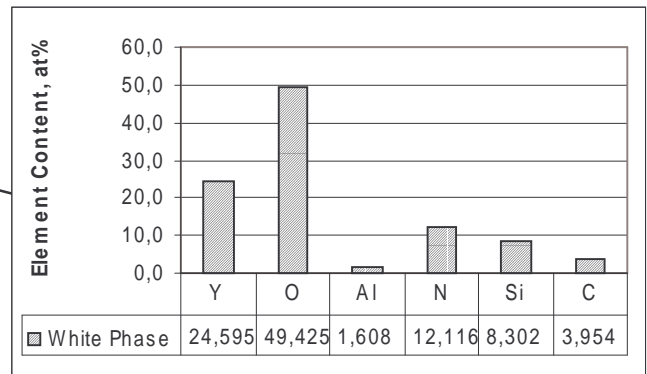


Fig. 5.6 WDS X-ray maps of the element distribution in C-60AlN-N2: (a) BSE image, (b) Y map, (c) N map, (d) Si map, (e) O map, (f) Al map. The cycles in the O map mark the position of holes, corresponding to the black regions in the BSE image.



Nitrogen-rich phase



Oxynitride phase

Fig. 5.7 SEM image and WDS results of C-60AlN-N₂, showing the existence of an oxynitride phase with a stoichiometry close to Y₁₀Al₂Si₃O₁₈N₄ as a secondary intergranular phase.

6 LPS-SiC WITH Y_2O_3 -AlN ADDITIVES

6.1 Introduction

Based on the knowledge gained from the model system SiC-SiO₂, where mainly the grain-boundary films were studied, and from the model system ‘coarse SiC with Y_2O_3 -AlN additives,’ where the chemical composition of triple-junction phases was quantitatively measured, investigations on a technologically relevant system, namely SiC- Y_2O_3 -AlN, will be reported in the present section. This SiC-based system has attracted an increasing attention in recent years [CHI94,WIE98,RIX00, BIS01] because it allows the introduction of N into the materials, resulting in an improvement of both sintering behavior and final mechanical properties. Although SEM was extensively utilized in these previous investigations in order to understand grain growth, phase transformation, crack extension and other microstructural properties, relatively little TEM work has been carried out on this material, especially on the nature of grain-boundary films and triple-junction phases. If spacially resolved knowledge about chemical composition is required, especially about the light element (N and O) content of grain-boundary films, TEM-based EELS analysis is recognized as a non-replaceable method. Therefore, in the present section, after the fabrication of dense SiC- Y_2O_3 -AlN samples, TEM and EELS as the principal methods of research were utilized to study the microstructure and chemistry in-depth.

6.2 Experimental procedure

Commercially available α -SiC (Grade A-10, H.C. Starck), β -SiC (Grade BF-12, H.C. Starck), AlN (Grade C, H.C. Starck), and Y_2O_3 (Grade C, H.C. Starck) were used as starting powders. The compositions of the various samples as well as their sintering conditions are specified in Table 6.1. Powder mixtures were prepared by attrition milling for 4 hours in isopropanol, using Si_3N_4 milling media. Then the slurry was separated from the milling media, dried at 65°C for 48 hours, and sieved to obtain homogeneously mixed, fine particle-size powders. The powders were cold isostatically pressed at 600 MPa to obtain the green bodies. Liquid-phase sintering was conducted in a gas pressure furnace with graphite heating elements (FCT, Germany). The sintering atmosphere was either N₂ or Ar with a maximum pressure of 1 MPa (see Table 6.1). The sintering temperature was always 1950°C with a

holding time of 1 hour. After sintering the samples were cooled at a rate of 20 K/min to 1500°C and then at a rate of ~50 K/min to room temperature.

The mass loss was measured for all samples. The densities were measured using Archimedes' method in water. X-ray powder diffractometry (D5000, Siemens) was performed using Cu K α radiation to identify the crystalline phases. For an estimate of the ratio of β -SiC to α -SiC during phase transformation, relative peak intensities were analyzed and compared with a calibration curve [WIE98].

100 α -60AlN samples sintered in N $_2$ (100 α -60AlN-N $_2$), 100 α -60AlN samples sintered in Ar (100 α -60AlN-Ar) and 90 β -60AlN samples sintered in N $_2$ (90 β -60AlN-N $_2$) were selected for TEM observations. TEM specimens were prepared by standard techniques, starting from mechanical slicing, polishing, dimpling and ending with ion-milling until perforation. The same equipment (JEM-4000EX, JEOL) and procedure as in the Chapter 5 were used to conduct the TEM and HRTEM observations. Spatially-resolved EELS analysis was performed on a dedicated scanning transmission electron microscope (Model HB501, Vacuum Generators, U.K.) equipped with a Gatan 666 Parallel EELS spectrometer. The electron probe diameter is around 0.5 nm, enabling spot analysis on selected regions of the samples. Besides, two other procedures were used for special analyses. First, the electron beam was scanned over square areas of 3 nm \times 4 nm on and off a grain-boundary film; the EELS data were integrated and compared to quantify excess concentrations of individual elements in the grain-boundary film. Second, a 'line-scan' mode was conducted by moving the electron probe across triple junctions and recording one spectrum per nanometer to study elemental distributions across the triple-junction phases. All the EELS spectra were processed and quantified through a special software, (EL/P, Gatan Inc.), with an uncertainty or deviation of about \pm 10%.

6.3 Densification

All samples were liquid-phase sintered to density higher than 90% of theoretical density. Fig. 6.1 shows the sintering behavior of α -SiC with different sintering additives under different sintering conditions. At 1950°C, sintering was more complete in N $_2$ than in Ar. Although infiltration of N from the sintering atmosphere into intergranular phases can increase their viscosity and obstruct the atomic transport [PRO79, JAC88], there is a beneficial effect of N on the decomposition reaction of AlN:



and this obviously played a more important role for a high final density. Within the same sintering processes (1950°C, N₂ or Ar), the highest relative density was always achieved when the chemical composition of the sintering additives was 60 mol% AlN and 40 mol% Y₂O₃. Results of the mass loss measurements are shown in Fig. 6.2. Since the decomposition of AlN was efficiently suppressed by sintering in N₂, smaller mass losses were detected in samples sintered in N₂, as compared to Ar. The remaining mass losses mainly result from the decomposition reaction between SiC and SiO₂ on the surface of the starting powders. Nevertheless, the mass losses increase along with increasing the AlN content in the sintering additive (40, 60 and 80 mol%). Full density was also achieved for 90β-60AlN which contains mainly β-SiC in the starting powder (see Section 6.5). Since a high degree of densification was consistently reached during a sintering time of one hour, the AlN-Y₂O₃ system was proven to be an efficient sintering additive.

6.4 Effect of sintering atmosphere on grain growth and densification

Fig. 6.3 shows two TEM bright-field images of the microstructures of α-SiC materials sintered at 1950°C in Ar (100α-60AlN-Ar) and in N₂ (100α-60AlN-N₂). The microstructural difference caused by the sintering atmospheres is clearly visible. Although both materials contain SiC particles with varied grain sizes, the grain size distribution is different: the amount of small grains is larger in the 100α-60AlN-Ar sample, or, the distribution of grain sizes is narrower in the 100α-60AlN-N₂ sample. The small grains (with a size less than 0.2 μm) have typically a round shape and are always surrounded by large intergranular pockets, as shown more clearly in Fig. 6.4, indicating an ongoing solution-reprecipitation sintering process. When this liquid-phase sintering mechanism is taken into account, the above-mentioned difference of grain-size distributions can be understood. In case of an N₂ sintering atmosphere, incorporation of N from the atmosphere increases the viscosity of intergranular liquid phases, reduces the mass transport, and slows down the solution and reprecipitation of SiC grains [PRO79, SEO92, LOE94]. The narrow grain-size distribution in the starting powders ($d(0.1) = 0.35 \mu\text{m}$, $d(0.5) = 0.95 \mu\text{m}$, $d(0.9) = 2.47 \mu\text{m}$, measured by laser granulometry) which is achieved by long-time attrition milling, can thus be kept until the final stage of sintering. In case of Ar as sintering atmosphere, on the contrary, the lower viscosity of the liquid phases encourages the dissolution of small grains and the reprecipitation of larger faceted grains, extending the grain size distribution to larger values.

Although grain growth is retarded by the incorporation of N_2 , the densification is not inhibited but accelerated, compared with the case of SiC sintered in Ar (cf. Fig. 6.1). This is different from the earlier opinion which had been gained from studying oxide-sintered SiC materials [PRO79, SEO92, LOE94]. The replacement of Al_2O_3 by AlN and the inhibition of AlN decomposition by N_2 is responsible for this difference, as detailed above. With both Ar and N_2 as sintering atmosphere, a sufficient amount of liquid phase is formed by reaction of AlN with Y_2O_3 , and thus grain rearrangement can proceed at the early stage of liquid-phase sintering, as it is evident from the fact that all intergranular regions have been fully filled by the liquid phase (see Fig. 6.3(b)). On the other hand, voids formed by the decomposition of AlN, which are found in 100 α -60AlN-Ar (as indicated by arrows in Fig. 6.5), are not present in 100 α -60AlN- N_2 . Retardation of grain growth and improvement of densification are therefore simultaneously existing in the SiC-oxynitride ceramics sintered under N_2 pressure, offering an efficient method to prepare homogeneous fine-grained materials.

6.5 SiC grain morphology and phase transformation.

Full density was achieved in sintered materials containing a mixture of 90% β -SiC and 10% α -SiC in the starting powder (90 β -60AlN- N_2). A TEM image of this material is shown in Fig. 6.6. The interlocking plate-like SiC grains indicate the β -to- α phase transformation which is accompanied by anisotropic grain growth [PAD94-1, NAD95, WIE98]. XRD analysis reveals that around 80% of the as-sintered SiC consist of the 6H polytype. Similar to the observations in liquid-phase sintered α -SiC materials, small and rounded grains could always be found in the large intergranular regions as shown in the dark field (DF) TEM image (Fig. 6.7), while large grains always appear faceted, as a result of the solution-reprecipitation sintering mechanism. Reprecipitation is accompanied by phase-transformation of the SiC grains. Fig. 6.8 shows a typical α -SiC grain, where the bands of contrast represent the stacking faults formed during grain growth. The spacing of the stacking faults appears quite uniform. No contrast change due to a core-rim structure could be observed. This is different from the SEM observations [BIS01, WIE98, NAD95] where the α -SiC seeds contained in the powder were often found to be present as 'core' regions of the final grains and reprecipitated SiC as 'rim' regions, but it is in agreement with the other TEM observations [FAL97, MOB96]. Compositional analyses are therefore necessary at this point, in order to quantify the impurities that are expected to be included in the SiC crystals during reprecipitation and grain

growth. Fig. 6.9(a) shows the EELS spectrum of the outer region of an α -SiC grain in 100 α -60AlN-N₂ samples. Fig. 6.9(b) is a partly magnified spectrum where the O edge is clearly visible, but the N edge is absent. Similar results could be achieved in other SiC grains as well as in 100 α -60AlN-Ar. The detection of O might arise from the dissolution of O or from the oxidation of the SiC grain surface. If O is an impurity dissolved in the SiC grains, the outer and center regions of SiC grains will contain different amounts of O. If the O is from surface oxidation of the TEM specimen, a homogeneous distribution of O over the SiC grains is to be expected. As a matter of fact, no O edge was found in the EELS spectra of the center region of SiC grains. It is therefore more reasonable to consider that the dissolution of O accounts for the phenomenon. Thus, the existence of differently doped zones in liquid-phase sintered SiC grains is confirmed. N appears to be incapable to dissolve into SiC grains in measurable quantities under the present sintering conditions, even though a quite high N content was present in the liquid phase due to the N₂ sintering atmosphere.

6.6 Grain-boundary films

6.6.1 HRTEM observation

The HRTEM images of all SiC samples examined reveal the presence of an amorphous film at grain boundaries, as shown in Fig. 6.10. The thickness of the grain-boundary films consistently ranged from 0.8 to 2.0 nm and was independent of grain misorientation, supporting Clarke's model [CLA87] regarding the equilibrium film thickness. Analogous to the discussion presented in Chapter 4, it is the presence of elements other than Si and O that stabilizes the amorphous films at the grain boundaries between SiC grains and leads to a finite equilibrium thickness. However, more detailed correlations between film thickness and sintering atmosphere, sintering temperature and SiC polytypes could not be established, because the uncertainties that exist with regard to thickness measurements for the thin (< 2 nm) films are too large. From the point of view of HRTEM, the distribution of the amorphous phase at grain boundaries is quite homogeneous. No voids and secondary crystals were present at the grain boundaries. Residual turbostratic carbon, however, although in very small quantity, was observed at non-equilibrium (i.e. thicker) grain boundaries of all samples (Fig. 6.11). The graphite may arise from the decomposition of SiC or from the excess carbon present as an impurity in the starting SiC powder [FAL97] and could significantly promote grain boundary sliding and relaxation of internal friction stresses [PEZ98].

6.6.2 EELS analyses and element excess

The different effects of sintering atmospheres on the grain-boundary films were revealed by measuring the composition of grain-boundary films by EELS. A typical EELS spectrum from a grain-boundary film in a 100 α -60AlN-Ar sample is shown in Fig. 6.12. The atomic ratio of N to O, as resulting from EELS elemental quantification, is shown to be 0.08. When the same procedure is performed with a 100 α -60AlN-N₂ sample, the N/O atomic ratio is much higher, about 0.5. It is therefore clear that using N₂ instead of Ar as sintering atmosphere largely increases the relative content of N in the grain boundaries. Two difficulties existing in this spectrum and also commonly encountered in all the other spectra are worth to be pointed out: firstly, the quantification of C at grain boundaries is not meaningful because carbon contamination from the residual gas atmosphere of the TEM always exists; and secondly, the Y M edge and Al L_{2,3} edge have relatively small intensity and are too close to, i.e. overlapped by the Si L edge, and therefore not visible in Fig. 6.12.

A more accurate EELS quantitative analytical method for evaluating the segregation in interface regions [GU98, IKE93, CHIA94] was applied to grain-boundary films in 100 α -60AlN-Ar and 100 α -60AlN-N₂. EELS information collected from an analysis region (3 × 4 nm²) on a grain-boundary film was compared with that from an analysis region of the same size located off the grain-boundary film (cf. Fig. 6.13). The excess Γ (atoms per area parallel to the grain-boundary film) of a segregated element at the grain boundary can then be calculated by

$$\Gamma_i = \frac{\sigma_r}{\sigma_i} \left(\frac{I_i^{on}}{I_r^{on}} - \frac{I_i^{off}}{I_r^{off}} \right) \cdot N_r \cdot w . \quad (6.2)$$

Here, ‘i’ and ‘r’ denote the segregated element and a bulk element used as the reference. ‘on’ and ‘off’ denote the analyzed boxes (on the grain-boundary film and off the grain-boundary film) from which the data are collected. I is the EELS edge intensity, and σ is the scattering cross section, the value of which can be obtained by analyzing the EELS spectra with a special software (EL/P, Gatan Inc.). N_r is the site density of the reference element in bulk grains, which is 48.3 atoms/nm³ in case Si from SiC grains is used as reference element. w is the width of the analysis region across the grain boundary (3 nm in the present analyses). One requirement for the reference element is that its concentration is sufficiently uniform regardless of the presence of a grain-boundary film. Therefore, in the case of SiC-based samples, Si was used as reference, based on which the excess amounts of N and O at grain boundaries were evaluated. The calculated elemental excesses (Γ_i) at grain boundaries are plotted in Fig. 6.14. The important effect of the sintering atmosphere on the composition of

grain-boundary films is clearly visible. The low N excess (7.7 atoms/nm^2) at grain boundaries in case of Ar as sintering atmosphere is dramatically increased to 52.5 atoms/nm^2 when N_2 is used as sintering atmosphere, while the O excess is independent of the sintering atmosphere within the experimental accuracy.

6.6.3 ELNES analyses and bonding information

As mentioned above, it is difficult to quantify the C excess at grain boundaries due to carbon contamination. Here, the energy-loss near-edge structure (ELNES) analysis can be beneficial to understand the carbon dissolution in the grain-boundary phase to some degree. Since ELNES is very sensitive to the nearest neighbors of the probed element, information about bonding, electronic structure and coordination can be obtained. Fig. 6.15 shows the ELNES of the Si $L_{2,3}$ edges from SiC, SiO_2 glass, and a grain-boundary film in $100\alpha\text{-60AlN-Ar}$. The different shapes of these near-edge structures reflect the different structural units, namely SiO_4 tetrahedra for SiO_2 and SiC_4 tetrahedra for SiC. Since the Si $L_{2,3}$ ELNES from the grain-boundary film has similarities to both reference spectra, the structural units of the grain-boundary film are concluded to contain Si-O as well as Si-C bonds. Although N dissolved in the grain boundaries could also cause the change in the shape of ELNES [GU96], this effect can be neglected here due to the small N excess at grain boundaries in the $100\alpha\text{-60AlN-Ar}$ materials. The finding that there is C at grain boundaries is unambiguous, because if all of the detected carbon arose from carbon contamination, the Si $L_{2,3}$ ELNES spectrum with a shape characteristic for mixed Si-C and Si-O bonds could not be observed.

Since N and C dissolution definitely leads to a high viscosity of silicate glass melts [KAP95, PEZ97, PEZ98], the present observation of N and C segregation at the grain-boundary films means that the viscous slip along grain boundaries, creep, plastic deformation and many other related mechanical properties will be strongly affected.

6.7 Triple-junction phases

6.7.1 Triple junctions and large pockets

Generally there are two kinds of geometries at multigrain junctions in the studied SiC samples: one is the intergranular phase between three or four contacting SiC grains with a size around 50 nm, called triple junctions, as shown in Fig. 6.16(a); the other is formed by much larger regions (more than 500 nm in diameter), which are surrounded by multiple SiC grains, as shown in Fig. 6.16(b). While these configurations, which are called large pockets, could be

'holes' due to imperfect particle compaction or remaining after the dissolution of SiC grains at elevated temperature, the small triple junctions can be considered to be the result of the reprecipitation and grain growth of the SiC particles. Compared with materials sintered from α -SiC powder, those using β -SiC as main component of the starting powder exhibit a larger amount of large pockets, because the grain growth accompanying the β -to- α phase transformation of SiC is anisotropic: along the basal (0001) plane of α -SiC, the small triple junctions are very likely to be formed during anisotropic grain growth, as shown exemplary in Fig. 6.17 (indicated by 'A'). In the direction perpendicular to the basal plane, in contrast, the grain growth is so slow that large pockets are difficult to be removed (Fig. 6.17, indicated by 'B'). Filling of the large pockets requires more liquid and therefore complicates densification. [KIM98, PAD94-2].

6.7.2 Crystallization of phases at triple junctions and large pockets

Crystallization of the triple-junction phases has been found in all the sintered samples. Fig. 6.18 shows an overview of a crystallized triple-junction phase in 100 α -60AlN-Ar. The size of this typical triple junction is only 20 nm. Crystallized triple-junction phases have also been observed in 100 α -60AlN-N₂ and 90 β -60AlN-N₂. Like small triple junctions, large pockets are also filled with secondary crystalline phases, as shown in Fig. 6.19. Through careful adjustment (tilting) to remove the moire fringes caused by the lattice fringe overlap of triple-junction phases and SiC grains (cf. Fig. 6.20), the crystallization in triple junctions was found to be incomplete, with residual amorphous phases at the interface between secondary crystalline phases and SiC grains and at the tip of the corners, as shown in Fig. 6.21. This observation is in agreement with theoretical work by Raj [RAJ81], who suggested that the hydrostatic stresses arising from the volume change during crystallization of the intergranular phases inhibit the completion of their crystallization.

6.7.3 Identification of the secondary crystalline phases

XRD analyses were used to identify the secondary crystalline phases. Fig. 6.22(a) and Fig. 6.22(b) show XRD results of the SiC samples sintered in Ar and sintered in N₂ atmosphere. Besides α -SiC as main crystalline phase, Y₁₀Al₂Si₃O₁₈N₄ was identified to be the secondary phase in SiC sintered in Ar, while Y₁₀Al₂Si₃O₁₈N₄ and Y₂Si₄O₃ were identified to be the secondary phases in SiC sintered in N₂. With increasing Y₂O₃ content in the additive, the content of these secondary phases in the materials also increased, indicating the important role Y₂O₃ plays in forming such secondary phases. The identification of Y₁₀Al₂Si₃O₁₈N₄, which is believed to be formed preferentially upon the crystallization of Y₂O₃-AlN-SiO₂ glass melts

during cooling, is consistent with previous research on liquid-phase sintering in the SiC-AlN-Y₂O₃ system [KEP98, NAD95, WIE98]. The more N-rich crystalline phase, Y₂SiN₄O₃, was also detected, in trace amounts, by XRD analyses of SiC materials in the second model experiment (refer to Chapter 4). In the phase diagram of the Y-Si-N-O system [SUN91] Y₂SiN₄O₃ is the quaternary compound with the highest N content. The formation of Y₂SiN₄O₃ indicates the important effect of N on the crystallization of triple-junction phases. The identification of these secondary crystalline phases and evaluation of their distribution in the intergranular regions were performed by EELS analysis, as follows.

6.7.4 EELS analyses and confirmation of N-rich triple-junction phases

Fig. 6.23(a) shows a crystallized triple-junction phase of 100 α -60AlN-Ar, in the center of which an EELS spectrum was recorded, as shown in Fig. 6.23(b). According to its N/O atomic ratio, and combining with the XRD analysis results (Fig. 6.22(a)), the triple-junction phase was identified as Y₁₀Al₂Si₃O₁₈N₄. Similar spectra could also be measured in other triple junctions and large pockets of the same sample, which is in agreement with the XRD result that only one type of secondary crystalline phase exists in 100 α -60AlN-Ar. Different secondary crystalline phases were detected in 100 α -60AlN-N₂ by EELS atomic-ratio analyses, as shown in Fig. 6.23, where triple junctions with a surprisingly sharp N edge correspond to Y₂SiN₄O₃ (Fig. 6.23 (c,d) and cf. Fig. 6.22(b)) whereas large pockets contain Y₁₀Al₂Si₃O₁₈N₄ (Fig. 6.23 (e,f) and cf. Fig. 6.22(b)). So again, the EELS analyses confirm the XRD results. The advantage of using EELS analyses here is that not only the existence of two secondary crystalline phases is confirmed, but also the distribution of the phases along the intergranular spaces is recognized. Moreover, the reason of the phase separation can be understood, as the following discussion will show.

The incorporation of N into the intergranular phase in 100 α -60AlN-N₂ is still the basic reason of the phase separation. At elevated temperature, direct incorporation of N from the sintering atmosphere and the suppression of the decomposition reaction of AlN by N₂ overpressure both act to increase the N content and thus the viscosity of the liquid intergranular phases. These viscous liquids are redistributed among the SiC grains as the grain rearrangement and solution-precipitation sintering mechanisms proceed. In a situation as shown in Fig. 6.24, the viscous flow from triple junctions to large pockets (along the arrows) becomes difficult due to the hindrance by the small rounded grain 'A', which is undergoing the solution process. This difficulty will even be increased when grain growth of grain 'B' and grain 'C' narrows the flow path. In this situation, phase separation of the intergranular liquid may

happen. A liquid phase rich in O and therefore possessing a low viscosity would easily flow into the large pockets, while liquid phase rich in N and having therefore a high viscosity would preferentially remain in the triple junctions. Finally, different liquid phases would occupy the large pockets and the triple junctions and, after cooling and crystallization, form the O-rich $Y_{10}Al_2Si_3O_{18}N_4$ and N-rich $Y_2SiN_4O_3$ phases, respectively.

It should be stressed that this “entrapment” mechanism does not depend on a situation same to Fig. 6.24. Anytime when a narrow channel forms in the way of viscous flow, the entrapment of the phase with higher viscosity might happen. Since in the final stage of the liquid-phase sintering, the SiC grains continuously grow and gradually approach each other, the formation of the narrow channels between grains becomes unavoidable. Therefore the phase separation described above is common phenomenon and becomes the characteristic of 100 α -60AlN-N₂. In 100 α -60AlN-Ar, where the N content is low and the liquid phase has a very low viscosity throughout, such a phase separation is not present.

6.7.5 Distribution of elements across triple-junction phases

Along with the crystallization of triple-junction phases, the residual amorphous phase segregates to the interface between SiC grains and the secondary crystalline phases, as observed by HRTEM and discussed before. By using line-scanning EELS analyses, information about the elemental distribution in the amorphous interface is available. Fig. 6.25 shows the analysis result of 100 α -60AlN-Ar. The microprobe line-scan leading from one of the surrounding SiC grains into the center of the triple junction reveals an intensity variation of the Si, C, N, and O edges. Different from Si, C and O maps showing a gradual intensity decrease or increase, the N map contains a sharp peak in the region which is corresponding to the amorphous interface. Two reasons can be responsible for the N enrichment at interfaces: firstly, analogous to the discovery in the model system SiC-SiO₂ (cf. Section 4.5), the surface of SiC is a preferred place for N segregation; and secondly, as a result of crystallization of the O-rich triple-junction phase, the excess N is driven to the interface. By measuring the width of the peak in the N map, the thickness of the amorphous interface is evaluated to be approximately 3 nm.

The same analysis was conducted in 100 α -60AlN-N₂, with the result shown in Fig. 6.26. In this case the electron probe was moved from one SiC grain via the triple junction to another SiC grain. Similarly, the triple junction contains a lower amount of Si and C than SiC grains (after removing the carbon contamination effect). But the distribution of N and O across the triple junction is totally different from that measured in the 100 α -60AlN-Ar sample (cf. Fig.

6.25). In this case N is enriched in the triple junction, because of the reason discussed before (cf. Section 6.7.4). O is driven to the interface. But it seems that the N on the surface of SiC grains cannot be totally replaced by O. So there are actually two layers in the interface, one being the N-rich interface (corresponding to the peaks at 8 nm and 35 nm in the N map), and the other being the O-rich interface (corresponding to the peaks at 12 nm and 32 nm in O map). The N-rich interface layer is close to the SiC grain, while the O-rich interface layer is facing the triple junction phase. The thickness of the whole interface is about 5 nm. The causes of such a characteristic interface structure is not clear. More detailed investigations are required to this end in the future.

Table 6.1 Compositions and sintering conditions of the liquid-phase sintered SiC-based samples.

Nomenclature	SiC : Additive (vol%)	α -SiC : β -SiC (mol%)	AlN : Y ₂ O ₃ (mol%)	Sintering Temp. (°C)	Sintering Atmosphere (max. pressure)
100 α -40AlN	90 : 10	100 : 0	40 : 60	1950	1 MPa Ar or 1 MPa N ₂
100 α -60AlN	90 : 10	100 : 0	60 : 40	1950	1 MPa Ar (100 α -60AlN-Ar) or 1 MPa N ₂ (100 α -60AlN-N ₂)
100 α -80AlN	90 : 10	100 : 0	80 : 20	1950	1 MPa Ar or 1 MPa N ₂
90 β -60AlN	90 : 10	10 : 90	60 : 40	1950	1 MPa N ₂ (90 β -60AlN-N ₂)

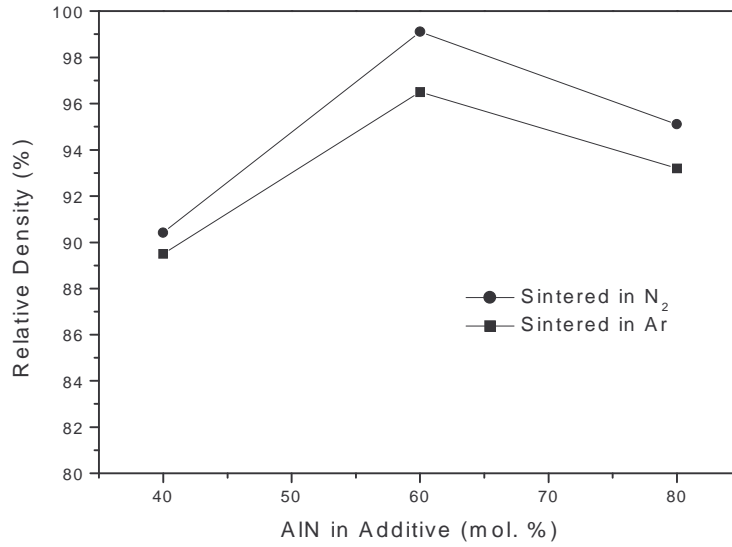


Fig. 6.1 Effect of AlN content in additive and sintering atmosphere on the relative density of liquid-phase sintered SiC-based samples.

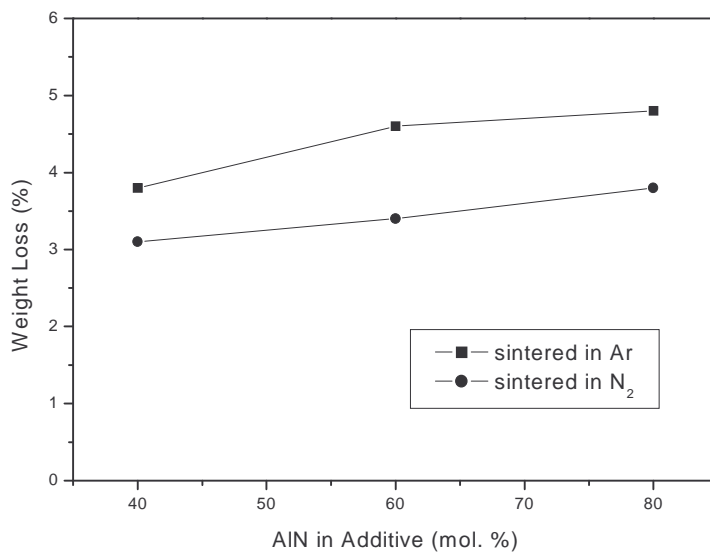


Fig. 6.2 Effect of AlN content in additive and sintering atmosphere on the weight loss of liquid-phase sintered SiC-based samples.



a



b

Fig. 6.3 TEM bright-field images of the overall microstructures of 100 α -60AlN samples sintered at 1950°C, (a) in Ar (100 α -60AlN-Ar) and (b) in N₂ (100 α -60AlN-N₂).



Fig. 6.4 TEM image of 100α-60AlN-Ar, showing typical small SiC grains (indicated by arrows) which have round shapes and are located inside large intergranular pockets, indicating an ongoing solution-precipitation process.

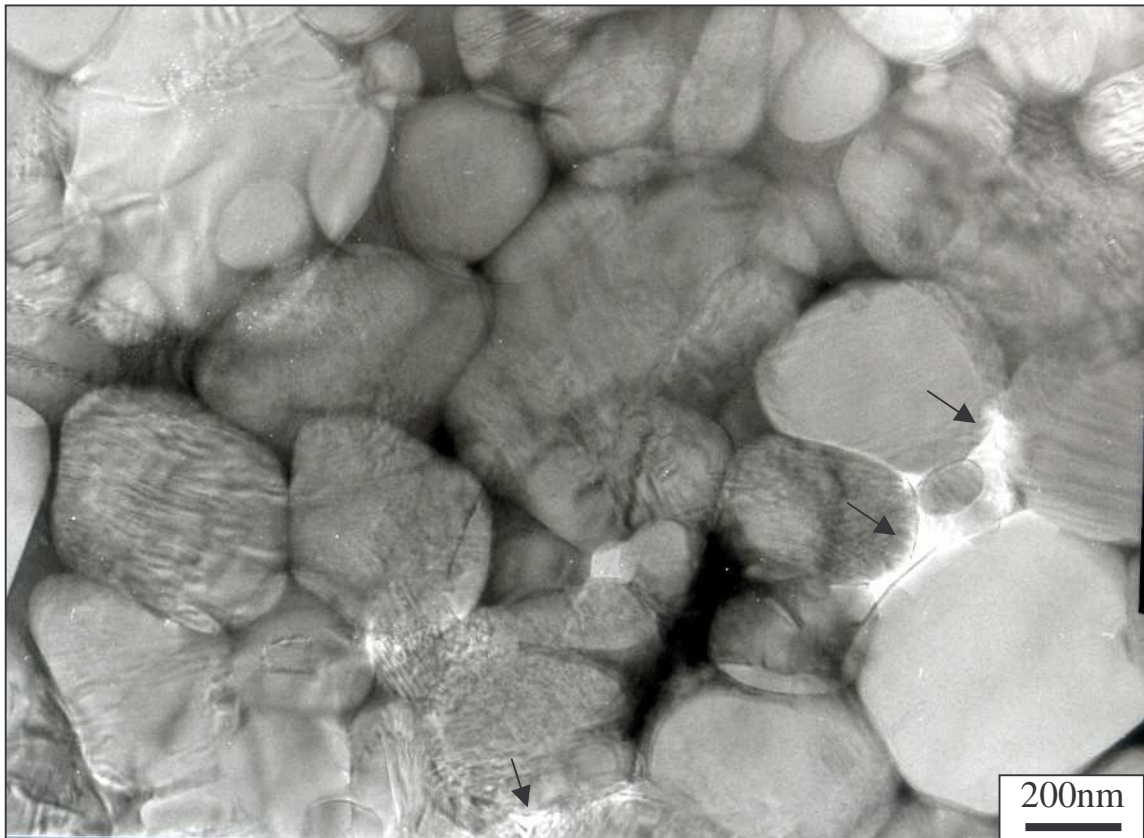


Fig. 6.5 TEM image of 100 α -60AlN-Ar sample, showing the existence of voids at the triple junctions, as indicated by arrows.



Fig. 6.6 TEM image of liquid-phase sintered sample using β -SiC as main component of the starting powder (90 β -60AlN-N₂). The elongated SiC grains have actually plate-like shape, indicating the β -to- α -SiC phase transformation.

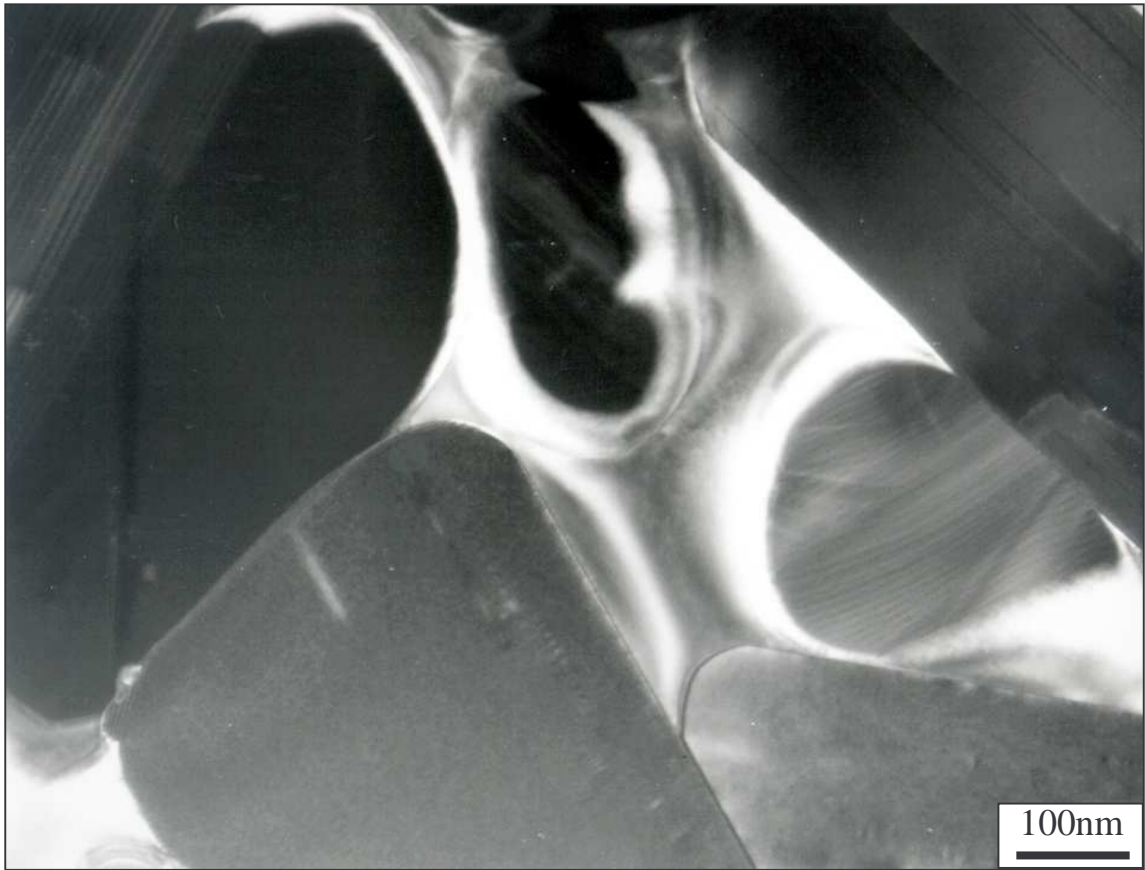


Fig. 6.7 Dark-field TEM image of 90 β -60AlN-N₂, where the intergranular phase is seen in bright contrast and SiC grains in dark contrast. The small grain surrounded by intergranular phase is the result of the ongoing solution-precipitation process.

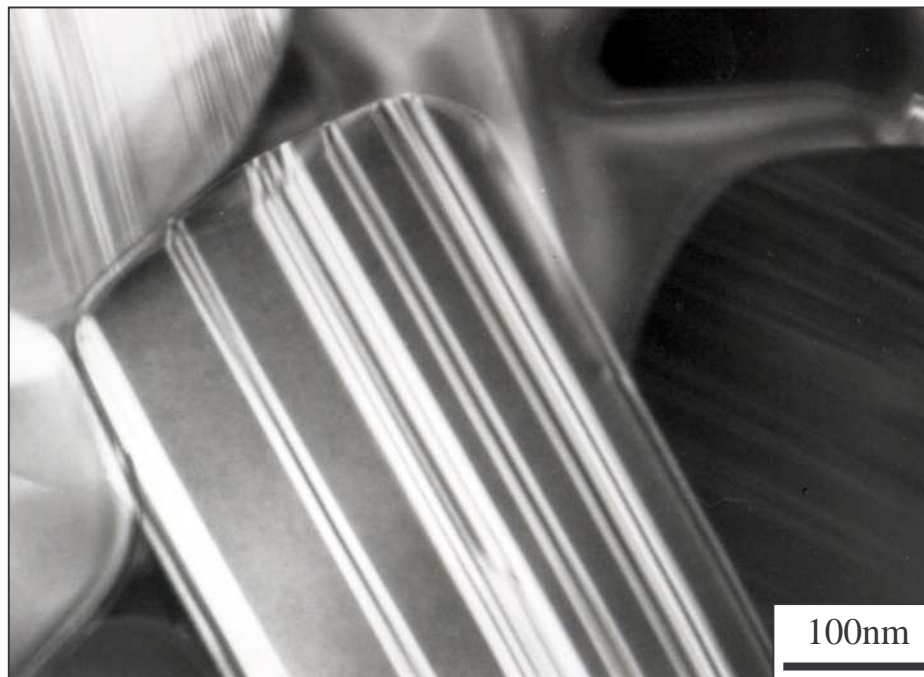


Fig. 6.8 A exemplary epitaxially grown SiC grain. The typical core-rim structure of liquid phase sintered SiC grains is not visible in TEM image.

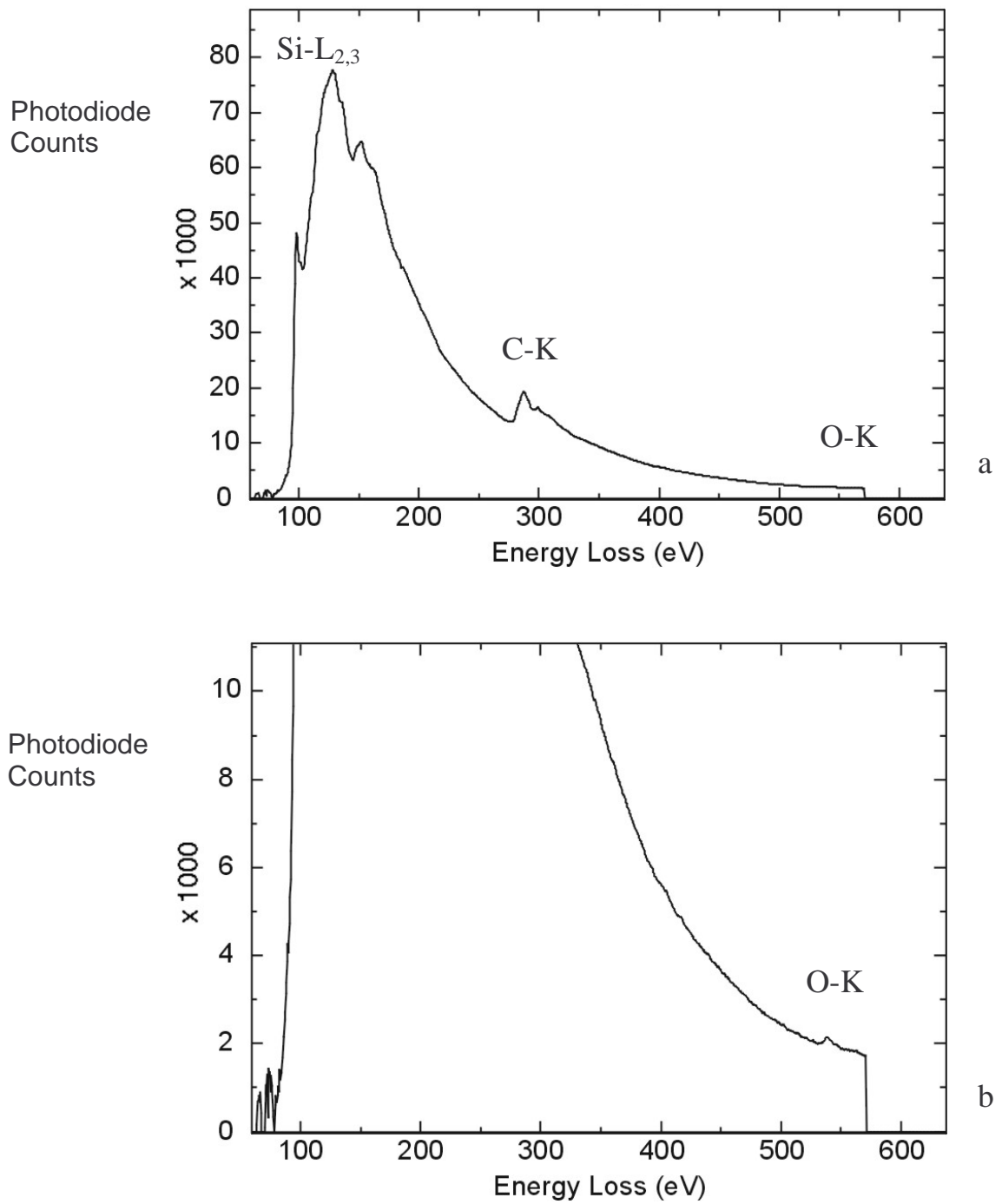


Fig. 6.9 (a) EELS spectrum of a rim region of a plate-like α -SiC grain in 90 β -60AlN-N₂; (b) same spectrum magnified in y direction, revealing the existence of O in the rim region. No N can be detected.

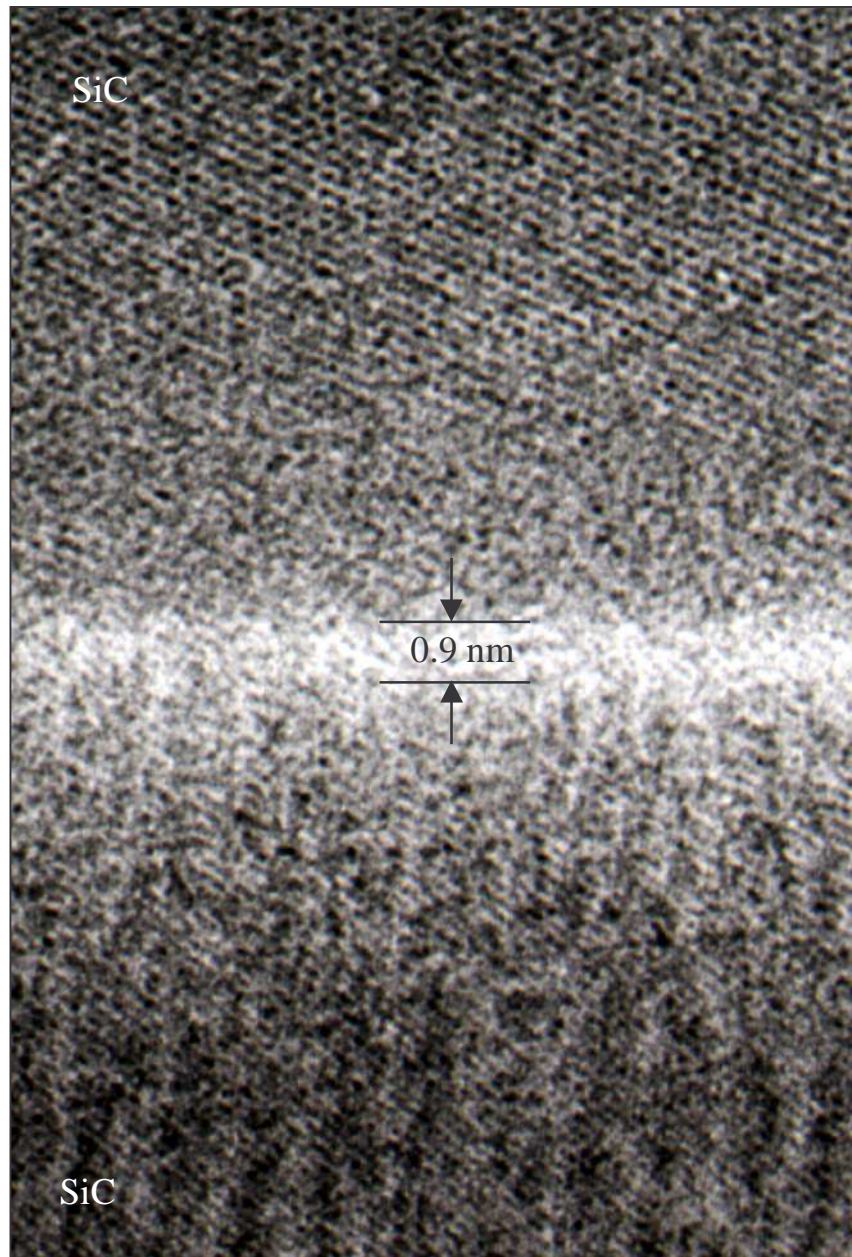


Fig. 6.10 HRTEM image of a typical grain boundary in $100\alpha\text{-}60\text{AlN-N}_2$ with a thickness of 0.9 nm.

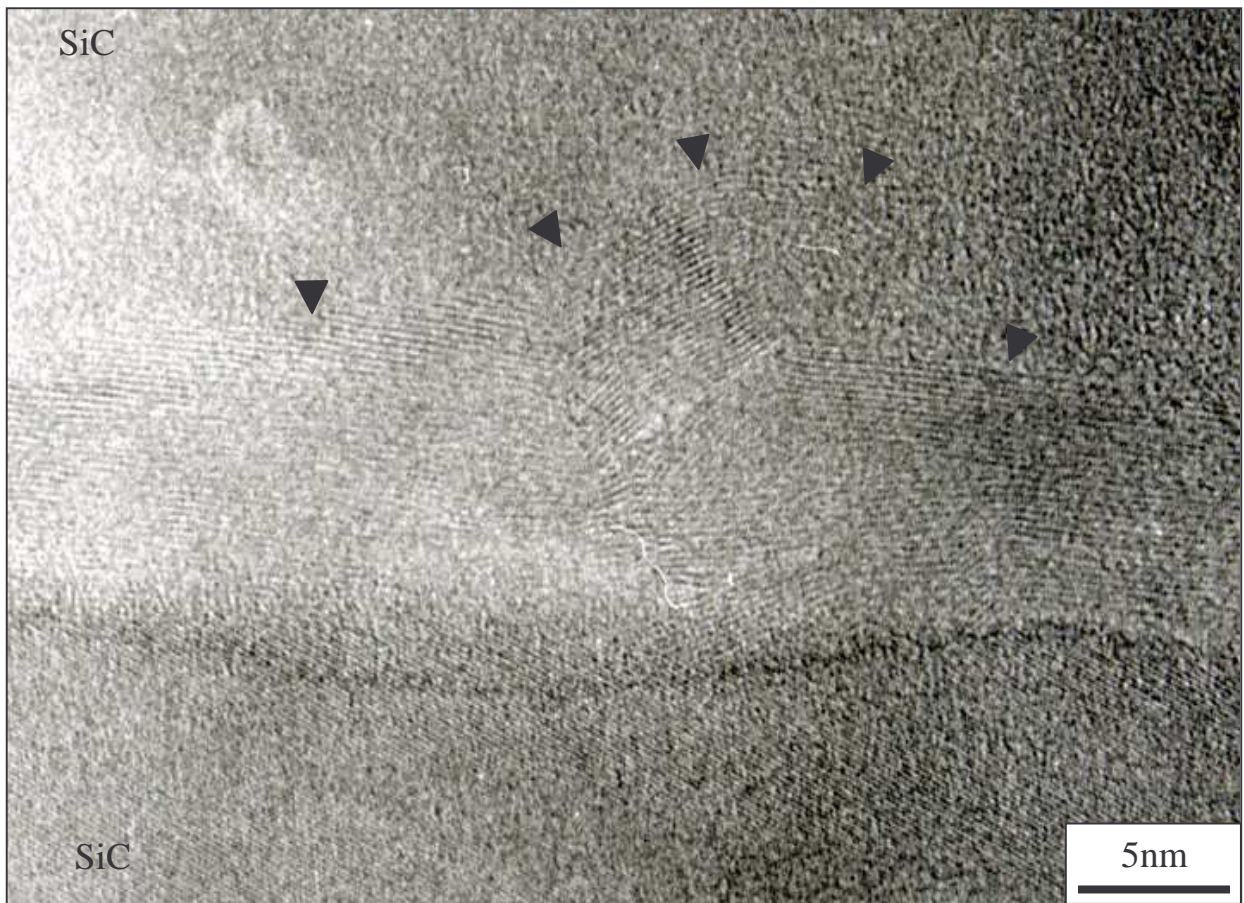


Fig. 6.11 HRTEM observation of residual turbostratic carbon at the grain boundary in 100α -60AlN-Ar. The characteristic lattice fringes of carbon are indicated by arrows.

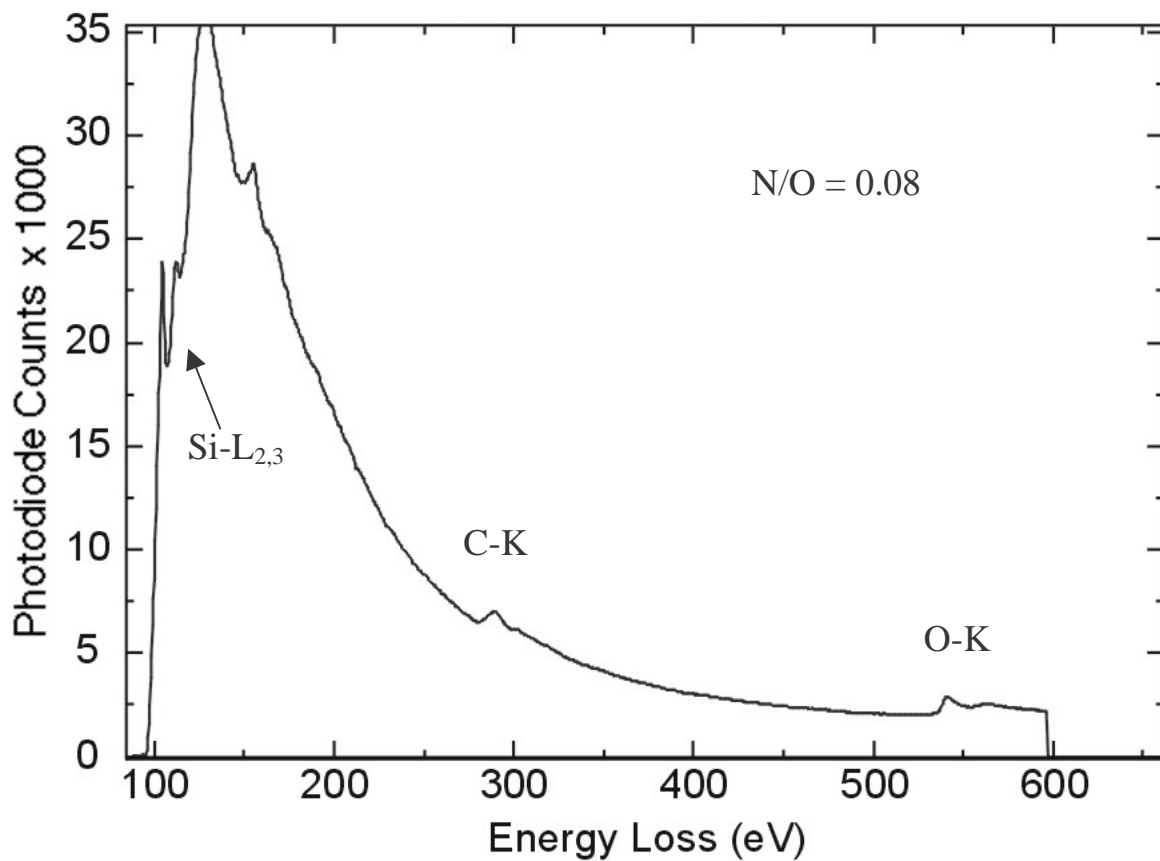


Fig. 6.12 Typical EELS spectrum of a grain-boundary film in 100α -60AlN-Ar. N/O atomic ratio is calculated to be 0.08.

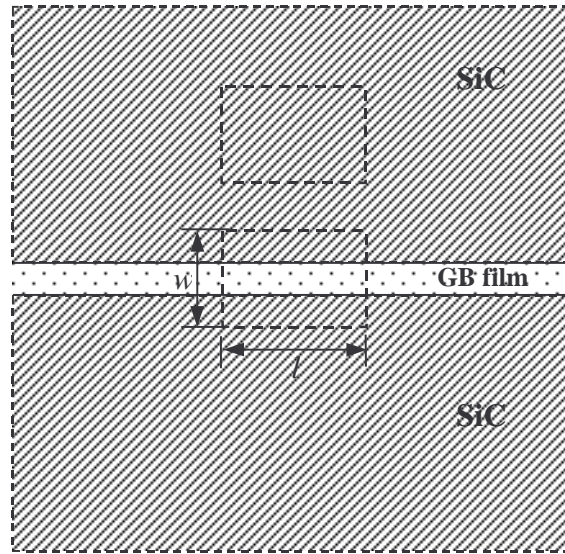


Fig. 6.13 Illustration of two analysis boxes on and off a GB film used to quantify the elemental segregation excess.

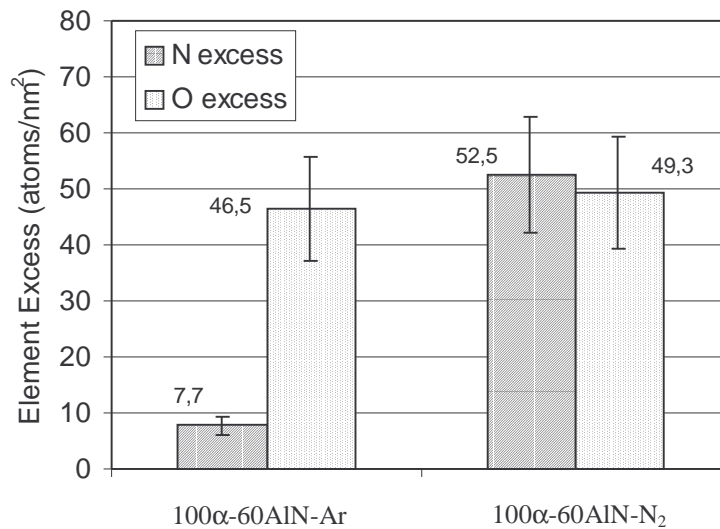


Fig. 6.14 Calculated N excess and O excess (atoms per area parallel to GB film) at grain boundaries in 100α-60AlN-Ar and 100α-60AlN-N₂. The N excess at grain boundaries is largely increased by using N₂ as sintering atmosphere.

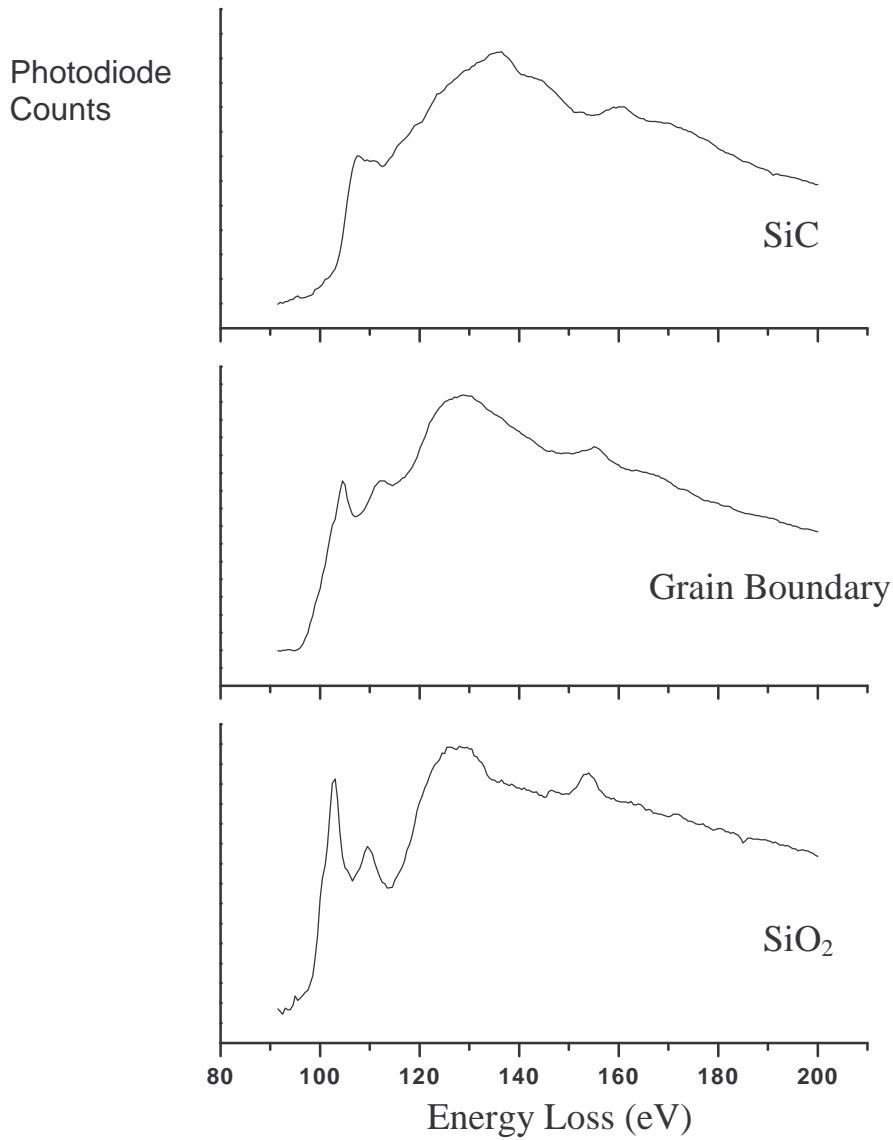


Fig. 6.15 ELNES of the Si L_{2,3} edge from a grain-boundary film in 100 α -60AlN-Ar, in comparison with those from two references (SiC grain and SiO₂ glass). Similarities of the near-edge structure of the GB film with both references indicate that the tetrahedral units in the GB film contain both Si-C and Si-O bonds.

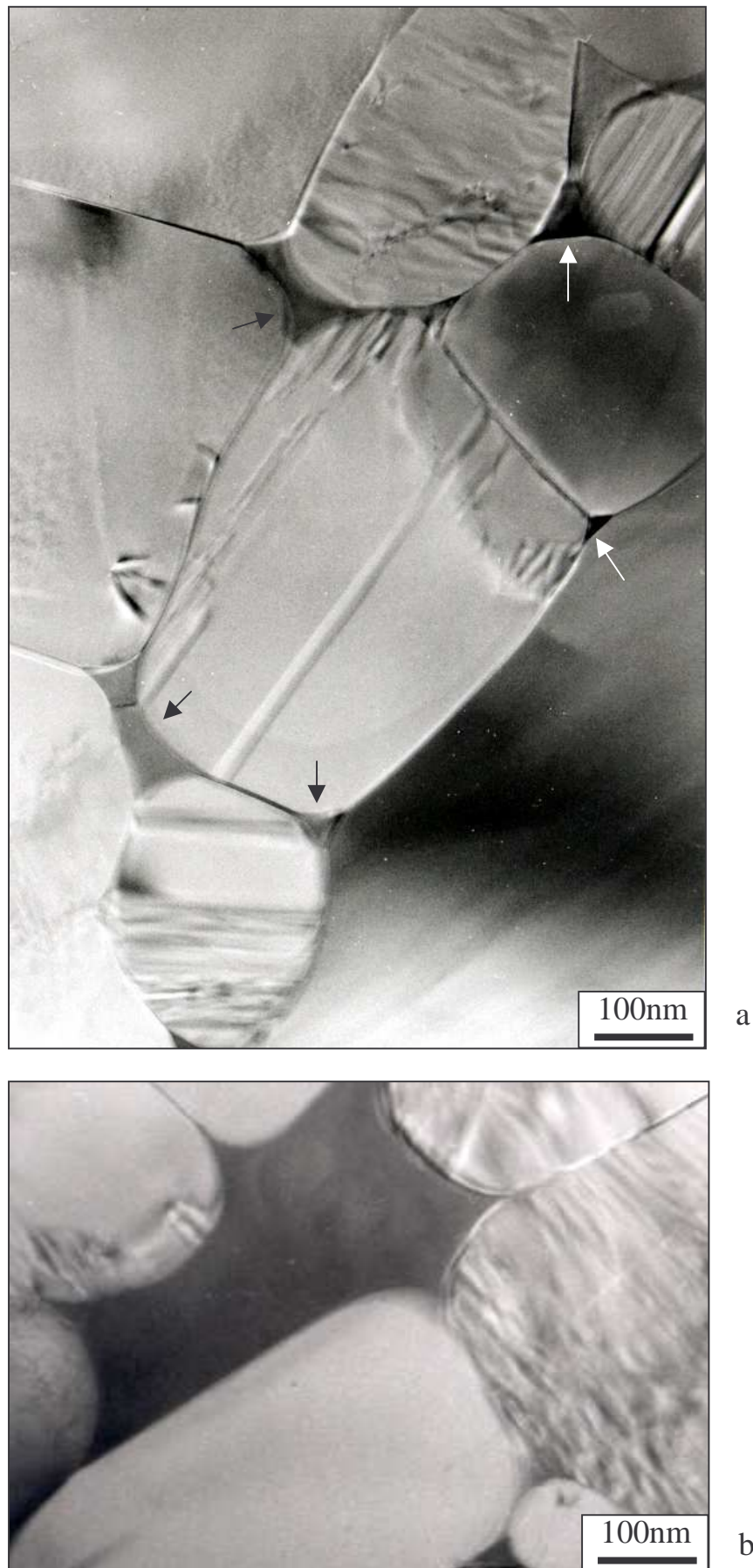


Fig. 6.16 Two kinds of geometries at multigrain junctions: (a) triple junctions, which are in-between three or four SiC grains and have an average size of 50 nm; (b) large pockets, which are normally surrounded by more than five grains and have diameters larger than 500 nm.

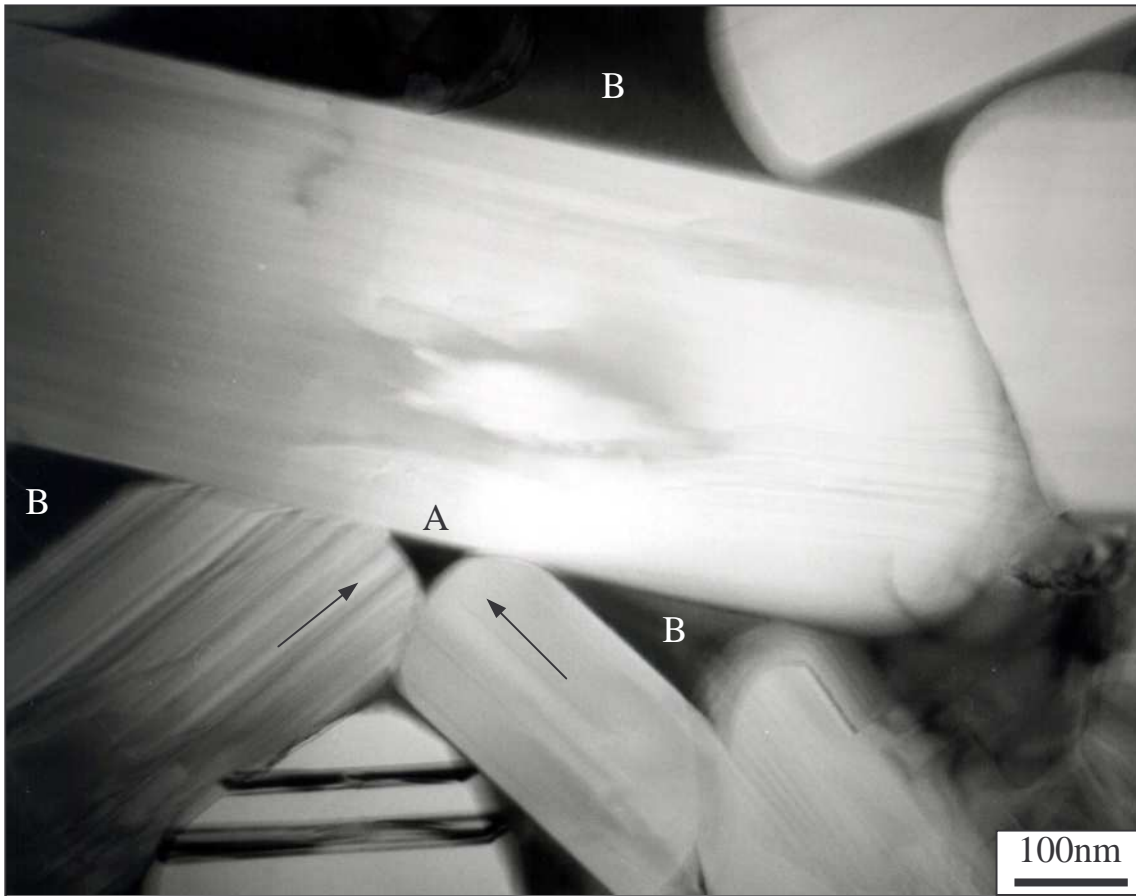


Fig. 6.17 TEM image of triple junctions in 90 β -60AlN-N₂. Depending on the direction of grain growth, some triple junctions (indicated by B) are more difficult to be reduced in size than others (indicated by A).

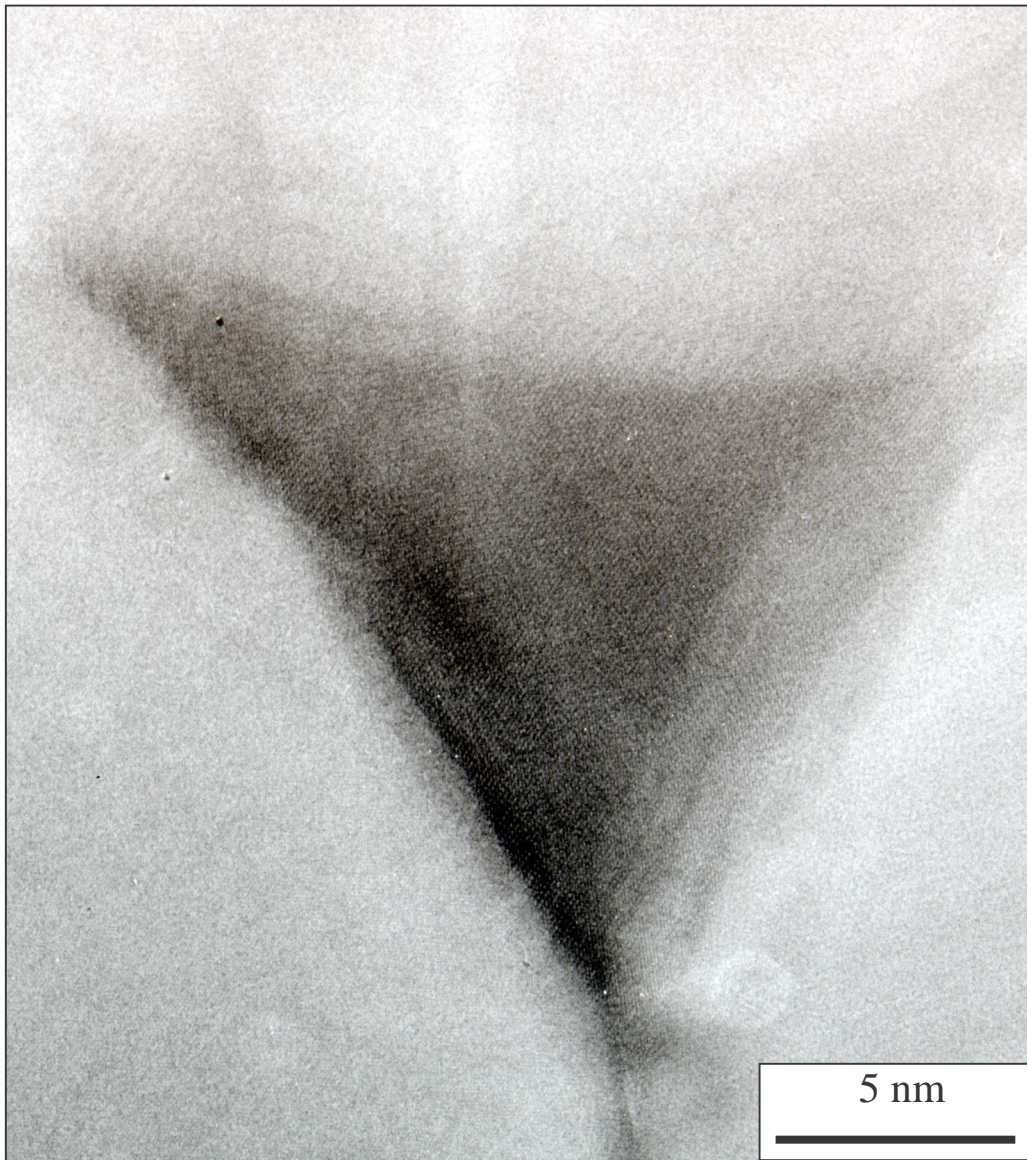


Fig. 6.18 HRTEM image of crystallization inside a typical triple junction in 100 α -60AlN-Ar. The side length is about 20 nm.

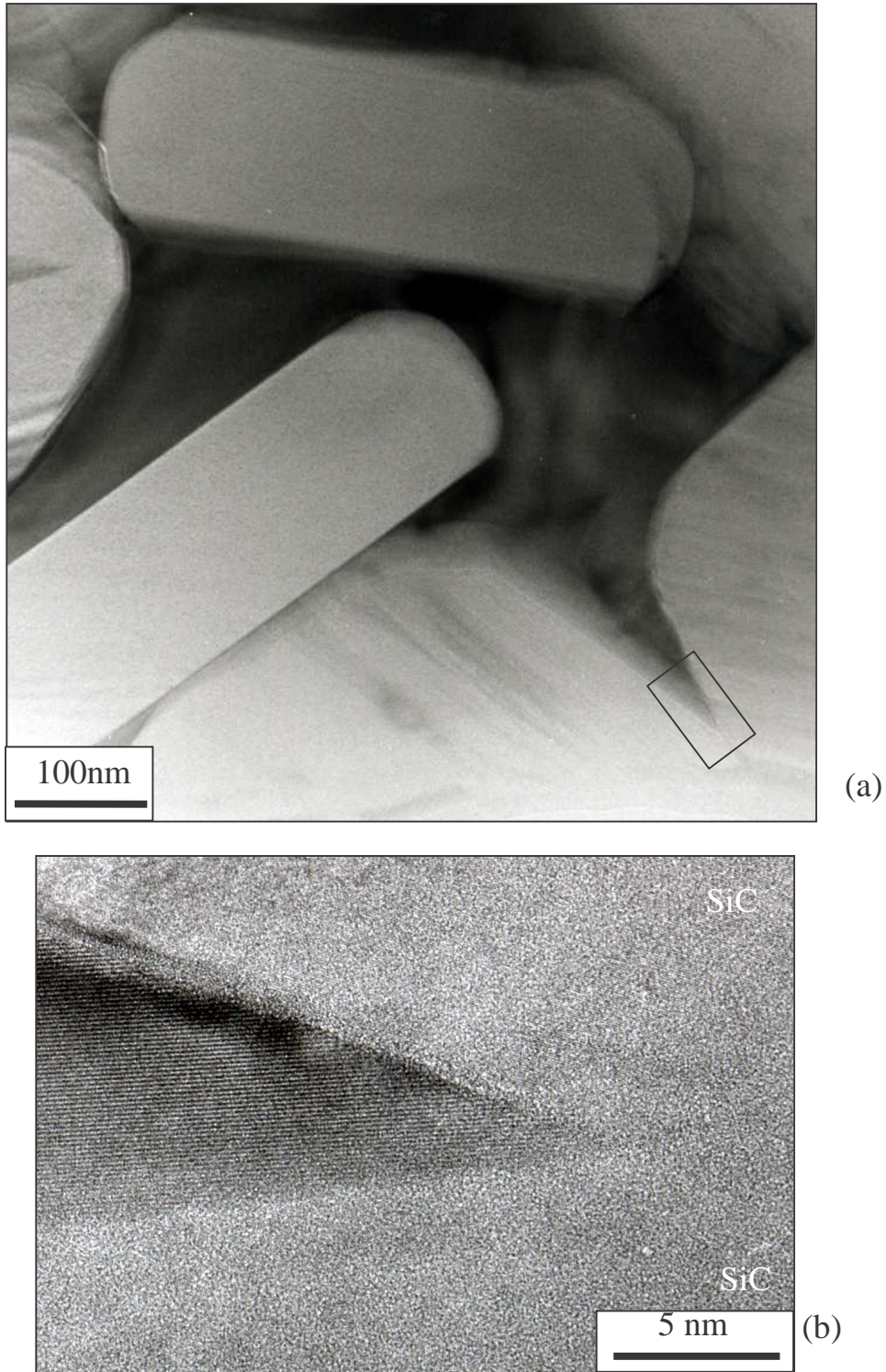


Fig. 6.19 (a) TEM image of a large intergranular pocket in 90β -60AlN-N₂. (b) HRTEM image of the region outlined by a square reveals that the large pocket is filled with a crystalline phase.

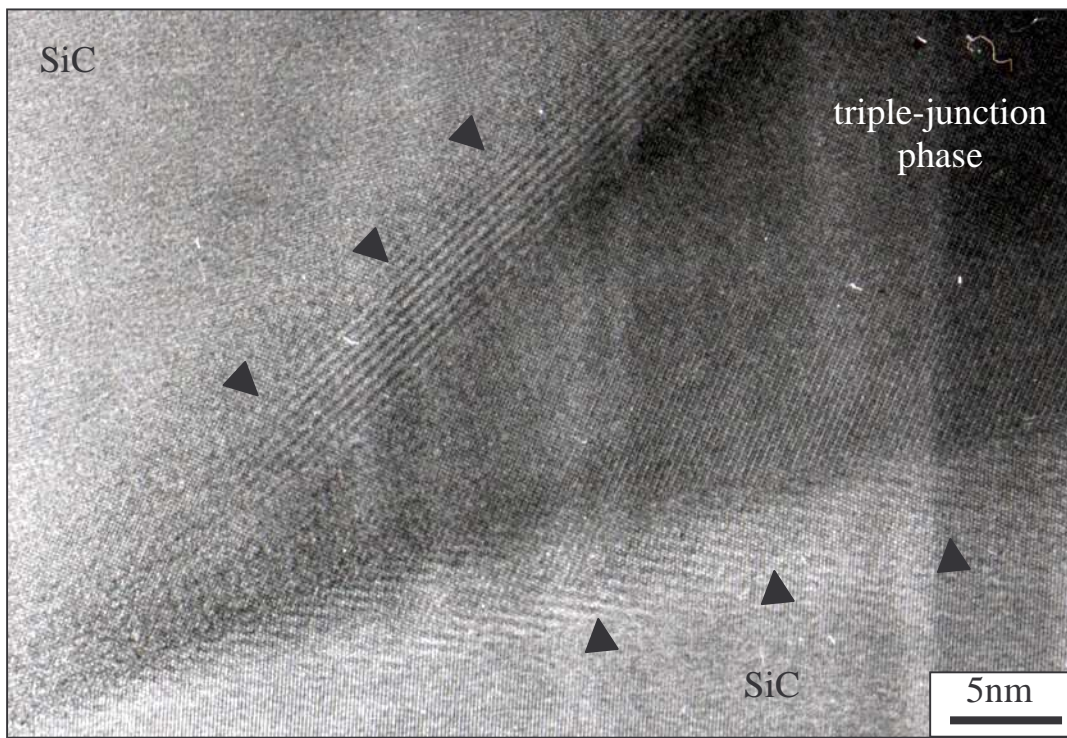


Fig. 6.20 HRTEM image of a crystallized triple-junction phase in 100α -60AlN-N₂. The moiré fringes, as indicated by arrows, are caused by the overlap of lattice fringes of the secondary crystalline phase and SiC grains.

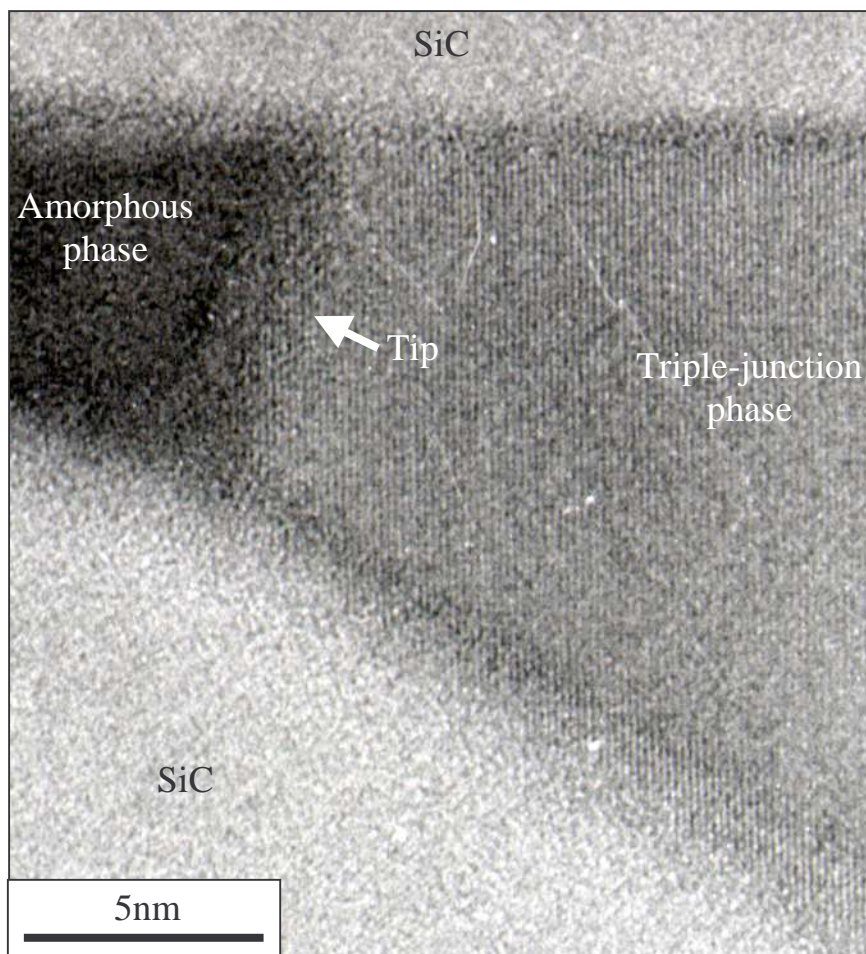


Fig. 6.21 HRTEM image after careful tilting to remove moiré fringes, revealing that amorphous phases are stable at the tip of the corner of the crystallized triple-junction phase in 100α -60AlN-N₂.

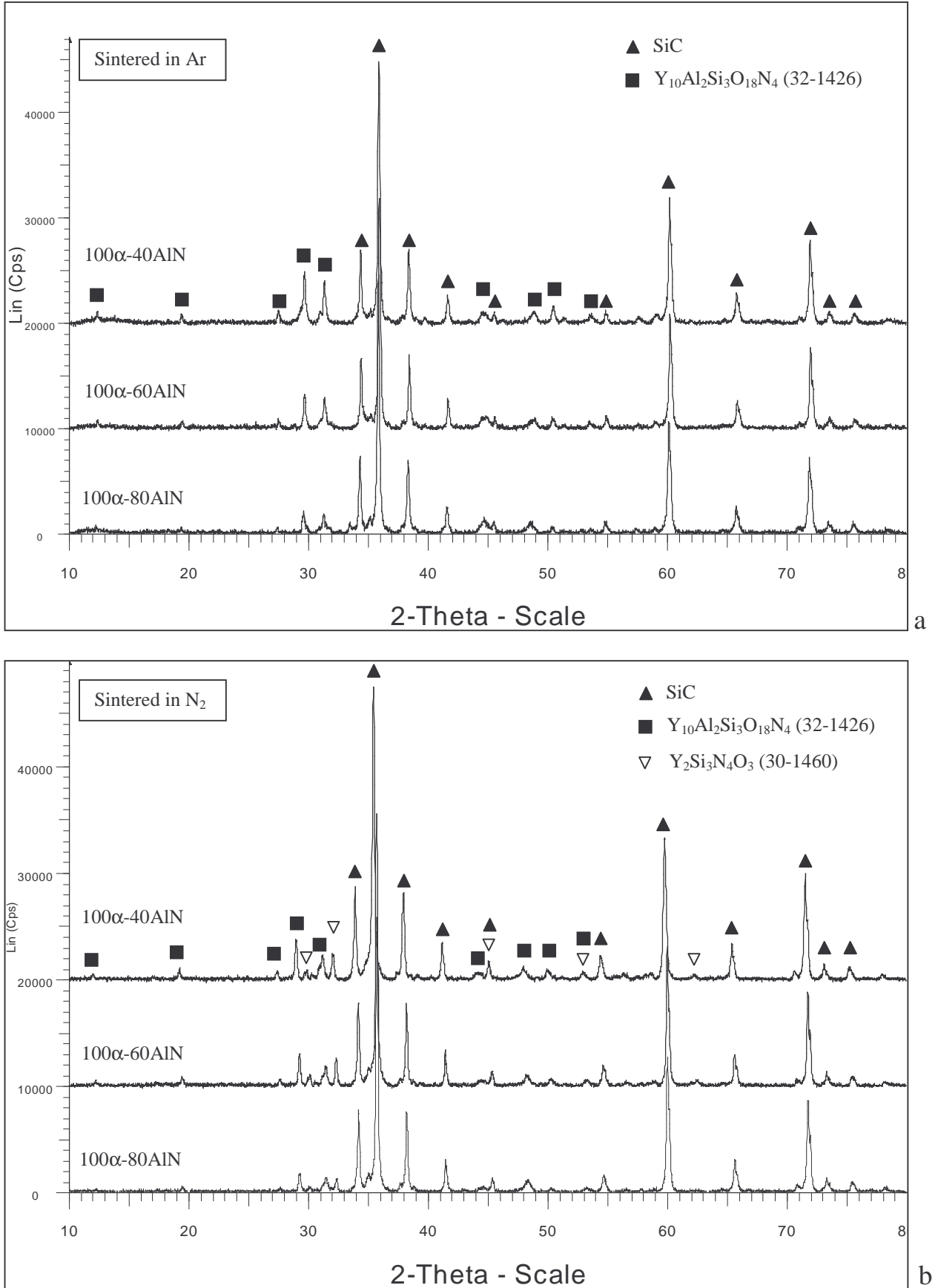


Fig. 6.22 XRD analyses of SiC samples using α -SiC as starting powder and sintered at 1950°C in Ar (a) and in N_2 (b). The nitrogen-rich $Y_2Si_3N_4O_3$ phase is identified in samples sintered in N_2 , but is absent in those sintered in Ar.

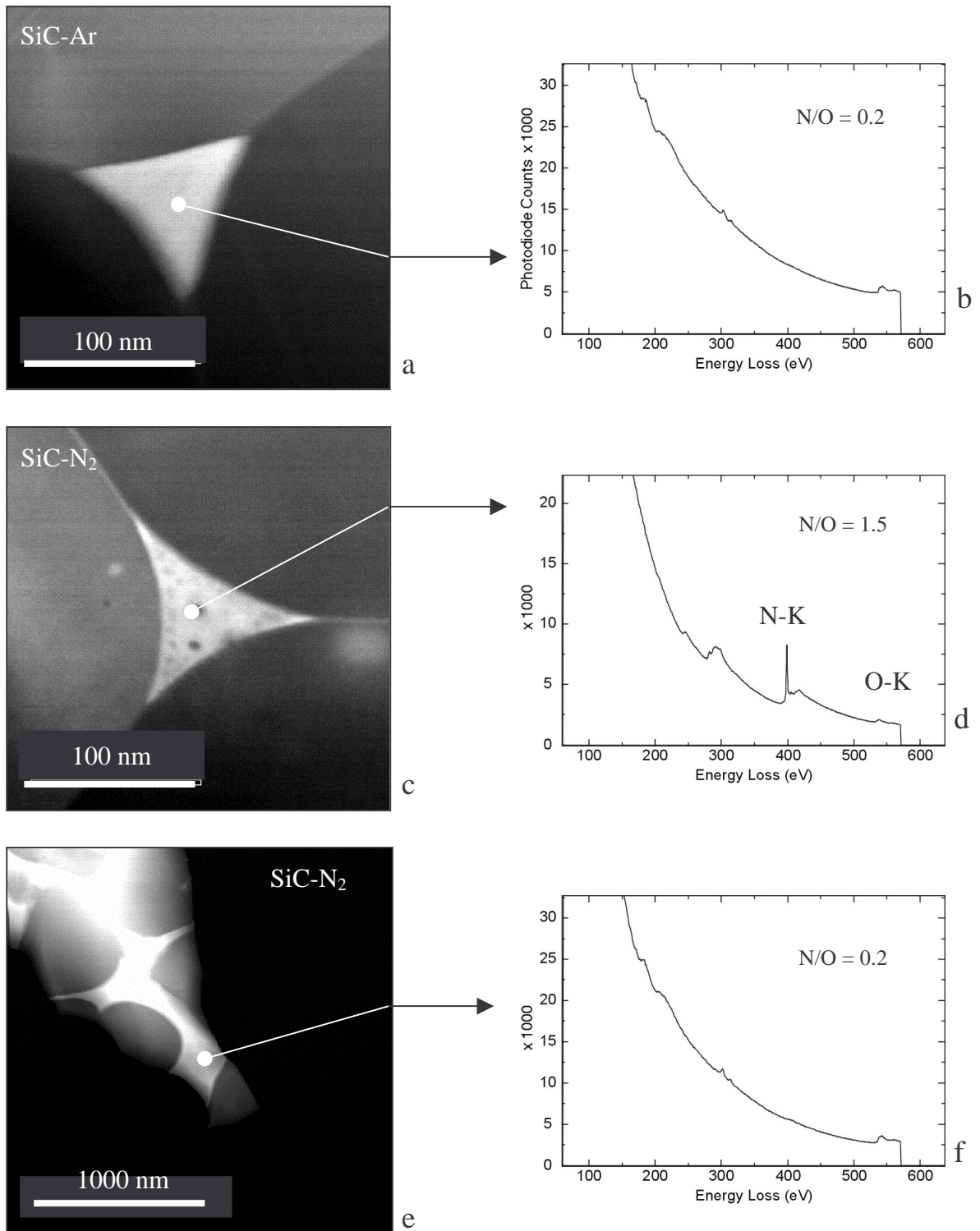


Fig. 6.23 EELS analyses on triple-junction phases in $100\alpha\text{-}60\text{AlN-Ar}$ (a, b), triple-junction phases in $100\alpha\text{-}60\text{AlN-N}_2$ (c, d) and large pockets in $100\alpha\text{-}60\text{AlN-N}_2$ (e, f). N/O atomic ratios are given with a relative deviation of 20%.

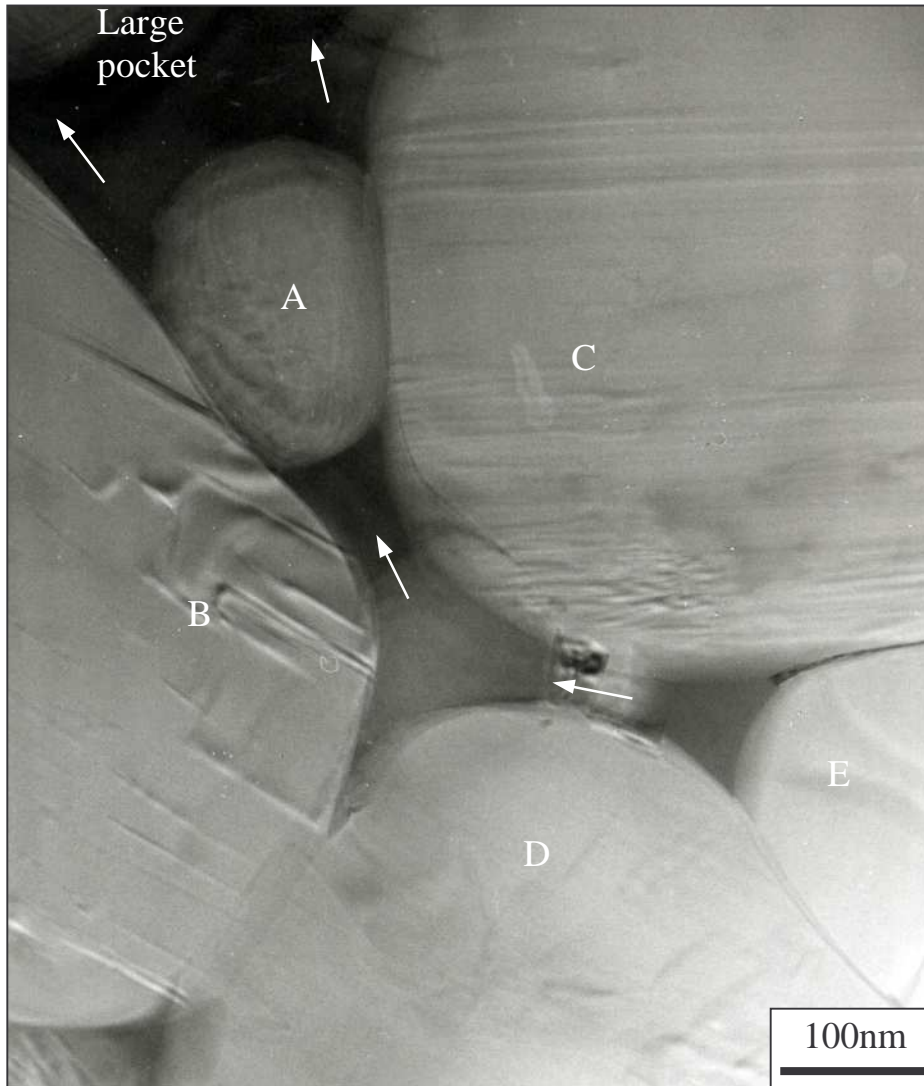
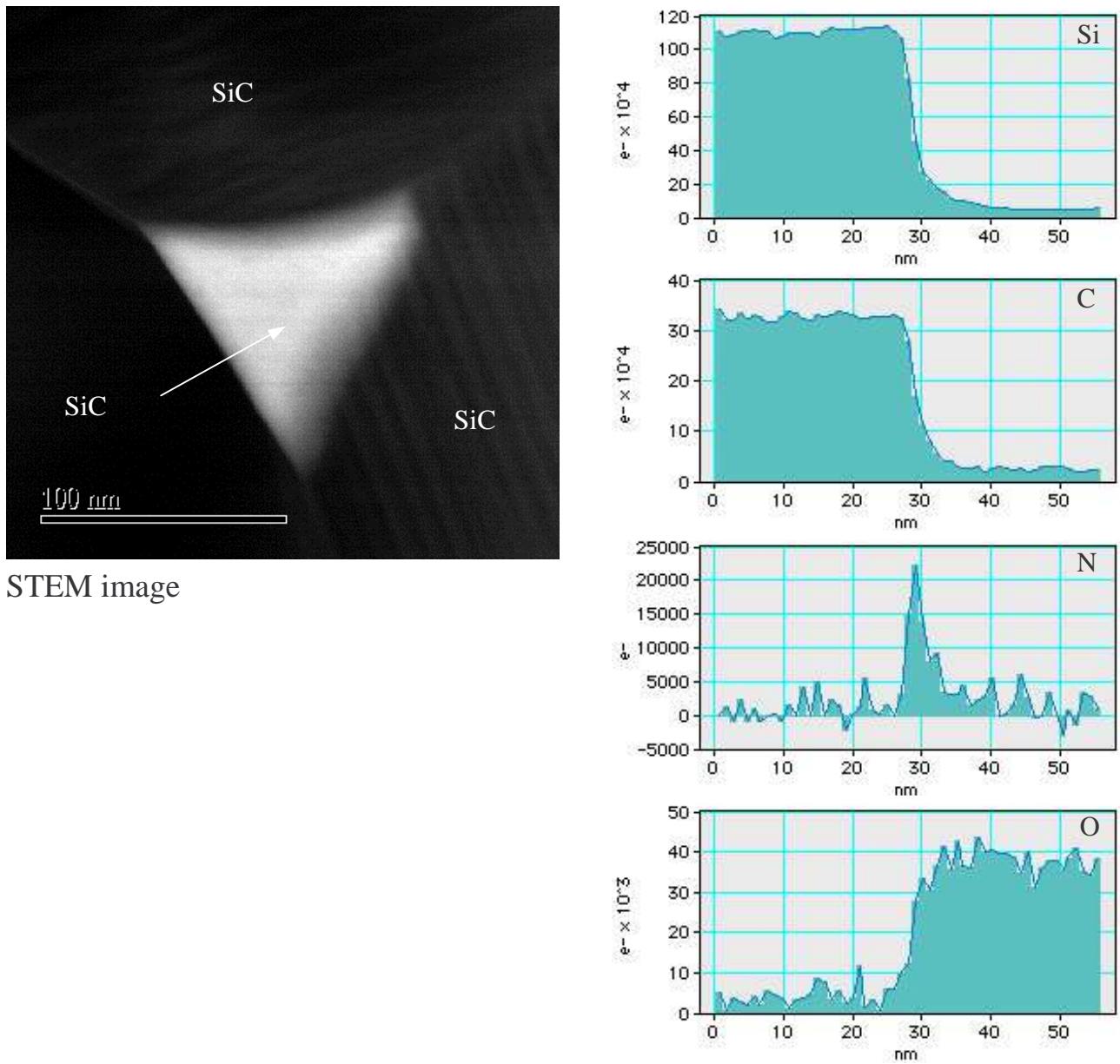
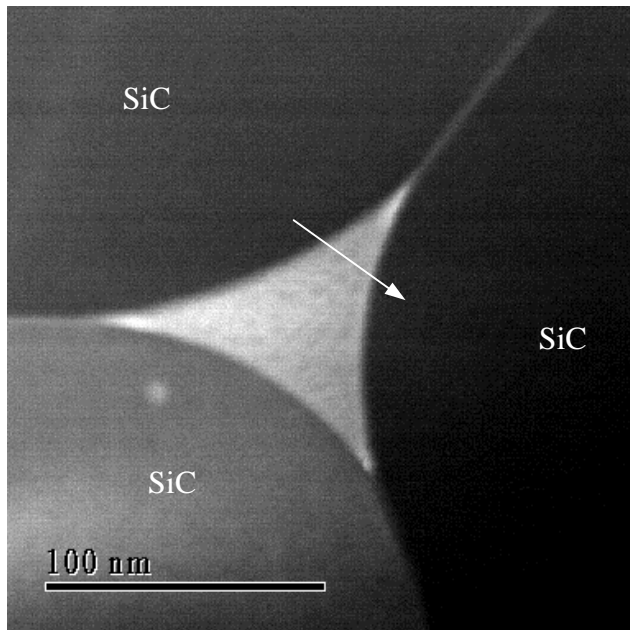


Fig. 6.24 TEM image of a microstructural feature which is common in the liquid phase sintered SiC ceramics. Due to the dissolution of the small SiC grain A and grain growth by reprecipitation of SiC grains B, C, D and E, the viscous liquid flows from the triple junction to the large pocket, as indicated by arrows, causing phase separation according to nitrogen content (see Section 6.7.4 for detailed discussion).



STEM image

Fig. 6.25 Line-scanning EELS analyses across a triple junction in $100\alpha\text{-}60\text{AlN-Ar}$ along the arrow indicated in the STEM image. Si, C, N and O distribution along the triple junction are drawn. N segregation at the interface is clearly visible.



STEM image

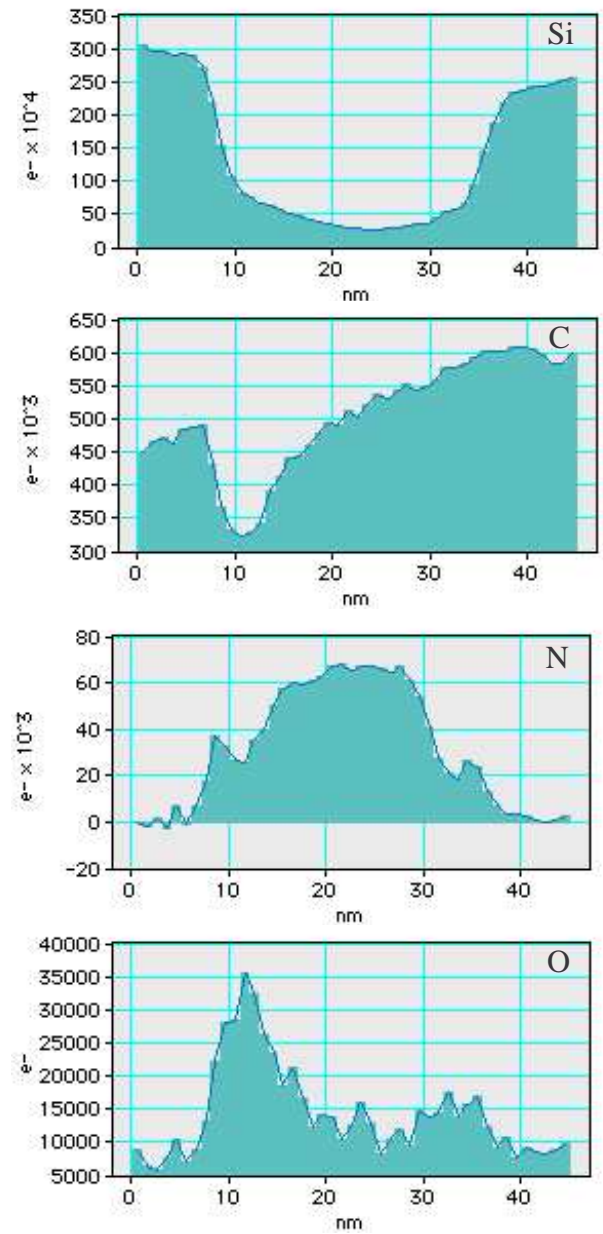


Fig. 6.26 Line-scanning EELS analyses across a triple junction in $100\alpha\text{-}60\text{AlN-N}_2$ along the arrow indicated in the STEM image. Si, C, N and O distributions across the triple junction are drawn. The C distribution is influenced by carbon contamination.

7 SUMMARY AND CONCLUSIONS

- Thin amorphous intergranular films were found to be stable at the grain boundaries of liquid-phase sintered SiC-SiO₂. The incorporation of C and N and the formation of oxycarbide and oxynitride glasses in the grain boundaries were detected by EELS analyses. Theoretical calculations based on Clarke's model [CLA87] show that the incorporation of C and N into the glass structure changes the structural correlation length of the intergranular phases, increasing the steric repulsive force and finally stabilizing the intergranular amorphous films. If this influence of C and N in the intergranular phase is taken into consideration in the calculation of the equilibrium film thickness, Clarke's model is found to describe the observed microstructures of LPS-SiC materials correctly.
- Incorporation of N from the sintering atmosphere causes grain growth of elongated nanometer-sized Si₂N₂O crystals in triple junctions of the SiC-SiO₂ model system. Incorporated N segregates preferentially at the surface of SiC grains, where the nucleation and grain growth of Si₂N₂O crystals most likely starts. At SiC/SiO₂ phase boundaries, crack deflection was observed.
- A N-rich amorphous phase was identified to be the main intergranular phase in coarse-grained SiC sintered with Y₂O₃-AlN additives in N₂ atmosphere, while three further secondary intergranular phases were AlN, Y₂SiN₄O₃, and Y₁₀Al₂Si₃O₁₈N₄, respectively. The high incorporation of N₂ from the sintering atmosphere into the intergranular phase leads to a direct increase of the N content in the intergranular phase and encourages the decomposition reaction between oxides and SiC grains. Together, these two effects can serve to explain the depletion in O and the formation of the N-rich amorphous phase in the intergranular spaces.
- Studies on a technologically relevant system consisting of fine-grained SiC sintered with Y₂O₃-AlN show that Y₂O₃-AlN is an efficient sintering additive for densification. Solution-reprecipitation is proved by TEM observation to be the main sintering mechanism. N₂ atmosphere, as compared with Ar atmosphere, is beneficial to suppress the decomposition of nitride additives, reduce the mass loss, retard the grain growth, and increase the homogeneity of the final grain-size distribution.
- The interlocking plate-like SiC grain morphology arising from the β-to-α SiC phase transformation was observed by TEM in SiC-Y₂O₃-AlN ceramics using β-SiC as main component of starting powders. Although the core/rim structure of SiC grains was not

visible in TEM images, doping of the 'rim' region by oxygen was detected by EELS, indicating the presence of such a characteristic microstructure.

- Stable amorphous films are present at all the grain boundaries in liquid-phase sintered SiC-Y₂O₃-AlN materials. The equilibrium thickness was measured by HRTEM to be 0.8 to 2 nm. EELS analyses show that Si, Al, C, O and N are present in the grain-boundary films. When N₂ instead of Ar is used as sintering atmosphere, N segregation at grain boundaries is largely increased, while the O content remains constant. Segregated carbon at grain-boundary films was proved by ELNES analyses to be bonded to silicon.
- Triple-junction phases in completely densified SiC-Y₂O₃-AlN materials were observed by HRTEM to be partly crystallized. In the case of Ar sintering atmosphere, the secondary crystalline phase is Y₁₀Al₂Si₃O₁₈N₄. In the case of N₂ sintering atmosphere, phase separation occurs during sintering and cooling: Y₁₀Al₂Si₃O₁₈N₄ occupies the main part of large grain pockets, while N-rich Y₂SiN₄O₃ crystals occupy the small triple junctions. The different viscosity of O-rich intergranular phase and N-rich intergranular phase at elevated temperature are believed to be the main cause of this phase separation. Line-scan EELS analyses show the detailed element distribution across the amorphous interface between the SiC grains and the triple junctions. It is again found that Ar and N₂ sintering atmosphere have different influences. The former leads to the enrichment of N in the interface, while the latter causes the formation of two interface layers: N-rich interface adjacent to the SiC grain and O-rich interface facing the triple junction.

Untersuchung des Gefüges und der Chemie von Korngrenzenfilmen und Tripelpunktphasen in flüssigphasengesinterten SiC-Keramiken

ZUSAMMENFASSUNG

Silizium Carbid ist ein viel versprechender Hochtemperatur – Strukturwerkstoff. Dichte SiC-Keramiken mit ausgezeichneten mechanischen Eigenschaften können durch Flüssigphasensintern mit Hilfe von Additiven hergestellt werden [WIE98, RIX00, BIS01]. Die Additive schmelzen bei hoher Temperatur, bilden eine flüssige Phase und verbessern das Verdichtungsverhalten. Die flüssige Phase füllt die Korngrenzen und Tripelpunkte aus und bildet nach der Abkühlung Korngrenzenfilme und Sekundärphasen. Gründliche Untersuchungen zur Mikrostruktur und Chemie dieser intergranularen Phasen sind sehr wichtig, um das Sinterverhalten des Materials zu verstehen und die mechanischen Eigenschaften zu verbessern. Im Vergleich zu Si_3N_4 , einer weiteren technisch wichtigen kovalenten Keramik, die ebenfalls über den Flüssigphasensinterprozeß hergestellt wird, sind bislang sehr wenige Untersuchungen zur intergranularen Phase in SiC-Keramiken angestellt worden. Ein Grund hierfür ist wahrscheinlich, dass die Existenz des Kohlenstoffs die Grenzflächenreaktionen und Kornwachstumsphänomene verkompliziert. In letzter Zeit hat die Elektronenmikroskopie, einschließlich der Rasterelektronenmikroskopie (REM), Transmissionselektronenmikroskopie (TEM), Hochauflösenden Elektronenmikroskopie (HRTEM) und Analytischen Elektronenmikroskopie (AEM), als die wichtigste Methode der Mikrostrukturforschung, einen großen Fortschritt erlebt. Das Auflösungsvermögen wurde erhöht, die Anwendbarkeit auf Probleme der Werkstoffwissenschaften wurde erweitert, die Instrumente wurden bedienerfreundlicher und, als bedeutsamster Faktor, die Computertechnik wird immer mehr dazu eingesetzt, die Effizienz und Zuverlässigkeit zu erhöhen. Deshalb können mit Hilfe dieser modernen Elektronenmikroskopiemethoden die Schwierigkeiten bei der Untersuchung der SiC-Keramik überwunden werden, wie in dieser Arbeit gezeigt wird.

Drei SiC-Keramiken wurden hergestellt und untersucht. Die erste ist ein Modellsystem, SiC-SiO₂. SiO₂ wurde als einziges Additiv verwendet, um eine intergranulare Phase ohne zusätzliche Elemente zu erhalten. Der Schwerpunkt der Modellsystemuntersuchung lag auf der Korngrenzenphase. Durch HRTEM wurde die Dicke der Korngrenzenphase gemessen, und durch Elektronenenergieverlustspektroskopie (EELS) wurde die Elementverteilung an der Korngrenze identifiziert. Die Ergebnisse werden mit Modellrechnungen verglichen, die von Clarke [CLA87] angestellt wurden, um die Wirkung von C und N auf die

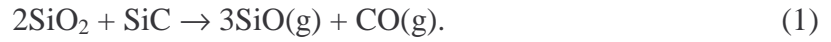
Korngrenzenstruktur zu verstehen. Das zweite Material ist ebenfalls ein Modellsystem, bei dem grobkörnige SiC Pulver zum Sintern mit Y_2O_3 und AlN als Sinteradditive verwendet werden. Eine grobkörnige Mikrostruktur bietet die Möglichkeit, genaue Punktanalysen mit Hilfe der Wellenlängedispersiven Röntgenanalyse (WDX, mit einer Fläche von minimal $1 \mu m^2$) durchführen zu können. Das dritte Material ist ein technisch wichtiges System, SiC- (Y_2O_3-AlN) [WIE98, RIX00, BIS01], mit ‚normaler‘ (sub- μm) Teilchengröße des Ausgangspulvers. Vollständige Verdichtung wurde in diesem System durch Flüssigphasensintern bei einer Sintertemperatur von $1950^\circ C$ erreicht. Aufwändige Untersuchungen des Gefüges und der Chemie von Korngrenzenfilmen und Tripelpunktphasen in diesem Material wurden durchgeführt.

Die Elektronenmikroskopie bildet sich in dieser Arbeit die wichtigste Forschungsmethode. Mit Hilfe des REM (Zeiss DSM982 Gemini) wurden Gefügemerkmale der keramischen Materialien untersucht. Die Bestimmung der Gefügeparameter erfolgte an digitalisierten Aufnahmen mit dem Programm IMAGE C der Fa. Imtronic. Um Elementzusammensetzung der intergranularen Phasen zu analysieren, wurden WDX und energiedispersive Röntgenanalyse (EDX) immer dann verwendet, wenn die Fläche der Phasen groß genug für das Punktauflösungsvermögen dieser spektroskopischen Methoden war. Der Schwerpunkt der elektronenmikroskopischen Untersuchungen in dieser Arbeit liegt bei der TEM und den damit zusammenhängenden Methoden. Damit können morphologische und strukturelle Probedetails mit Abmessungen weit unterhalb des μm -Bereichs untersucht werden. Ein JEOL JEM 4000EX und ein JEM 4000FX wurden als hauptsächliche Instrumente für Hellfeld- und Dunkelfeldabbildung (HF/DF) sowie für die Feinbereichsbeugung (SAD) verwendet. Mit den gleichen Instrumenten können HRTEM-Abbildungen von hinreichend dünnen Proben (ca. 10 nm) erzielt und somit direkte Informationen über den atomaren Abstand bzw. Kristallstrukturen in Festkörpern erhalten werden. Die beide Instrumente haben eine maximale Beschleunigungsspannung von 400 kV und eine Punktauflösung von 0.17 nm. EELS ist eine einzigartige Möglichkeit, qualitative und quantitative Informationen die chemische Zusammensetzung der intergranularen Phasen in nm-Bereich zu erhalten. Ein Raster-transmissionselektronenmikroskop (STEM, Model HB501, Vacuum Generators, U. K.) mit einem Gatan 666 PEELS Spektrometer wurde für die EELS Analysen in dieser Arbeit verwendet.

Das Modellsystem SiC-SiO₂

Nach zahlreichen Sinterversuchen an SiC-SiO₂ Keramiken stellte sich eine Sintertemperatur $1860^\circ C$ als optimal heraus. Niedrigere Sintertemperaturen führen zu einer geringeren Menge

an Flüssigphase und behindern das Sintern über den „Lösungs- und Wiederausscheidungs-Mechanismus“; höhere Sintertemperaturen als 1860°C begünstigen dagegen Gasphasenreaktionen von SiO₂ mit SiC, die zu einer Zersetzung des SiC führen, wie folgt:



Eine Gasmischung aus N₂ und CO wurde als Sinteratmosphäre verwendet und erwies sich als sehr effizient zur Unterdrückung der Gasphasenreaktionen. Die höchste erzielte Dichte war 94.2% der theoretische Dichte in einer SiC-Probe mit 20 Masse-% SiO₂, die bei 1860°C gesintert wurde. Diese Probe wurde für TEM Untersuchung ausgewählt.

Eine große Anzahl von Korngrenzen in SiC-SiO₂ wurde mittels HRTEM beobachtet. Ein dünner amorpher Film wird immer an Korngrenzen gefunden. Die Dicke des Korngrenzefilms beträgt zwischen 0.7 nm und 6 nm, mit einer Durchschnittsdicke von 1.5 nm. Die EEL-Spektren der amorphen Korngrenzefilme zeigt, dass sie nicht nur Si und O, sondern auch C und eine kleine Menge N enthalten. Die Existenz von C beruht auf einer begrenzten Löslichkeit von SiC in der Korngrenzephase, und N stammt aus der Sinteratmosphäre. Der Effekt der C und N auf die Korngrenzefilme wird verständlich, wenn Modellrechnungen im Rahmen des Clarke-Modells durchgeführt werden.

Nach Clarke erfolgt die Berechnung der totalen Wechselwirkungsenergie (Interaction Energy) über einen Korngrenzefilm hinweg durch [CLA87]:

$$E(h) = \frac{-H_{\alpha\beta\alpha}}{12\pi h^2} + \frac{2\alpha\eta_0^2\xi}{\tanh\left[\frac{h}{2\xi}\right]}. \quad (2)$$

Dabei ist $H_{\alpha\beta\alpha}$ die Hamaker-Konstante für den Fall, dass Körner des Materials α durch einen Film des Materials β getrennt werden; sie entscheidet über die Stärke der Anziehungskraft. h

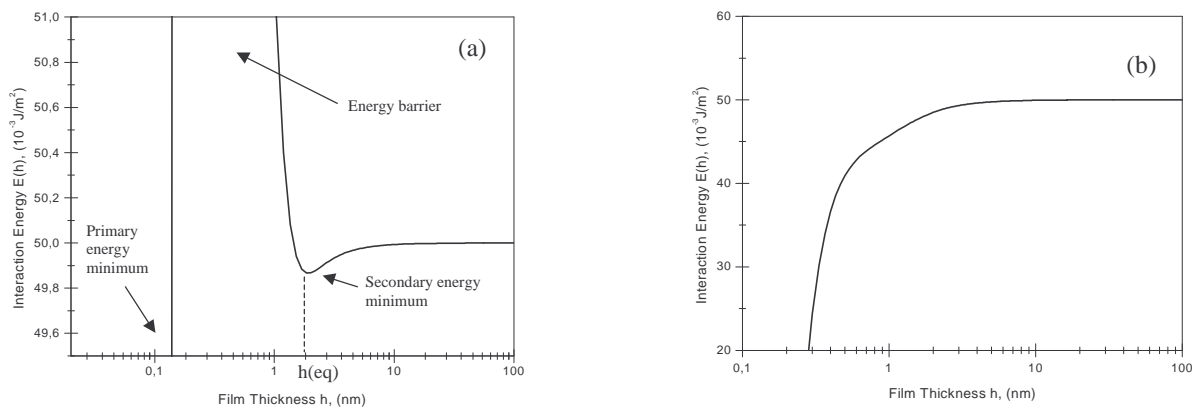


Abb. 1 Calculated interaction energy E as a function of the film thickness h for the configurations (a) Si₃N₄-SiO₂-Si₃N₄ and (b) SiC-SiO₂-SiC, assuming that $\alpha\eta_0^2 = 100$ MPa, $\xi = 2.5$ Å, (a) $H_{\alpha\beta\alpha} = 76 \times 10^{-21}$ J, and (b) $H_{\alpha\beta\alpha} = 233 \times 10^{-21}$ J. The resulting equilibrium thicknesses, $h(\text{eq})$, are (a) 1.8 nm and (b) 0 nm, respectively.

ist die Filmdicke; $\alpha\eta_0^2$ ist eine Konstante, die über die Stärke der Abstoßungskraft entscheidet; ξ ist die strukturelle Korrelationslänge, die eine molekulare Dimension annimmt. Für das System $\text{Si}_3\text{N}_4\text{-SiO}_2$, wobei die Hamaker-Konstante $H_{\alpha\beta\alpha} = 76 \times 10^{-21}$ J, $\alpha\eta_0^2 = 100$ MPa, und $\xi = 2.5$ Å (ungefähr die Größe der SiO_4 Tetraeder) ist, kann die Wechselwirkungsenergie als Funktion der Filmdicke h aufgetragen werden, wie in Abb. 1a gezeigt. Es ist offensichtlich, dass es zwei lokale Energieminima gibt, nämlich das „primäre Minimum“ bei verschwindender Filmdicke (d. h. die ‚saubere‘ Kristall-Kristall Korngrenze) und das „sekundäre Minimum“ bei der so genannten Gleichgewichts-Filmdicke (im Falle von $\text{Si}_3\text{N}_4\text{-SiO}_2$, 1.8 nm). Dieses Ergebnis der Berechnung entspricht den bisher durchgeführte HRTEM-Beobachtungen, wo regelmäßig ein amorpher Film mit Dicken im nm-Bereich zwischen den Si_3N_4 Körnern gefunden wurde. Die gleiche Situation existiert in vielen anderen Keramiksystemen. Das System SiC-SiO_2 bildet jedoch eine Ausnahme, weil die Hamaker-Konstante für dieses System außergewöhnlich groß ist, nämlich $H_{\alpha\beta\alpha} = 233 \times 10^{-21}$ J. Die Energie-Dicke Diagramm für dieser System wurde berechnet und ist in Abb. 1b gezeigt. Hier existiert keine Energiebarriere, und die Gleichgewichts-Filmdicke ist Null. Es besteht folglich eine Diskrepanz zwischen dieser Berechnung und den HRTEM-Beobachtungen, wo die amorphen Filme deutlich sichtbar sind. Um diesen Unterschied zu verstehen, sind EELS-Analysen der Korngrenzefilme sehr hilfreich. Wie EELS gezeigt hat, ist die Korngrenzephase im System SiC-SiO_2 nicht reines SiO_2 , sondern Siliciumoxycarbid und/oder Siliciumoxynitrid. Der Gehalt an C und N kann die Größe der Silicium-basierten Tetraeder im Vergleich zu SiO_4 -Tetraedern vergrößern (auf 3.1 Å für SiC_4 und 2.8 Å für SiN_4). Die Tatraeder können auch einen höheren Verknüpfungsgrad besitzen (4 Bindungen im Falle von C und 3 im Falle von N, an Stelle von nur 2 Bindungen im Falle von O). Diese beiden Effekte

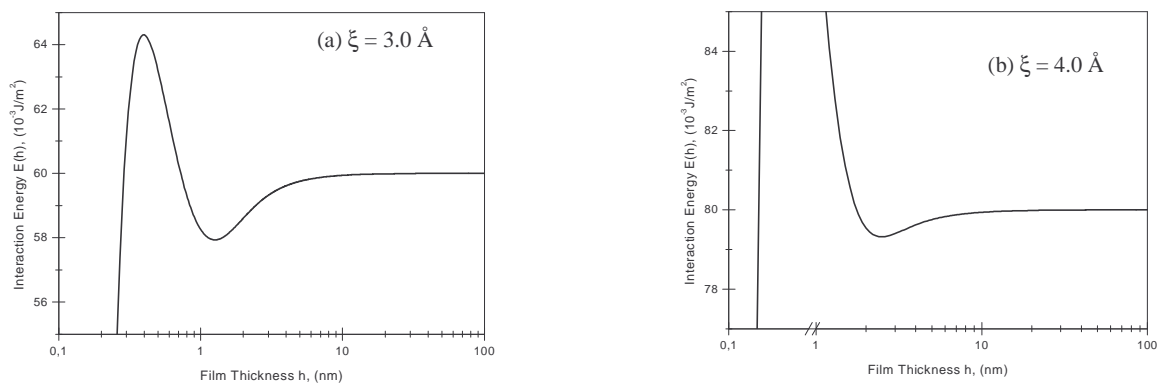


Abb. 2 Calculated Interaction Energy E as function of film thickness h for the $\text{SiC-SiO}_2\text{-SiC}$ system, assuming that $H_{\alpha\beta\alpha} = 233 \times 10^{-21}$ J, $\alpha\eta_0^2 = 100$ MPa, (a) $\xi = 3.0$ Å, and (b) $\xi = 4.0$ Å. The equilibrium thicknesses are (a) 1.3 nm and (b) 2.4 nm, respectively.

können dann die strukturelle Korrelationslänge ξ vergrößern. Abb. 2a und Abb. 2b zeigen die Rechnungsergebnis bei erhöhter struktureller Korrelationslänge ($\xi = 3.0 \text{ \AA}$ und $\xi = 4.0 \text{ \AA}$). Ein sekundäres Energieminimum entsteht, und die Gleichgewichts-Filmdicke beträgt 1.3 nm beziehungsweise 2.4 nm. Diese revidierten Berechnungen auf der Grundlage des Clarke-Modells entsprechen dann den experimentellen Ergebnissen. In Gegenwart von C und N ist der stabile Korngrenzefilm ein Charakteristikum von flüssigphasengesinterten SiC-Keramiken.

Außer der amorphen Phase befinden sich in der intergranulare Region der SiC-SiO₂ Keramik auch viele nm-große Kristalle (etwa 30 - 50 nm Länge). Quantitative EELS-Analysen zeigen, dass die Kristalle Si₂N₂O sind. Wieder erweist sich die Eintragung von N aus der Sinteratmosphäre als verantwortlich für die Bildung und das Wachstum dieser Kristalle. Detaillierte TEM und HRTEM Beobachtungen zeigen, dass das Kornwachstum der Kristalle immer nahe der Oberfläche der SiC-Partikel angefangen hat. Das bedeutet, dass sich eingetragener Stickstoff bei Sinter Temperatur vorzugsweise an Oberfläche der SiC-Partikel anreichert. Während des Abkühlens ist die N-reiche Oberfläche der SiC ist dann eingeeigneter Platz für die Heimbildung von Si₂N₂O, das die einzige ternäre kristalline Phase im Si-N-O system ist.

Das Modellsystem „Flüssigphasengesintertes SiC mit grobem Gefüge“

Aufgrund der Grobkörnigkeit (mittlere Korngröße von 64 μm) ist die Verdichtung dieser Materialien sehr erschwert. Trotzdem existieren viele Bereiche mit lokaler Verdichtung, in denen die Identifizierung der Zusammensetzung mit WDX durchführbar ist. Abb. 3 zeigt die WDX-Ergebnisse von Proben, die entweder in Ar oder in N₂ gesintert wurden; dargestellt ist jeweils die Zusammensetzung der intergranularen Phase. Eine sauerstoffreiche Oxynitridphase wurde als die intergranulare Phase von Ar-gesintertem SiC identifiziert (3a).

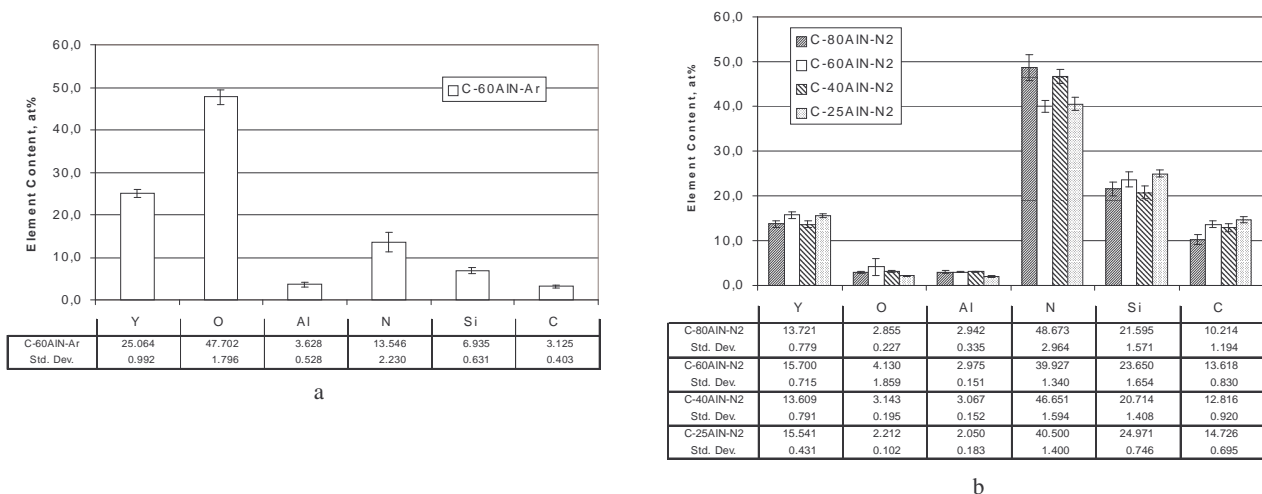


Abb. 3 WDX results on the amorphous intergranular phase of liquid phase sintered SiC, (a) sintered in Ar, (b) sintered in N₂. (Std. Dev. = standard deviation)

Im Unterschied dazu wurde in N₂-gesintertem SiC eine stickstoffreiche und an Sauerstoff verarmte intergranulare Phase gefunden (Abb. 3b). Es ist klar, dass die Oxynitridphase von zusammenschmelzen der Sinteradditive Y₂O₃ und AlN mit SiO₂, das auf der Oberfläche von SiC-Pulvern immer vorhanden ist, her stammt. In Ar-Atmosphäre kann die Oxynitridphase bis zum Ende der Sinterzeit erhalten. In N₂ muss dagegen der Stickstoffeintrag und daraus resultierende chemische Reaktionen betrachtet werden. Durch Zersetzungsreaktionen wie



entsteht elementares Silicium. Das flüssige Si kann chemische Bindungen mit N eingehen, was einen vermehrten Eintrag von N in die Schmelze begünstigt. Am Ende steht eine intergranulare Phase mit stark erhöhtem N-Gehalt, die auf Grund von Zersetzungsreaktionen wie (3) an Sauerstoff verarmt ist.

Die mit WDX gemessene intergranulare Phase erscheint in REM-Abbildungen hellgrau. Sie ist die Hauptphase in den intergranularen Bereichen und kann mittels SAD (TEM) als amorphe Phase identifiziert werden. Außerdem gibt noch eine Nebenphase in den intergranularen Bereichen, die in REM-Abbildungen weiß erscheint. Diese Nebenphase ist kristallin und kann mittels Röntgen-Pulverdiffraktometrie (XRD) identifiziert werden. XRD zeigt im Falle von Ar als Sinteratmosphäre Y₁₀Al₂Si₃O₁₈N₄ und Y₂O₃ sowie im Falle der N₂-Sinteratmosphäre Y₁₀Al₂Si₃O₁₈N₄, Y₂SiN₄O₃, und AlN als kristalline intergranulare Phasen an. Diese kristallinen Phasen werden auch durch WDX-Mapping nachgewiesen. Dies verdeutlicht nochmals den wichtige Effekt der Sinteratmosphäre.

Flüssigphasengesintertes SiC mit Y₂O₃-AlN Additiven

Alle Proben des technisch bedeutsamen Materialsystems SiC-Y₂O₃-AlN wurden zu hoher Dichte flüssigphasengesintert. Die relative Dichte ist am höchsten (99 %), wenn die Zusammensetzung des Sinteradditivs 60 mol% AlN und 40 mol% Y₂O₃ ist. Eine N₂-Sinteratmosphäre ist gegenüber Ar vorteilhaft zur Erreichung höherer Dichten bei geringerem Masseverlust, weil die Zersetzungsreaktion des Sinteradditivs AlN (AlN → Al + ½ N₂) durch N₂ effizient untergedrückt wird. TEM-Hellfeldabbildungen zeigen, dass die Auflösung kleiner SiC-Körner bei N₂-Sinteratmosphäre nicht so stark ausgeprägt ist wie bei Ar-Sinteratmosphäre. Das beruht darauf, dass im Falle von N₂ als Sinteratmosphäre der Eintrag von N die Viskosität der Flüssigphase erhöht, den Massetransport verringert und den Lösungs-Wiederausscheidungs-Sinterprozess verzögert. Wenn β-SiC pulver als Hauptkomponente zum Sintern benutzt wird, werden als Ergebnis der β-to-α Phaseumwandlung ausgedehnte, plättchenförmige Körner im TEM beobachtet. Die EELS-

Analysen zeigen, dass im Randbereich der SiC Körner Sauerstoff nachgewiesen werden kann, in den Kornmitten dagegen nicht. Diese Analyse bestätigt die Auflösung von O aus dem intergranularen Bereich in den SiC-Körnern.

HRTEM Abbildung an der SiC-Y₂O₃-AlN Gefüge zeigen die beständige Anwesenheit amorpher Filme an Korngrenzen. Die Dicke der Korngrenzenfilme liegt zwischen 0.8 nm und 2.0 nm. Poren und kristalline Zweitphasen werden an den Korngrenzen nicht beobachtet. Dagegen ist Graphit am manchen Korngrenzen Graphit nachweisbar, wenn auch in geringer Menge. Aus analogen Gründen, wie sie anhand des Systems SiC-SiO₂ diskutiert wurden, sind die Korngrenzenfilme durch die Gegenwart von C, N und anderen Elementen in der Korngrenzenphase stabilisiert. Die N- und O- Gehalte in der Korngrenzenphase wurden mit Hilfe von EELS- Methoden quantitativ bestimmt. Der Gehalt an N ist gering bei Ar als Sinteratmosphäre (7.7 Atom/nm²); er ist wesentlich höher bei N₂ als Sinteratmosphäre (52.5 Atom/nm²). Der Gehalt an O ist dagegen unabhängig von der Sinteratmosphäre (zwischen 46.5 und 49.3 Atom/nm²). Mit ELNES (Energy-Loss Near Edge Fine Structure Spectroscopy) wurde bestätigt, dass in der Korngrenzenphase hauptsächlich Si-O und Si-C Bindungen vorliegen.

In SiC-Y₂O₃-AlN Proben können mit dem TEM zwei verschiedene Arten von Tripelpunkten unterschieden werden. Es handelt sich dabei einmal um kleinere Zwickel, zwischen drei oder vier SiC Körnern, mit einer Größe um 50 nm. Zum anderen existieren größere Bereiche intergranularer Phase (> 500 nm im Durchmesser), die von einer größeren Anzahl von SiC-Körnern umgeben sind. SAD und HRTEM zeigen, dass die Tripelpunktphasen größtenteils kristallin sind. Zwischen den kristallinen Tripelpunktphasen und den SiC-Körnern gibt es immer amorphe Filme (Abb. 4). Durch XRD und EELS-Analysen kann die Zusammensetzung der Tripelpunktphasen identifiziert werden. Für in Ar gesinterte Proben findet sich nur eine kristalline Tripelpunktphase, nämlich Y₁₀Al₂Si₃O₁₈N₄. In N₂ gesinterte Proben

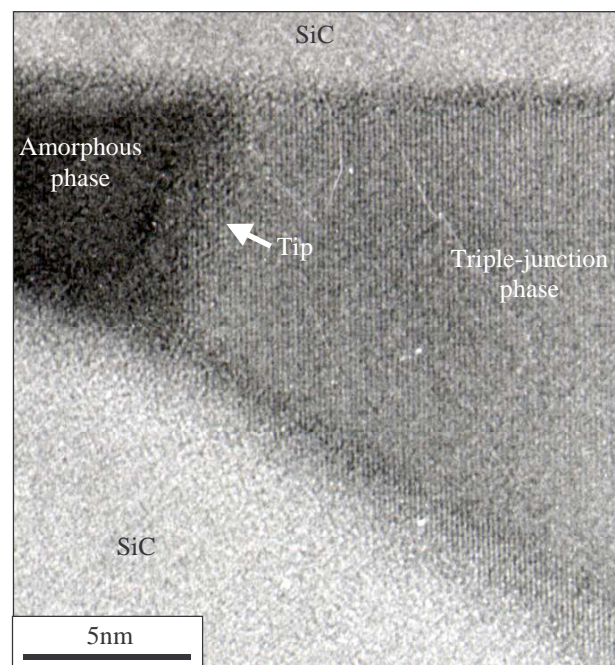


Abb. 4 HRTEM image after careful tilting to remove moire fringes, revealing that amorphous phases are stable at the tip of the corner of the crystallized triple-junction phase in sample 100 α -60AlN-N₂.

weisen dagegen zwei kristalline Phasen auf, und zwar $Y_{10}Al_2Si_3O_{18}N_4$ in größeren Tripelpunkten und $Y_2SiN_4O_3$ in kleineren Tripelpunkten (Abb. 5). Die charakteristische Verteilung der Tripelpunkphase in N_2 -gesinterten Probe beruht auf dem Einfluss der Sinteratmosphäre. Bei der Sintertemperatur wird die Flüssigphase lokal mit N angereichert. Dies führt zu einer erhöhten Viskosität; die Flüssigphase ist schwer zu bewegen und vorbleibt vorzugsweise im Bereich kleiner Tripelpunkt. Im Gegensatz dazu hat die Flüssigphase mit wenig N und einem hohen O-Gehalt eine höhere Beweglichkeit und kann deshalb eher in die

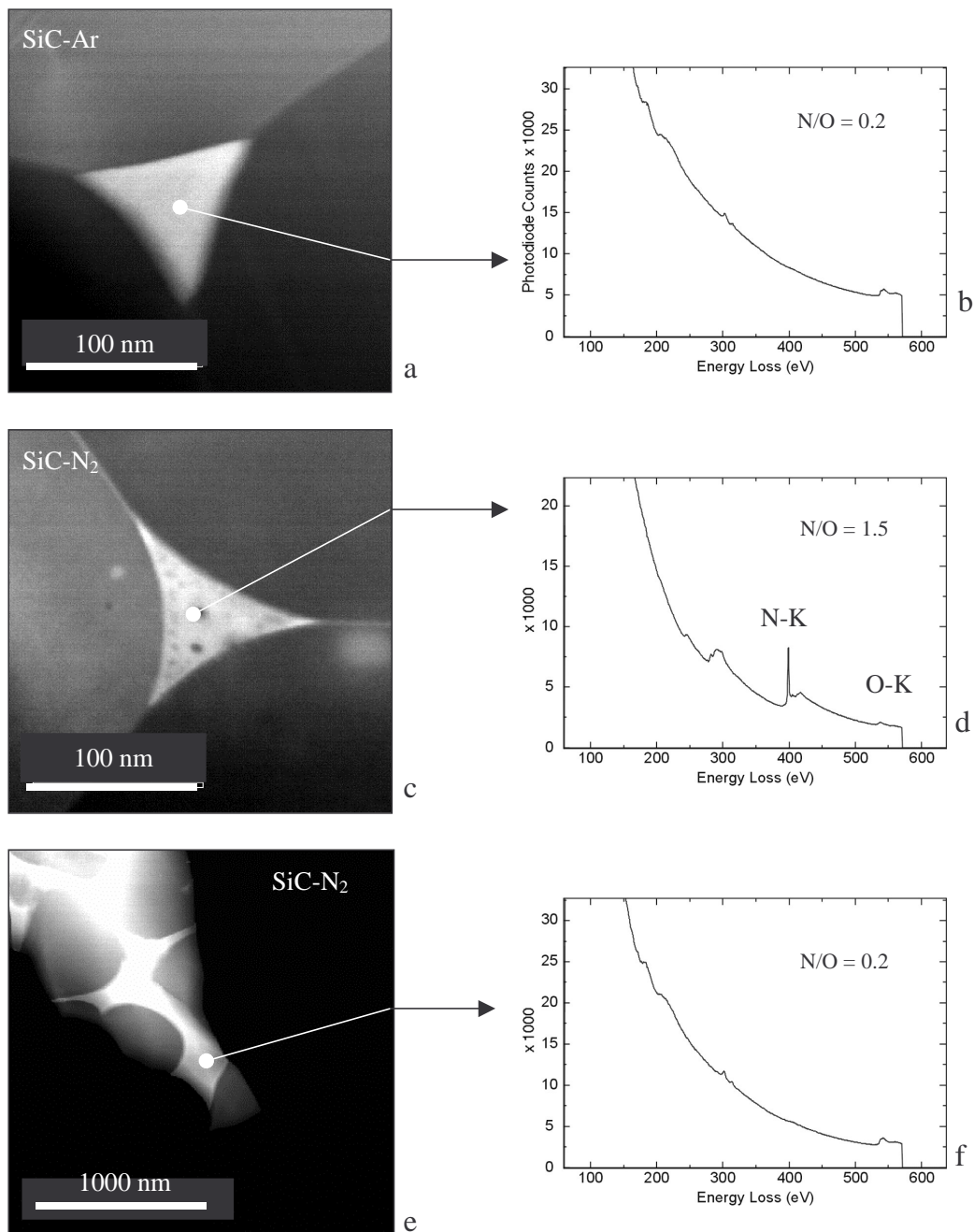
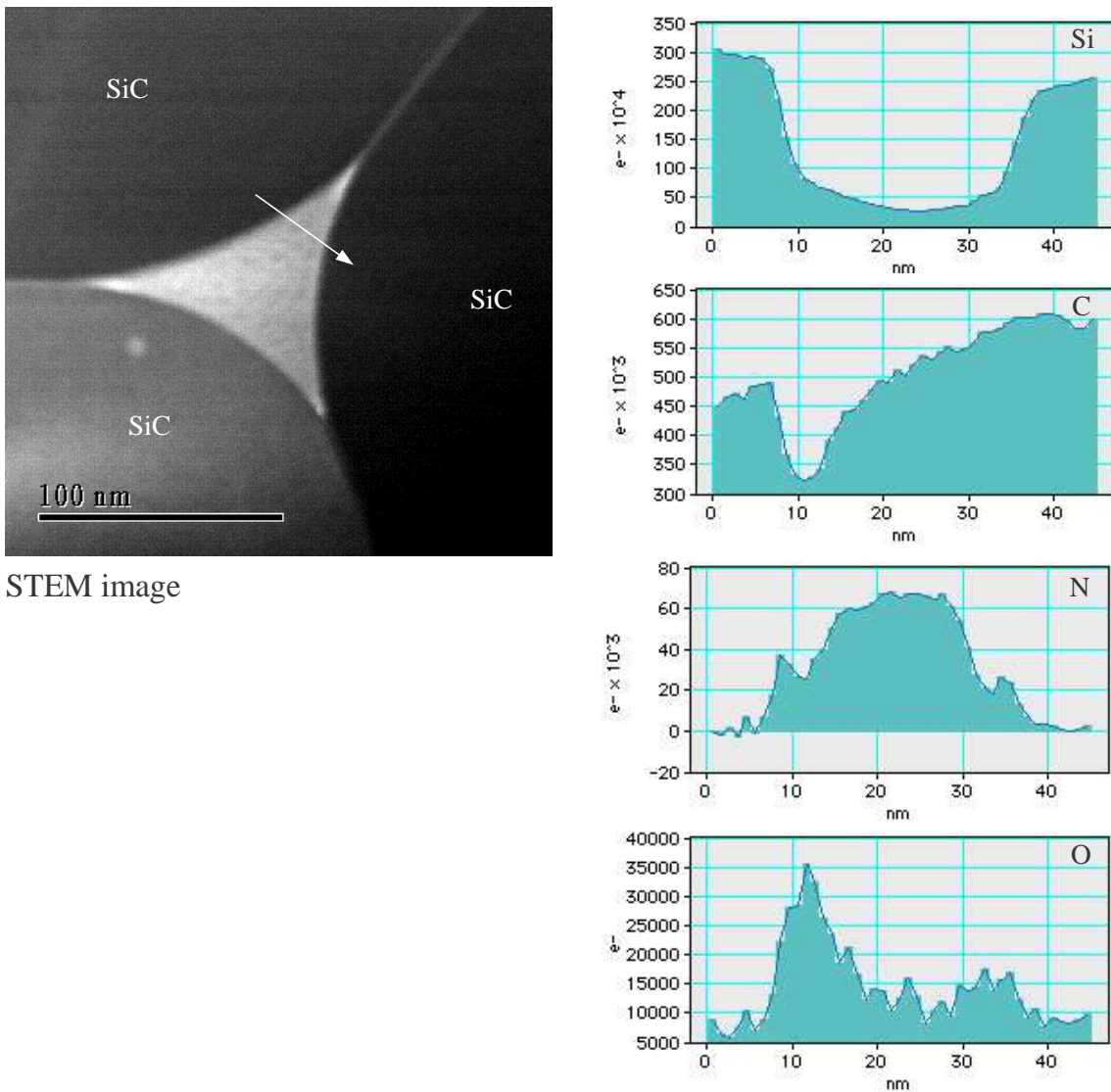


Abb. 5 EELS analyses on triple-junction phases in sample 100 α -60AlN-Ar (a, b), triple-grain junctions in sample 100 α -60AlN-N₂ (c, d) and large pockets in sample 100 α -60AlN-N₂ (e, f). N/O atomic ratios are given with a relative deviation of 20%.

großen Tripelpunkts abließen. Schließlich kristallisiert bei Abkühlung die N-reiche Phase in den kleinen Tripelpunkten zu $Y_2SiN_4O_3$, und die O-reiche Phase in den größeren Tripelpunkten zu $Y_{10}Al_2Si_3O_{18}N_4$.

Die amorphe Grenzflächenphase zwischen kristallinen Tripelpunktphasen und SiC-Körnern wurde mit Hilfe von EELS-Zeilenabtastungen (Line scans) untersucht. Die amorphe Phase ist reich an N, wenn Ar als Sinteratmosphäre benutzt wurde. Mögliche Ursachen hierfür sind: 1. die Oberfläche der SiC-Körner ist ein bevorzugte Platz für die Anreicherung von N; 2. als Ergebnis der Kristallisation der Tripelpunktphasen wird der Überschuss an N zur Grenzfläche getrieben. Das Ergebnis der EELS-Analyse mit N_2 als Sinteratmosphäre ist in Abb. 6 gezeigt. Hier ist die kristalline Tripelpunktphase ($Y_2SiN_4O_3$) reich an N. O ist im



STEM image

Abb. 6 Line-scanning EELS analyses across a triple junction in sample 100 α -60AlN- N_2 along the arrow indicated in the STEM image. Si, C, N and O distributions across the triple junction are drawn. The C distribution is influenced by carbon contamination.

Überschuss vorhanden und segregiert zur Grenzfläche. Deshalb weist die Grenzfläche zwei Schichten auf: eine ist N-reich und befindet sich unmittelbar auf der Oberfläche der SiC-Körner, die andere ist O-reich und befindet sich auf der Seite der Tripelpunktphase (Abb. 6).

REFERENCES

- ACH92 E. G. Acheson, U. K. Patent 17.911, 1892.
- ACK97 H. D. Ackler, "Thermodynamic Calculations and Model Experiments on Thin Intergranular Amorphous Films in Ceramics," Ph.D. Thesis, Massachusetts Institute of Technology, Cambridge, MA, (1997).
- ALL56 R. A. Alliegro, L. B. Coffin and J. R. Tinklepaugh, "Pressure-Sintered Silicon Carbide," *J. Am. Ceram. Soc.*, **39** [11] 386-389 (1956).
- BAR97 M. W. Barsoum, "Fundamentals of Ceramics," McGraw-Hill Co., Singapore, 1997, p.74.
- BEC98 P. F. Becher, E. Y. Sun, K. P. Plucknett, K. B. Alexander, C. H. Hsueh, H-T. Lin, S. B. Waters and C. G. Westmoreland, "Microstructural Design of Silicon Nitride with Improved Fracture Toughness: I, Effects of Grain Shape and Size," *J. Am. Ceram. Soc.*, **81** [11] 2821-2830 (1998).
- BIR86 D. P. Birnie, "A Model for Silicon Self-Diffusion in Silicon Carbide: Anti-Site Defect Motion," *J. Am. Ceram. Soc.*, **69** [1] C33-C35 (1986).
- BIS01 K. Biswas, G. Rixecker, I. Wiedmann, M. Schweizer, G. S. Upadhyaya and F. Aldinger, "Liquid Phase Sintering and Microstructure-Property Relationships of Silicon Carbide Ceramics with Oxynitride Additives," *Mater. Chem. Phys.*, **67** 180-191 (2001)
- BOB99 M. Bobeth, D. R. Clarke and W. Pompe, "A Diffuse Interface Description of Intergranular Films in Polycrystalline Ceramics," *J. Am. Ceram. Soc.*, **82** [6] 1537-1546 (1999).
- BON87 D. A. Bonnell, T. Y. Tien and M. Rühle, "Controlled Crystallization of the Amorphous Phase in Silicon Nitride Ceramics," *J. Am. Ceram. Soc.*, **70** 460-465 (1987).
- BRAD97 M. P. Brada and D. R. Clarke, "A Thermodynamic Approach to the Wetting and Dewetting of Grain Boundaries," *Acta mater.*, **45** [6] 2501-2508 (1997).
- BRAU94 W. Braue, H. J. Kleebe and C. Wehling, "Microstructure and Densification of Sintered (B+C)-Doped β -Silicon Carbide," *Mater. Res. Soc. Symp. Proc.*, **327** 269-274 (1994).
- CAN97 R. M. Cannon, "A Perspective on Segregants, Lassy Films and Wetting at Grain Boundaries in Ceramics," (The 1997 Sosman Lecture); Presented at the 99th Annual Meeting of the American Ceramic Society, Cincinnati, OH, May 7, 1997.
- CAO96 J. J. Cao, W. J. Moberlychan, L. C. De Jonghe, C. J. Gilbert and R. O. Ritchie, "In Situ Toughened Silicon Carbide with Al-B-C Additions," *J. Am. Ceram. Soc.*, **79** [2] 461-469 (1996).
- CAR91 R. W. Carpenter, W. Braue and R. A. Cutler, "Transmission Electron Microscopy of Liquid Phase Densified SiC," *J. Mater. Res.*, **6** [9] 1937-1949 (1991)
- CHI91 K. Y. Chia and S. K. Lau, "High Toughness Silicon Carbide," *Ceram. Eng. Sci. Proc.*, **12**[9-10] 1845-1861 (1991).
- CHI94 K. Y. Chia, W. D. G. Böcker and R. S. Storm, U. S. Pat. 5,298,470 (1994).
- CHIA94 Y-M. Chiang, L. A. Silverman, R. H. French and R. M. Cannon, "Thin Glass Film Between Ultrafine Conductor Particles in Thick-Film Resistors," *J. Am. Ceram. Soc.*, **77** [5] 1143-1152 (1994).
- CLA77 D. R. Clarke and G. Thomas, "Grain Boundary Phases in a Hot-Pressed MgO Fluxed Silicon Nitride," *J. Am. Ceram. Soc.*, **60** [11-12] 491-495 (1977).
- CLA82 D. R. Clarke, F. F. Lange and G. D. Schnittgrund, "Strengthening of a Sintered Silicon Nitride by Postfabrication Heat Treatment," *J. Am. Ceram. Soc.*, **65** C-51-C52 (1982).

- CLA87 D. R. Clarke, "On the Equilibrium Thickness of Intergranular Glass Phases in Ceramic Materials," *J. Am. Ceram. Soc.*, **70** [1] 15-22 (1987).
- CLA93 D. R. Clarke, T. M. Shaw, A. P. Philipse and R. G. Horn, "Possible Electrical Double-Layer Contribution to the Equilibrium Thickness of Intergranular Glass Films in Polycrystalline Ceramics," *J. Am. Ceram. Soc.*, **76** [5] 1201-1204 (1993).
- COP78 J. A. Coppola, et al., *Japanese Patent Application 53-121810*, 1978.
- COR90 L. Cordrey, D.E. Niesz and D. J. Shanefield, "Sintering of Silicon Carbide with Rare-Earth Oxide Additions," pp. 618-636 in *Sintering of Advanced Ceramics*, Vol. 7. Edited by C. A. Handwerker, J. E. Blendell and W. A. Kaysser. American Ceramic Society, Westerville, OH., 1990.
- CUT78 I. B. Cutler, P. D. Miller, W. Rafaniello, H. K. Park, D. P. Thompson and K. H. Hack, "New Materials in the Si-C-Al-O-N and Related Systems," *Nature*, **275** 434-435 (1978).
- CUT89 R. A. Cutler and T. B. Jackson, "Liquid Phase Sintered Silicon Carbide," pp. 309-318 in *Ceramic Materials and Components for Engines, Proceedings of the Third International Symposium*. Edited by V. J. Tennery. American Ceramic Society, Westerville, OH, 1989.
- DRO58 J. Drowart, G. De Maria and M. G. Ingram, "Thermodynamic Study of SiC Utilizing a Mass Spectrometer," *J. Chem. Phys.*, **41** [5] 1015 (1958).
- DUV93 M. -L. Duval-Riviere and J. Vicens, "Intergranular Film Analysis in α -SiC Sintered with Al-Additives," *J. de. Phys IV.*, 1417-1421 (1993).
- EDI76 J. W. Edington, "Practical Electron Microscopy in Materials Science", Van Nostrand Reinhold, New York, 1976.
- FAB83 K. T. Faber and A. G. Evans, "Crack Deflection Process – I. Theory," *Acta Metall.*, **31** 565-576 (1983).
- FAL97 L. K. L. Falk, "Microstructural Development during Liquid Phase Sintering of Silicon Carbide Ceramics," *J. Eur. Ceram. Soc.*, **17** 983-994 (1997).
- FAL98 L. K. L. Falk, "Electron Spectroscopic Imaging and Fine Probe EDX Analysis of Liquid Phase Sintered Ceramics," *J. Eur. Ceram. Soc.*, **18** 2263-2279 (1998).
- FIS90 G. R. Fisher and P. Barnes, *Phil. Mag. B.*, **61** 217-236 (1990).
- GER85 R. M. German, *Liquid Phase Sintering*. Plenum Press, New York, 1985.
- GOL02 J. A. Golczewski, H.J. Seifert and F. Aldinger, "A Thermodynamic Model of Amorphous Grain Boundary Interfaces in Liquid Phase Sintered SiAlON Ceramics," *Z. Metallkd.*, submitted.
- GRE76 C. Greskovich and J. H. Rosolowski, "Sintering of Covalent Solids," *J. Am. Ceram. Soc.*, **59** 336-343 (1976).
- GREU95 F. Greuter, "Electrically Active Interfaces in ZnO Varistor," *Solid State Ionics*, **75** [1] 67-78 (1995).
- GRÖ94 J. Gröbner, "Konstitutionsberechnungen im System Y-Al-Si-C-O," Dissertation, Universität Stuttgart, 1994.
- GU96 H. Gu, X. Pan, I. Tanaka, R. M. Cannon, M. J. Hoffmann, H. Müllejans and M. Rühle, "Structure and Chemistry of Intergranular Films in Ca-Doped Si₃N₄," *Materials Science Forum*, **207-209** 729-732 (1996).
- GU98 H. Gu, R. M. Cannon and M. Rühle, "Composition and Chemical Width of Ultrathin Amorphous Films at Grain Boundaries in Silicon Nitride," *J. Mater. Res.*, **13** [2] 376-387 (1998).
- HAN83 S. C. Hansen and D. S. Phillips, "Grain Boundary Microstructures in a Liquid-Phase Sintered Alumina," *Phil. Mag. A*, **47** [2] 209-234 (1983).
- HIR77 P. B. Hirsch, A. Howie, R. B. Nicholson, D. W. Pashley, and M. J. Whelan, "Electron Microscopy of Thin Crystals", 2nd edition, Krieger, Huntington, New

- York, 1977.
- HON79 J. D. Hong, "Self-Diffusion in Alpha and Beta Silicon Carbide", Proc. Of the 4th Int. Met. Mod. Ceram., Mat Sci. Monographs, 6, Energy and Ceramics, P. Vincenzini (Ed.) Elsevier (1979).
- HUA86 J. L. Huang, A. C. Hurford, S. L. Bruner, R. A. Cutler and A. V. Virkar, *J. Mater. Sci.*, **21** 1448-1456 (1986).
- IKE93 J. A. S. Ikeda, Y-M. Chiang, A. J. Garratt-Reed and J. B. Van der Sande, *J. Am. Ceram. Soc.*, **76** 2447 (1993).
- INO80 Y. Inomata, H. Tanaka, Z. Inoue and H. Kawabata, "Phase Relation in SiC-Al₄C₃-B₄C System at 1800°C," *J. Ceram. Soc. Jpn. (Yogyo Kyokaiishi)*, **88** [6] 353-355 (1980).
- INO82 Y. Inomata, "Free Energy Theory of the Initial Sintering of Solids," *J. Ceram. Soc. Jpn.*, **90** [9] 527-537 (1982).
- JAC88 T. B. Jackson, A.C. Hurford, S. L. Bruner and R. A. Cutler, "SiC-Based Ceramics with Improved Strength," pp.227-240 in *Silicon Carbide*. Edited by J. W. Cawley and C. E. Semler, Am. Ceram. Soc., Westerville, OH, 1988.
- JAC92 N. S. Jacobson, K. N. Lee and D. S. Fox, "Reactions of Silicon Carbide and Silicon (IV) Oxide at Elevated Temperatures," *J. Am. Ceram. Soc.*, **75** [6] 1603-1611 (1992).
- JÄR98 K. Järrendahl and R. S. Davis, "Materials Properties and Characterization of SiC," pp. 1-18 in *Semiconductors and Semimetals Vol. 52: SiC Materials and Devices*, edited by Y. S. Park, Academic Press, London, U. K., 1998.
- JCP95 Joint Committee on Powder Diffraction Standards, ASTM, Swartmore, 1995.
- JEU93 A. Jeutter, "Untersuchung der Phasenbeziehungen im System Aluminiumnitrid-Yttriumoxid," Diplomarbeit, Universität Stuttgart, 1993.
- JOU91 Z. C. Jou, A. V. Virkar and R. A. Cutler, "High Temperature Creep of SiC Densified Using a Transient Liquid Phase," *J. Mater. Res.*, **6** 1945-1949 (1991).
- JUN97 H-W. Jun, H-W. Lee, G-H. Kim and H. S. Song, "Effect of Sintering Atmosphere on the Microstructure Evolution and Mechanical Properties of Silicon Carbide Ceramics," *Ceram. Sci. Eng. Proc.* **18** [4] 487-504 (1997).
- KAN99 K. Kaneko, M. Yoshiya, I. Tanaka and S. Tsurekawa, "Chemical Blending of Oxygen in Intergranular Amorphous Layers in High-Purity β -SiC Ceramics," *Acta mater.*, **47** [4] 1281-1287 (1999)
- KAP95 H. Kaplan-Diedrich, A. Eckebrachtand, G. H. Frischat, "Viscosity and Surface Tension of Oxynitride Glass Melts," *J. Am. Ceram. Soc.*, **78** 1123 (1995).
- KEB97 P. Keblinski, S. R. Phillpot, D. Wolf and H. Gleiter, "On the Thermodynamic Stability of Amorphous Intergranular Films in Covalent Materials," *J. Am. Ceram. Soc.*, **80** [3] 717-732 (1997).
- KEP98 M. Keppeler, H.-G. Reichert, J. M. Broadley, G. Thurn, I. Wiedmann and F. Aldinger, "High Temperature Mechanical Behaviour of Liquid Phase Sintered Silicon Carbide," *J. Eur. Ceram. Soc.*, **5** 527-533 (1998).
- KES92 H. Kessler, H. -J. Kleebe, R. W. Cannon and W. Pompe, "Influence of Internal Stresses on Crystallization of Intergranular Phases in Ceramics," *Acta metall. mater.*, **40** [9] 2233-2245 (1992).
- KIM95 Y-W. Kim, M. Mitomo and H. Hirotsuru, "Grain Growth and Fracture Toughness of Fine-Grained Silicon Carbide Ceramics," *J. Am. Ceram. Soc.*, **78** [11] 3145-3148 (1995)
- KIM97 Y-W. Kim, W. Kim and D-H. Cho, "Effect of Additive Amount on Microstructure and Mechanical Properties of Self-Reinforced Silicon Carbide," *J. Mater. Sci. Letters*, **16** 1384-1386 (1997).
- KIM98 Y-W. Kim, M. Mitomo, H. Emoto and J-G. Lee, "Effect of Initial α -Phase

- Content on Microstructure and Mechanical Properties of Sintered Silicon Carbide," *J. Am. Ceram. Soc.*, **81** [12] 3136-3140 (1998).
- KIM99-1 Y-W. Kim, Y-I. Lee, M. Mitomo, H-J. Choi and J-G. Lee, "Fabrication and Mechanical Properties of Silicon Carbide-Silicon Nitride Composites with Oxynitride Glass," *J. Am. Ceram. Soc.*, **82** [4] 1058-1060 (1999).
- KIM99-2 Y-W. Kim and M. Mitomo, "Fine-Grained Silicon Carbide Ceramics with Oxynitride Glass," *J. Am. Ceram. Soc.*, **82** [10] 2731-2736 (1999).
- KIN59-1 W. D. Kingery, "Densification during Sintering in the Presence of a Liquid Phase. I. Theory," *J. Appl. Phys.*, **30** [3] 301-306 (1959).
- KIN59-2 W. D. Kingery, "Densification During Sintering in the Presence of a Liquid Phase. II. Experimental," *J. Appl. Phys.*, **30** [3] 307-310 (1959).
- KLE92 H. J. Kleebe, M. J. Hoffmann and M. Rühle, "Influence of Secondary Phase Chemistry on Grain-Boundary Film Thickness in Silicon Nitride," *Z. Metallkd.*, **83** [8] 610-617 (1992).
- KLE93 H. J. Kleebe, M. K. Cinibulk, R. M. Cannon and M. Rühle, "Statistical Analysis of the Intergranular Film Thickness in Silicon Nitride Ceramics," *J. Am. Ceram. Soc.*, **76** [8] 1969-1977 (1993).
- KLE97 H-J. Kleebe, "Structure and Chemistry of Interfaces in Si₃N₄ Ceramics Studied by Transmission Electron Microscopy," *J. Ceram. Soc. Jpn.*, **105** [6] 453-475 (1997).
- KNO32 M. Knoll and E. Ruska, *Z. Physik*, **78**, 318 (1932).
- KRS95 V. D. Krstic, *MRS Bull.*, **20** 46 (1995).
- LAN75 F. F. Lange, "Hot-pressing Behaviour of Silicon Carbide Powders with Additions of Aluminum Oxide," *J. Mater. Sci.*, **10** 314-320 (1975).
- LAN76 F. F. Lange und T. K. Gupta, "Sintering of SiC with Boron Compounds," *J. Am. Ceram. Soc.*, **59** [11-12], 537-538 (1976).
- LEE94 S. K. Lee and C. H. Kim, "Effects of α -SiC versus β -SiC Starting Powders on Microstructure and Fracture Toughness of SiC Sintered with Al₂O₃-Y₂O₃ Additives," *J. Am. Ceram. Soc.*, **77** 1655-1658 (1994).
- LEN97 R. Lenk and J. Adler, "SiC Platelet Orientation in a Liquid-Phase-Sintered Silicon Carbide Composite Formed by Thermoplastic Forming Techniques," *J. Eur. Ceram. Soc.*, **17** 197-202 (1997).
- LEW94 M. H. Lewis, "Crystallization of Grain Boundary Phases in Silicon Nitride and Sialon Ceramic," pp.217 in *Tailoring of Mechanical Properties of Si₃N₄ Ceramics*. Edited by M. J. Hoffmann and G. Petzow. Kluwer Academic Publishers, Dordrecht, The Netherlands, 1994.
- LOE94 R. E. Loehman, "Structure, Formation, and Stability of Oxynitride Glasses," pp. 167-175 in *Tailoring of Mechanical Properties of Si₃N₄ Ceramics*. Edited by M. J. Hoffmann and G. Petzow. Kluwer Academic Publishers, Dordrecht, The Netherlands, 1994.
- MAY98 J. Mayer, S. Matsumura and Y. Tomokiyo, "First Electron Spectroscopic Imaging Experiments on the New JEOL 2010 FEG," *J. Electron Microsc.*, **47** [4] 283-291 (1998).
- MCH94 A. E. McHale, "Phase Equilibria Diagrams, Volume X," *Am. Ceram. Soc.*, Westerville, OH, 1994.
- MOB96 W. J. Moberlychan, R. M. Cannon, L. H. Chan, J. J. Cao, C. J. Gilbert, R. O. Ritchie and L. C. De Jonghe, "Microstructural Development to Toughen SiC," *Mat. Res. Soc. Symp. Proc.*, **410** 257-262 (1996).
- MOB98 W. J. Moberlychan, L. C. De Jonghe, *Acta metall.*, **46** 2471 (1998).
- MUL94 M. A. Mulla and V. D. Krstic, "Mechanical Properties of β -SiC Pressureless Sintered with Al₂O₃ Additions," *Acta metall. mater.*, **42** [1] 303-308 (1994).

- NAD73 J. S. Nadeau, "Very High Pressure Hot Pressing of Silicon Carbide," *Am. Ceram. Soc. Bull.*, **52** [2] 170-174 (1973).
- NAD95 M. Nader, "Untersuchung der Kornwachstumsphänomene an flüssigphasengesinterten SiC-Keramiken und ihre Möglichkeiten zur Gefügeveränderung". Dissertation, Universität Stuttgart, 1995.
- NAG00 T. Nagano and K. Kaneko, "Superplasticity of Liquid-Phase-Sintered β -SiC with Al_2O_3 - Y_2O_3 -AlN Additions in an N_2 Atmosphere," *J. Am. Ceram. Soc.*, **83** [10] 2497-2502 (2000).
- OMO82 M. Omori and H. Takei, "Pressureless Sintering of SiC," *J. Am. Ceram. Soc.*, **65** [6] C-92 (1982).
- OMO85 M. Omori and H. Takei, "Composite Silicon Carbide Sintered Shape and Its Manufacturing," U. S. Pat., No. 4 502 983, 1985.
- OMO86 M. Omori and H. Takei, "Method for Preparing Sintered Shapes of Silicon Carbide," U. S. Pat., No. 4 564 490, 1986.
- PAD94-1 N. P. Padture, "In Situ-Toughened Silicon Carbide," *J. Am. Ceram. Soc.*, **77** [2] 519-523 (1994).
- PAD94-2 N. P. Padture and B. R. Lawn, "Toughness Properties of a Silicon Carbide with an *In Situ* Induced Heterogeneous Grain Structure," *J. Am. Ceram. Soc.*, **77** [10] 2518-2522 (1994).
- PAN98 C. G. Pantano, A. K. Singh and H. Zhang, "Silicon Oxycarbide Glasses," *J. Sol-Gel Sci. Tech.*, **14**, 7, (1998).
- PET76 G. Petzow and W. J. Huppmann, "Flüssigphasensintern-Verdichtung und Gefügeausbildung," *Z. Metallkde.*, **67** [9] 579-590 (1976).
- PEZ00 G. Pezzotti, H. Nishimura, K. Ota and H-J. Kleebe, "Grain-Boundary Viscosity of BaO-Doped SiC," *J. Am. Ceram. Soc.*, **83** [3] 563-570 (2000).
- PEZ97 G. Pezzotti, K. Ota and H-J. Kleebe, "Viscous Slip along Grain Boundaries in Chlorine-Doped Silicon Nitride," *J. Am. Ceram. Soc.*, **80** [9] 2341-2348 (1997).
- PEZ98 G. Pezzotti, H-J. Kleebe and K. Ota, "Grain-Boundary Viscosity of Polycrystalline Silicon Carbide," *J. Am. Ceram. Soc.*, **81** [12] 3293-3299 (1998).
- PIE86 L. A. Pierce, D. M. Mieskowski and W. A. Sanders, "Effect of Grain-Boundary Crystallization on the High-Temperature Strength of Silicon Nitride," *J. Mater. Sci.*, **21** 1345-1348 (1986).
- PRO75 S. Prochazka, "The Role of Boron and Carbon in the Sintering of Silicon Carbide," pp. 171-181 in *Special Ceramics 6*. Edited by P. Popper. British Ceramic Research Association, Stoke-on-Trent, U. K., 1975.
- PRO79 S. Prochazka, C. A. Johnson, and R. A. Giddings, "Atmosphere Effects in Sintering of Silicon Carbide," pp. 366-381 in Proc. of International Symposium of Factors in Densification and Sintering of Oxide and Non-Oxide Ceramics. Edited by S. Somiya and S. Saito. Tokyo Institute of Technology, Tokyo, Japan, 1979.
- PRO87 S. Prochazka, "Why is It Difficult to Sinter Covalent Substances?" General Electric R&D Center, Schenectady, USA, Technical Information Series, Class 1 GECI Program 89CRD025, (1987).
- RAJ81 R. Raj and F. F. Lange, "Crystallization of Small Quantities of Glass (or a Liquid) Segregated in Grain Boundaries," *Acta Metallurgica.*, **29** 1993-2000 (1981)
- RAJ93 R. Raj, "Fundamental Research in Structural Ceramics for Service Near 2000°C," *J. Am. Ceram. Soc.*, **76** [9] 2147-2174 (1993).
- RAM47 R. I. Ramsdell, *Amer. Mineral.*, **32**, 64 (1947).
- RAM90 R. Ramesh, S. M. Green and G. Thomas, "Microstructure Property Relations in the Bi(Pb)-Sr-Ca-Cu-O Ceramic Superconductors," pp. 363-403 in *Studies of*

- High-Temperature Superconductors*, Advances in Research and Applications, Vol. 5., Nova Science Publications, Commack, NY, 1990
- RIX00 G. Rixecker, K. Biswas, I. Wiedmann, and F. Aldinger, "Liquid-phase sintered SiC ceramics with oxynitride additives," *Journal of Ceramic Processing Research*, **1** 12 (2000).
- RIX01 G. Rixecker, I. Wiedmann, and F. Aldinger, *J. Europ. Ceram. Soc.*, in press (2001)
- RÜH84 M. Rühle, N. Claussen and A. Heuer, "Microstructural Studies of Y₂O₃-Containing Tetragonal ZrO₂ Polycrystals (Y-TZP)," *Advances in Ceramics Vol. 12, Science and Technology of Zirconia II.*, The American Ceramic Society, Columbus OH., 1984, pp. 352-370.
- RUH85 R. Ruh, A. Zangvil and J. Barlowe, "Elastic Properties of SiC, AlN and Their Solid Solutions and Particulate Composites," *Am. Ceram. Soc. Bull.*, **64** [10] 1368-1373 (1985).
- SAK88 T. Sakai and T. Aikawa, *J. Am. Ceram. Soc.*, **71** [1] C-7-C-9 (1988).
- SCH80 K. A. Schwetz und A. Lipp, "The Effect of Boron and Aluminium Sintering Additives on the Properties of Dense Sintered Alpha SiC," *Science of Ceramics* 10, Ed. H. Hausner, DKG, 1980, pp. 149-158.
- SEI00 H. J. Seifert, J. Peng, H. L. Lukas and F. Aldinger, "Phase Equilibria and Thermal Analysis of Si-C-N Ceramics," *J. of Alloys and Compounds*, in print, (2000).
- SEO92 W. S. Seo, C. H. Pai, K. Koumoto and H. Yanagida, "Behavior of Stacking Faults in SiC—Mechanism of Annihilation and Additive Effects," *Solid State Phenom.*, **25** 133-142 (1992).
- SHI85 S. Shinozaki, R. M. Williams, B. N. Juterbock, W. T. Donlon, J. Hangan and C. R. Peters, "Microstructural Developments in Pressureless-Sintered β -SiC Materials with Al, B, C Addition," *Am. Ceram. Soc. Bull.*, **64**[10] 1389-1393 (1985).
- SIG93 L. S. Sigl and H. J. Kleebe, "Core/Rim Structure of Liquid-Phase-Sintered Silicon Carbide," *J. Am. Ceram. Soc.*, **76** [3] 773-776 (1993).
- SMO79 R. H. Smoak, "Pressureless Sintering Beryllium Containing SiC Powder Compositions," U. S. Pat., No. 172 109, 1979.
- SUN91 W-Y. Sun, *J. Am. Ceram. Soc.*, **74** [2] 2753-2758 (1991)
- SUN98 E. Y. Sun, P. F. Becher, K. P. Plucknett, C-H. Hsueh, K. B. Alexander, S. B. Waters, K. Hirao and M. E. Brito, "Microstructural Design of Silicon Nitride with Improved Fracture Toughness: II, Effects of Ytria and Alumina Additions," *J. Am. Ceram. Soc.*, **81** [11] 2831-2840 (1998).
- SUZ86 K. Suzuki, "Relation between Microstructure and Fracture Toughness of Ceramics," *Ceramics Japan*, **21** [7] 590-597 (1986).
- SUZ91 K. Suzuki, "Pressureless-Sintered Silicon Carbide with Addition of Aluminum Oxide," in *Silicon Carbide Ceramics-2*, Ceramics Research and Development in Japan Series, Eds. S. Somiya und Y. Inomata, Elsevier Applied Science, London, 1991, pp. 163-182.
- TAN00 H. Tanaka, H. N. Yoshimura and S. Otani, "Influence of Silica and Aluminum Contents on Sintering of and Grain Growth in 6H-SiC Powders," *J. Am. Ceram. Soc.*, **83**[1] 226-228 (2000).
- TAN84 H. Tanaka, Y. Inomata, K. Tsukuda and A. Hagimura, "Normal Sintering of β -SiC Powder," *J. Ceram. Soc. Jpn.*, **92** [8] 461-465 (1984).
- TAN85 H. Tanaka, Y. Inomata, K. Hara and H. Hasegawa, "Normal Sintering of Al-Doped β -SiC," *J. Mater. Sci. Letters*, **4** 315-317 (1985).
- TAN91 H. Tanaka, "Sintering of Silicon Carbide," in *Silicon Carbide Ceramics-1*,

- Ceramics Research and Development in Japan Series, Eds. S. Somiya und Y. Inomata, London, Elsevier Applied Science, 213-236 (1991).
- TAN94 I. Tanaka, H. J. Kleebe, M. K. Cinibulk, J. Bruley, D. R. Clarke and M. Rühle, "Calcium Concentration Dependence of the Intergranular Film Thickness in Silicon Nitride," *J. Am. Ceram. Soc.*, **77** [4] 1911-1914 (1994).
- THO62 G. Thomas, "Transmission Electron Microscopy of Metals", Wiley, New York, 1962.
- THO79 G. Thomas and M. J. Goringe, "Transmission Electron Microscopy of Metals", Wiley, New York, 1979.
- TUR95 S. Turan and K. M. Knowles, "A Comparison of the Microstructure of Silicon Nitride-Silicon Carbide Composites Made with and without Deoxidized Starting Material," *J. Microscopy.*, **177** [3] 287-304 (1995).
- TUR96 S. Turan and K. M. Knowles, " $\alpha \rightarrow \beta$ Reverse Phase Transformation in Silicon Carbide in Silicon Nitride-Particulate-Reinforced-Silicon Carbide Composites," *J. Am. Ceram. Soc.*, **79** [11] 2892-2896 (1996).
- VAN96 F. K. Van Dijen and E. Mayer, "Liquid Phase Sintering of Silicon Carbide," *J. Eur. Ceram. Soc.*, **16** [4] 413-420 (1996).
- VET93 J. S. Vetrano, H-J. Kleebe, E. Hampp, M. J. Hoffmann and M. Rühle, "Yb₂O₃-Fluxed Sintered Silicon Nitride. Part 1. Microstructure Characterization," *J. Mater. Sci.*, **28** 3529-3538 (1993).
- WAN97 C. Wang, M. Mitomo and H. Emoto, "Microstructure of Liquid Phase Sintered Superplastic Silicon Carbide Ceramics," *J. Mater. Res.*, **12** [12] 3266-3270 (1997).
- WAN98 H. Wang and Y-M. Chiang, "Thermodynamic Stability of Intergranular Amorphous Films in Bismuth-Doped Zinc Oxide," *J. Am. Ceram. Soc.*, **81** [1] 89-96 (1998).
- WIE98 I. Wiedmann, "Herstellung und mechanische Eigenschaften von flüssigphasengesintertem Siliziumkarbid", Dissertation, Universität Stuttgart, 1998.
- WIE99 S. M. Wiederhorn, B. J. Hockey and J. D. French, "Mechanisms of Deformation of Silicon Nitride and Silicon Carbide at High Temperature," *J. Eur. Ceram. Soc.*, **19** 2273-2284 (1999).
- WIL85 R. M. Williams, B. N. Juterbock, S. S. Shinozaki, C. R. Peters and T. J. Whalen, "Effects of Sintering Temperature on the Physical and Crystallographic Properties of β -SiC," *Am. Ceram. Soc. Bull.*, **64** [10] 1385-1389 (1985).
- WIL96 D. B. Williams and C. B. Carter, "Transmission Electron Microscopy", Plenum Press, New York, 1996.
- YE99 H. Ye, V. V. Pujar and N. P. Padture, "Coarsening in Liquid-Phase-Sintered α -SiC," *Acta mater.*, **47** [2] 481-487 (1999).
- ZHA90 H. Zhang and G. Pantano, "Synthesis and Characterization of Silicon Oxycarbide Glasses," *J. Am. Ceram. Soc.*, **73** [4] 958-63 (1990).
- ZHO99 Y. Zhou, H. Tanaka, S. Otani and Y. Bando, "Low-Temperature Pressureless Sintering of α -SiC with Al₄C₃-B₄C-C Additions," *J. Am. Ceram. Soc.*, **82** [8] 1959-1964 (1999).

CURRICULUM VITAE (LEBENS LAUF)

Family name : YE
Given name: Haihui
Date of birth: January 10, 1972
Place of birth: Shanghai, China
Nationality: Chinese
Family status: married, one child

Education and working Experiences:

9. 1978 – 7. 1983 Baoji Primary School, Shanxi, China.
9. 1984 – 7. 1989 Ningbo Second Middle School, Zhejiang, China.
- July 1989 National Examination for University and College
9. 1989 – 7. 1993 Bachelor of Science degree in Inorganic Materials Science and Technology, East China University of Science and Technology, Shanghai, China.
- Bachelor thesis: PTC (positive temperature coefficient) thermistors**
8. 1993 – 8. 1995 Working in **Gillette (Shanghai) Limited Company** (A joint venture of The Gillette Company in Shanghai, China) as a quality assurance technician.
9. 1995 – 7. 1998 Master of Science degree in Inorganic Materials Science and Technology, East China University of Science and Technology, Shanghai, China.
- Master thesis: Centrifugal-SHS (self-propagating high-temperature synthesis) of $\text{MoSi}_2\text{-Al}_2\text{O}_3$ composite**
9. 1998 – Now Studying for Ph.D. of Science degree in Max-Planck-Institute for Metals Research and University of Stuttgart, Stuttgart, Germany, supported by Max-Planck-Society Scholarship.
- Ph.D. thesis: Microstructure and chemistry of grain-boundary films and triple-junction phases in liquid-phase sintered SiC ceramics**